Imperial College London
Department of Earth Science and Engineering

Capillary Trapping and Oil Recovery in Altered-Wettability Carbonate Rock

Nayef Alyafei

May 2015

Supervised by
Prof. Martin J. Blunt

Submitted in part fulfilment of the requirements for the degree of
Doctor of Philosophy in Earth Science and Engineering of Imperial College London
and the Diploma of Imperial College London

—To my Family

Declaration

I declare that this thesis, **Capillary Trapping and Oil Recovery in Altered-Wettability Carbonate Rock**, is entirely my own work under the supervision of Prof. Martin J Blunt. The work was performed in the Department of Earth Science and Engineering at Imperial College London. All published and unpublished material used in this thesis has been given full acknowledgment. This work has not been previously submitted, in whole or in part, to any other academic institution for a degree, diploma, or any other qualification.

Nayef Alyafei
Department of Earth Science and Engineering
Imperial College London
May 2015

Abstract

Understanding the displacement and trapping of a displaced phase in porous media is important for applications in improved oil recovery (IOR) and carbon capture and storage (CCS). In IOR, we design the process to leave as little residual oil behind as possible, while for CCS, we do the opposite: we wish to maximise the amount of CO_2 trapped by the host brine. Reservoir rocks display a range of wettability, from being preferentially water-wet–they spontaneously imbibe water–to oil-wet, or water repellent. Many rocks are mixed-wet, with both water-wet and oil-wet pores. The other wettability state is more intermediate-wet where, as we show, the rock appears to be largely non-wetting to both oil and water. Carbonate reservoirs, which house the majority of the world's remaining conventional oil, and which offer potential storage locations for carbon dioxide, have an altered wettability after contact with crude oil. In this thesis we study spontaneous displacement and trapping in carbonate rocks for different wettability conditions. The rate of spontaneous imbibition governs the rate with which oil, or carbon dioxide is trapped, while the residual saturation quantifies how much trapped. This is particularly important in carbonate reservoirs, which are almost extensively fractured. In these reservoirs, the principal mechanism for displacement is spontaneous imbibition of water to displace oil (or carbon dioxide) in the water-wet portions of the pore space.

Pore structure and wettability are two of the main factors affecting displacement and capillary trapping. Experimental and pore-scale modelling studies have found a monotonic increase of residual non-wetting phase saturation, S_{nwr}, with the initial non-wetting phase saturation, S_{nwi} in a water-wet medium. However, altered-wettability systems have received relatively little attention, particularly those which are intermediate-wet.

We first present the three carbonates we study in this thesis: Estaillades, Ketton and Portland. These are three quarry limestones that have very different pore structures and span a wide range of permeability. We present standard core analysis results including mercury injection capillary pressure and nuclear magnetic resonance response. We also study three-dimensional X-ray images of these samples, obtained at a resolution of a few microns. We use these experiments to assess the pore size distribution; we show that all the samples have micro-porosity and use the results to interpret the trapping and displacement experiments performed later.

We then perform spontaneous imbibition experiments in these three carbonates under strongly water-wet conditions. We use scaling equations and recently published analyt-

ical solutions to assess the recovery of these rocks. We perform two sets of experiments. In the first, we measure the mass of water imbibed as a function of time. We show that the amount imbibed scales as the square root of time. In the second series of experiments, we measure saturation profiles as a function of distance and time using X-ray CT scanning. We demonstrate that the saturation profiles are functions of distance divided by the square root of time. We also demonstrate that the profiles are consistent with the analytical theory and, using reasonable estimates of relative permeability and capillary pressure, we can match the experimental results with the analytical solutions. We discuss how, in combination with conventional measurements of relative permeability (steady-state or using Buckley-Leverett theory in an unsteady-state experiment) these measurements could be used to measure capillary pressure and relative permeability.

In the next phase of the study, we use organic acid (cyclohexanepentanoic acid) to alter the wettability of our samples and observe the relationship between the initial oil saturation and the residual saturation. We take cores containing oil and a specified initial water saturation and waterflood until 10 pore volumes have been injected. We record the remaining oil saturation as a function of the amount of water injected. In the water-wet case, with no wettability alteration, we observe, as expected, a monotonic increase between the initial and the remaining oil saturation. However, when the wettability is altered, we observe an increase, then a decrease, and finally an increase in the trapping curve for Estaillades limestone with a small, but continued, decrease in the remaining saturation as more water is injected. This behaviour is indicative of mixed-wet or intermediate-wet conditions as there is no spontaneous imbibition of oil and water. However, Ketton did not show indications of a significant wettability alteration with a similar observed trapping profile to that observed in the water-wet case. Portland limestone also showed a monotonic increasing trend in residual saturation with initial saturation but with a higher recovery, less trapping, than the water-wet case. Again, this is intermediate-wet behaviour with no spontaneous imbibition of either oil or water, and slow production of oil after water breakthrough. Finally, we repeat the same experiments but instead we age the three carbonates with a high asphaltenic content and high viscosity crude oil at 70°C mimicking reservoir conditions. The results show a monotonic increase in residual saturation as a function of initial saturation but with higher recovery than the water-wet cases for Estaillades and Portland, with again no indication of wettability alteration for Ketton. We discuss the results in terms of pore-scale recovery process and contact angle hysteresis. We observe recovery behaviour that lies between the water-wet and mixed-wet conditions previously studied in the literature.

Overall, the thesis demonstrates that recovery rate and the amount of trapping are sensitive to pore structure and wettability. Very different recovery trends were observed for three rocks with similar chemical composition. The work serves as a benchmark for further modelling and experimental studies. The recommendation is to reproduce, in the laboratory, conditions close to those observed in the reservoir, and to use imbibition

and displacement measurements to quantify and constrain multiphase flow properties.

List of Publications

Peer Reviewed Journal Articles

Alyafei, N., A. Qaseminejad Raeini, A. Paluszny, and M. J. Blunt, A sensitivity study of the effect of image resolution on predicted petrophysical properties, *Transport in Porous Media* (in review).

Schmid, K, **N. Alyafei**, S.Geiger, and M. J. Blunt, Analytical solutions for spontaneous imbibition: Fractional flow theory and experimental analysis, *SPEJ* (in review).

Alyafei, N., A. Al-Menhali, and M. J. Blunt, Experimental and analytical investigation of spontaneous imbibition in water-wet carbonates, *Transport in Porous Media* (in preparation).

Alyafei, N., and M. J. Blunt, The effect of wettability on capillary trapping, *Advances in Water Resources* (in preparation).

Conference Proceeding Papers

Alyafei, N., O.Gharbi, A. Qaseminejad Raeini, J. Yang, S. Iglauer, and M. J. Blunt (2013), Influence of micro-computed tomography image resolution on the predictions of petrophysical Properties, *International Petroleum Technology Conference*, doi:10.2523/16600-MS.

Anderson, R, **N. Al-Ansi**, and M. J. Blunt (2013), Experiments and analysis of imbibition in carbonates, *European Association of Geoscientist and Engineers*.

Al-Ansi, N., and M. J. Blunt, Measurements of remaining oil saturation in mixed-wet carbonates, *The International Symposium of the Society of Core Analysts*, 2013.

Alyafei, N., T. Sølling, and M. J. Blunt (2014), Experimental investigation of co-current and counter-current spontaneous imbibition using micro-computraized tomography, *The International Symposium of the Society of Core Analysts*, 2014.

Acknowledgments

First of all, I would like to thank Allah for all the blessings. I have been blessed with a loving family, the best supervisor, supporting friends, and a caring country.

To my Family

I would like to thank my parents for their continuous support and encouragement. Also, I would like to thank the rest of my family including uncles, aunts, cousins for the support, I hope I made you proud. Special thanks to my wife for her understanding and support. I would like to thank my grandparents, although my grandfather is not with us today, he was the one who encouraged me to pursue further education and never stop to learn. Finally, special gratitude goes to my lovely grandmother for her infinite love and prayers.

To my Supervisor

I would like to thank my supervisor Prof. Martin J. Blunt for his guidance throughout my PhD and the wonderful experience I had. I am honoured to be one of his research students. His support, guidance, and direction are integral of this thesis. Prof. Martin taught me how to become an independent researcher and able to establish my own research ideas and make them a reality. I am beyond grateful to him.

To my Friends and colleagues

In addition to my friends in Qatar, I was blessed to meet amazing people during my PhD journey. I would like to thank Dr. Iain Macdonald and Prof. Geoffrey Maitland for their continuous support. I also would like to thank Mr. Alex Toth for his lab training, my work would be impossible without his help. Also, I would like to thank Mr. Ali Al-Menhali and his lovely family for their support. I would like to thank my brother Mr. Zaki Al-Nahari, my neighbour Mr. Abdulaziz Al Balushi, my Costa coffee partner Mr. Abdulkareem Alroudhan, and Mr. Dawod Al-Mahrouqi for his kindness. In addition, I would like to thank the following people: Dr. Branko Bijeljic, Dr. Stefan Iglauer, Dr. Yukie Tanino, Dr. Rehab El-Maghraby, Dr. Ahmed Abushaikha, Mr. Ibrahim Daher, Mr. Obidi Onochie, Dr. Fahad Dilib, Dr. Ali Qaseminejad Raeini, Mr. Rachares Petvipusit, Mr. Norman Nicholls, Dr. Munira Al-Hadrami. Ms. Hannah Menke, Mr. Matthew Andrew, Dr. Saif Al Ghafri, Mr. Yacine Debbabi, Dr. Amer Syed, Dr. Karen

Schmid, Dr. Holger Ott, and Prof. Theis Sølling.

To my Country

I would like to thank my country, Qatar, for the support and encouragement to the Qatari youth to continue their education. I was blessed to work under the Qatar Carbonates and Carbon Storage Centre (QCCSRC) with a group full of high intellectual individuals. In addition, I would like to thank Qatar University for their support.

To my Examiners

I would like to thank my internal examiner Prof. Matthew Jackson and my external examiner Dr. Martin Fernø for agreeing to be my examiners and taking the time to read and evaluate my thesis.
Thank you,
Nayef Alyafei

Contents

List of Tables

List of Figures

1. Introduction

1.1. Carbon Capture and Storage

According to the United Nations (UN), climate change is one of the major challenges facing human kind in this century [*Stocker et al.*, 2013]. It threatens the ecological system of our planet with floods, drought, and temperature variations. Climate change is a consequence of human activities mainly from burning fossil fuels, which contributes about 85% of the world's primary energy [*International Energy Agency*, 2012]. The burning of fossil fuels and other industrial processes has led to, and will likely lead to further substantial increases in the concentration of the greenhouse gases (GHGs) (methane, nitrogen oxides, and carbon dioxide) in the atmosphere [*Wigley et al.*, 1996]. Among all GHGs, carbon dioxide (CO_2) has the most significant impact on climate change [*Alley et al.*, 2007]. The increase of CO_2 concentration is correlated to a rise in global mean temperature [*Friedlingstein et al.*, 2010]. If the global consumption of fossil fuels continues to grow at the same rate based on 2008 levels, the level of CO_2 is predicted to reach at least 550 ppm in 2100, Figure 1.1 [*Blunt*, 2010]. According to the National Research Council (NRC), the global mean temperature is estimated to rise by 6°C if the concentration exceeds 550 ppm.

The prime solution for climate change is to move away from dominantly carbon-based to other forms of energy, such as renewables and nuclear. However, the world is yet not prepared to switch to these alternative energy supplies mostly because of intermittency and affordability [*Tohidi et al.*, 2010]. Therefore, carbon capture and storage (CCS) can be implemented in a transition period during which fossil fuels are still widely used. CCS is a process where CO_2 is captured from its anthropogenic sources–mainly fossil fuel burning power stations–and sequestrated in sinks [*Gibbins and Chalmers*, 2008]. There are several geological sites where CO_2 can be stored, such as saline aquifers and oil reservoirs, Figure 1.2.

To maximise the storage efficiency in CCS, we need to understand the different CO_2 sequestration mechanisms, namely: structural trapping, solubility trapping, mineral trapping, and capillary trapping. In the sequestration process, CO_2 passes through all these mechanisms in stages with different time scales and storage contributions, Figure 1.3.

Structural trapping is when the reservoir fluid gets trapped beneath the cap-rock (which is an impermeable layer). This mechanism depends on the geological features of

the reservoir and occur relatively fast compared to the other mechanisms [*Bachu et al.*, 1994].

Solubility trapping occurs when the injected CO_2 mixes with the host brine; since the CO_2 is soluble in brine, the brine will dissolve CO_2 until it becomes fully saturated. This process can take from few years to thousands of years depending on the reservoir permeability; the higher the permeability of the reservoir, the faster the mixing will be [*Lindeberg and Wessel-Berg*, 1997].

Mineral trapping occurs after the acidic solution forms from mixing of the CO_2 and the host brine; this acidic mixture reacts with the formation rock over hundreds to many thousands of years [*Morse and Arvidson*, 2002, *Gunter et al.*, 1993].

Capillary trapping occurs when the CO_2 is trapped as bubbles in the pore space surrounded by the host brine. Capillary trapping can occur quickly. The amount of CO_2 trapped will depend on the rock geometry, fluid properties, and wettability [*Juanes et al.*, 2010, *Macminn et al.*, 2010].

Another potential application for CO_2 storage is enhanced oil recovery (EOR) where oil production can be improved by injecting CO_2 in reservoirs. The advantage of this process is that any cost associated with capturing CO_2 can be offset by oil production thus making CCS economically feasible. In addition, we take advantage of extracting the abundant oil resources while reducing CO_2 emissions to the atmosphere (this assumes CO_2 capture when burning the produced oil) and therefore protecting the environment.

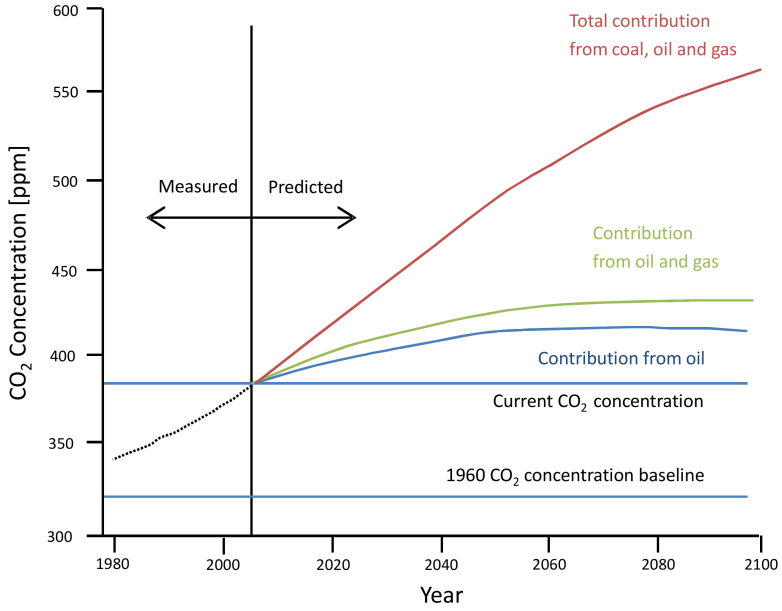

Figure 1.1. Predicted and measured atmospheric CO_2 concentrations based on the concentration measured in Hawaii from 1980 and 2008 (dashed line). While the the solid lines represent predictions of the contribution of coal, oil, and gas to the CO_2 concentration in the future. This figure is reproduced from *Blunt* 2010.

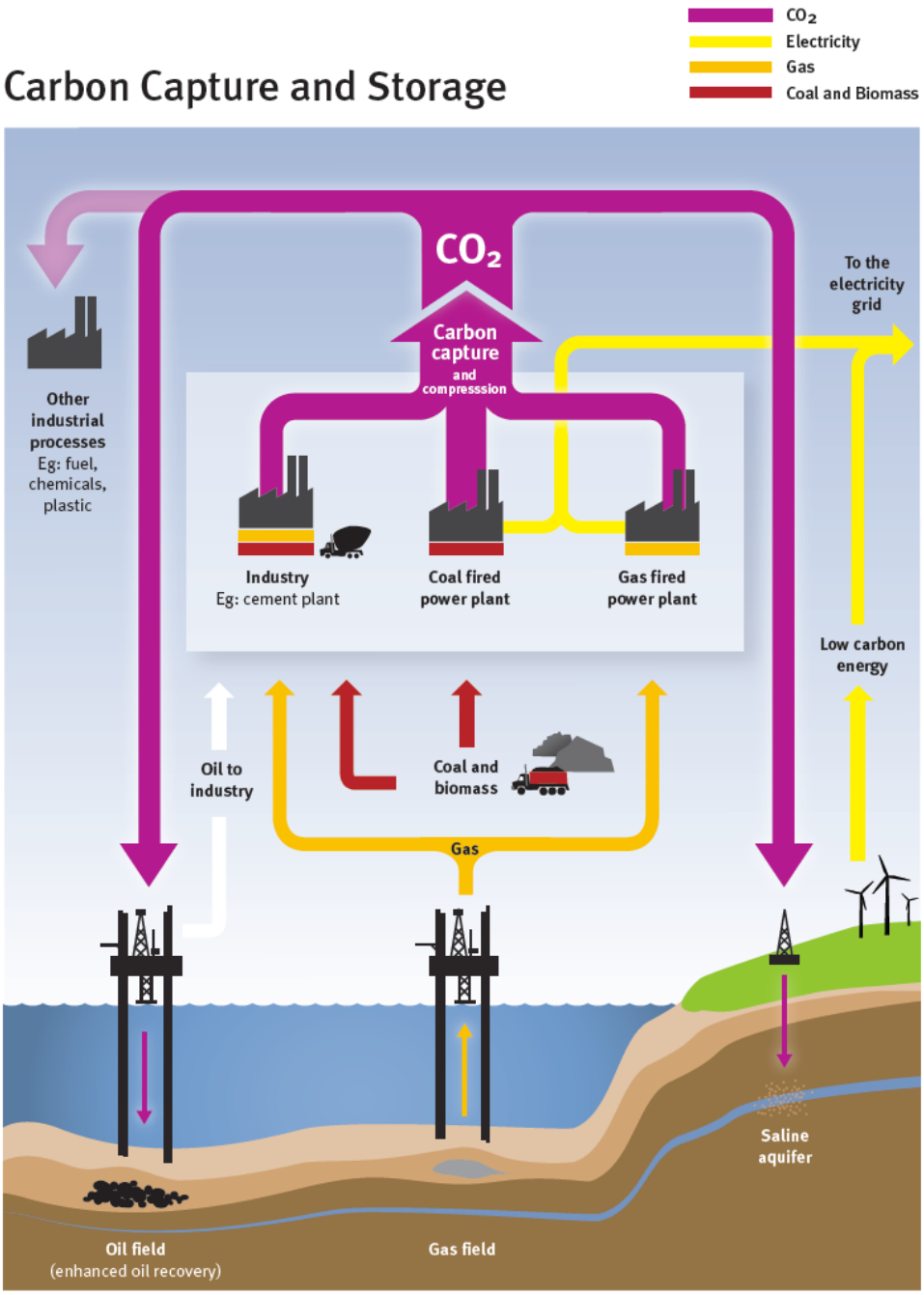

Figure 1.2. Schematic of CCS, the figure shows the process from collecting the CO_2 from power plants to injecting it in saline aquifers for storage purposes or injecting it in oil fields for EOR purposes [*Blunt*, 2010].

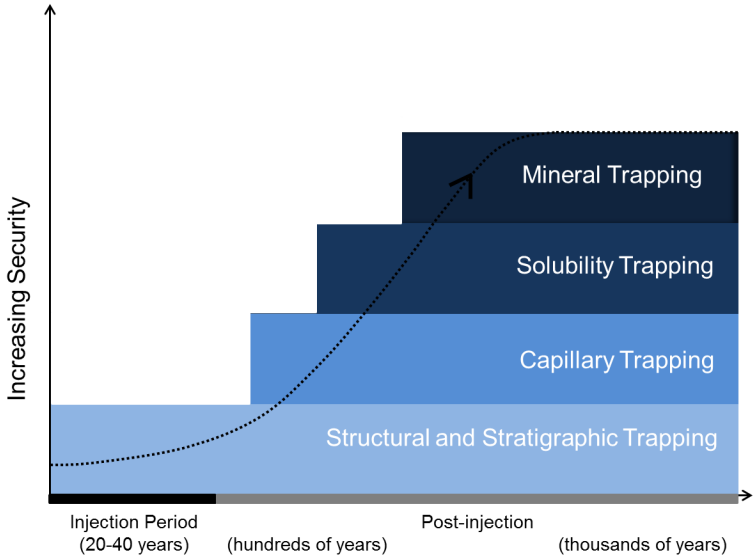

(a)

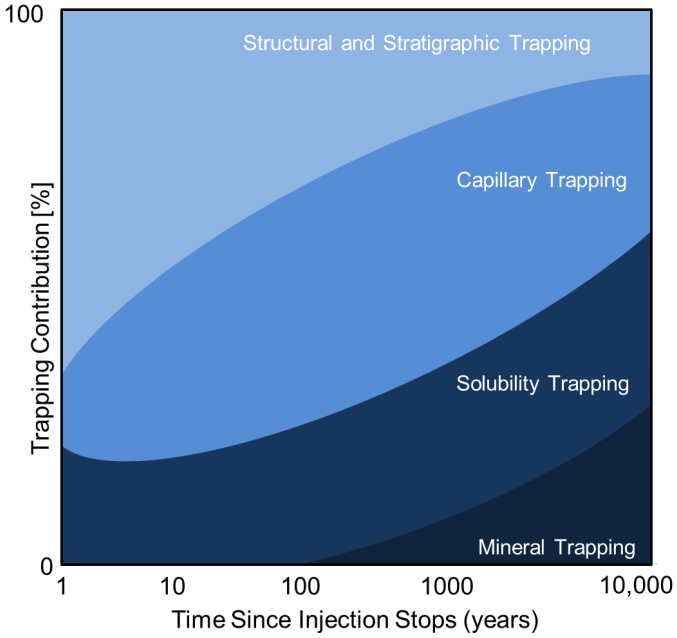

(b)

Figure 1.3. Illustration of (a) the level of security of the four trapping mechanisms of injecting CO_2 with out leakage and (b) the contribution of each trapping mechanism to the total CO_2 storage and the time dependency. These figures are adapted from [*Metz et al.*, 2005].

1.2. Oil Recovery

In oil reservoirs, we design the process to minimise the amount of capillary trapping of oil, hence maximising recovery. Generally speaking, oil production has three stages: primary, secondary, and tertiary. Primary recovery is when the oil comes out from the reservoir to the production well due to natural depletion of the reservoir pressure. Secondary recovery comes after primary recovery, and here water and/or gas are injected to flood the oil out of the reservoir. Tertiary recovery comes after secondary recovery and the aim is to try to recover more oil after secondary recovery.

The fluids injected in tertiary recovery are usually, surfactants, polymers, or CO_2 (called EOR) [*Lake*, 1989]. CO_2 can be injected in depleted oil reservoirs to displace the oil, while CO_2 remains in the reservoir. In addition, this process will maintain the reservoir pressure and production rates [*Dake*, 1983]. The IPCC considers CO_2 EOR as a form of underground CO_2 sequestration. In CO_2 EOR, storage occurs as CO_2 displaces hydrocarbons and the injected CO_2 is trapped within the reservoir's pore spaces through capillary forces and the other mechanisms discussed earlier. CO_2 EOR projects can be converted to CCS projects at the end of their operating lifetimes [*Metz et al.*, 2005].

1.3. Thesis Rationale

With over half of the world's conventional oil contained in fractured carbonate reservoirs, it is important that the fundamentals of fluid flow from fracture to matrix by spontaneous imbibition are understood [*Schlumberger*, 2013]. Spontaneous imbibition is one of the main recovery mechanisms in these reservoirs; in addition it is also the process rendering the non-wetting phase immobile in the reservoir. Also, reservoirs come in different wettability states and wettability is the prime factor affecting capillary trapping and thus the recovery and storage efficiencies, as we discuss later. To address this problem, we investigate recovery and trapping by spontaneous imbibition as well as waterflooding. Also, we investigate the effect of wettability on recovery rate and the amount of capillary trapping. In this thesis, we will study carbonate rocks, as they have received relatively little attention in the literature, despite their practical importance.

The aim of the thesis is to provide a set of benchmark experimental data on trapping, displacement and spontaneous imbibition on a well-characterised set of carbonate core samples. We will show that while we can explain and interpret the results in terms of pore-scale displacement processes, the results are very sensitive to the exact nature of the rock and the wettability. This thesis then acts as a guide to the types of experiment and analysis that is necessary to quantify the amount of trapping, imbibition and waterflood recovery under different conditions.

1.4. Capillary Trapping

Capillary trapping is the phenomenon of isolating the non-wetting phase by the wetting phase as trapped ganglia at the pore-scale. Capillary trapping is an important mechanism for storing CO_2/oil underground. Its understanding is important to reduce or recover the amount trapped for EOR, or maximise the amount stored for CCS. Figure 1.4 shows the process of storing CO_2 by capillary forces in a saline aquifer. In order to understand capillary trapping, we need to first understand immiscible displacement of two fluids in porous media and in particular, wettability, capillary pressure, and relative permeability.

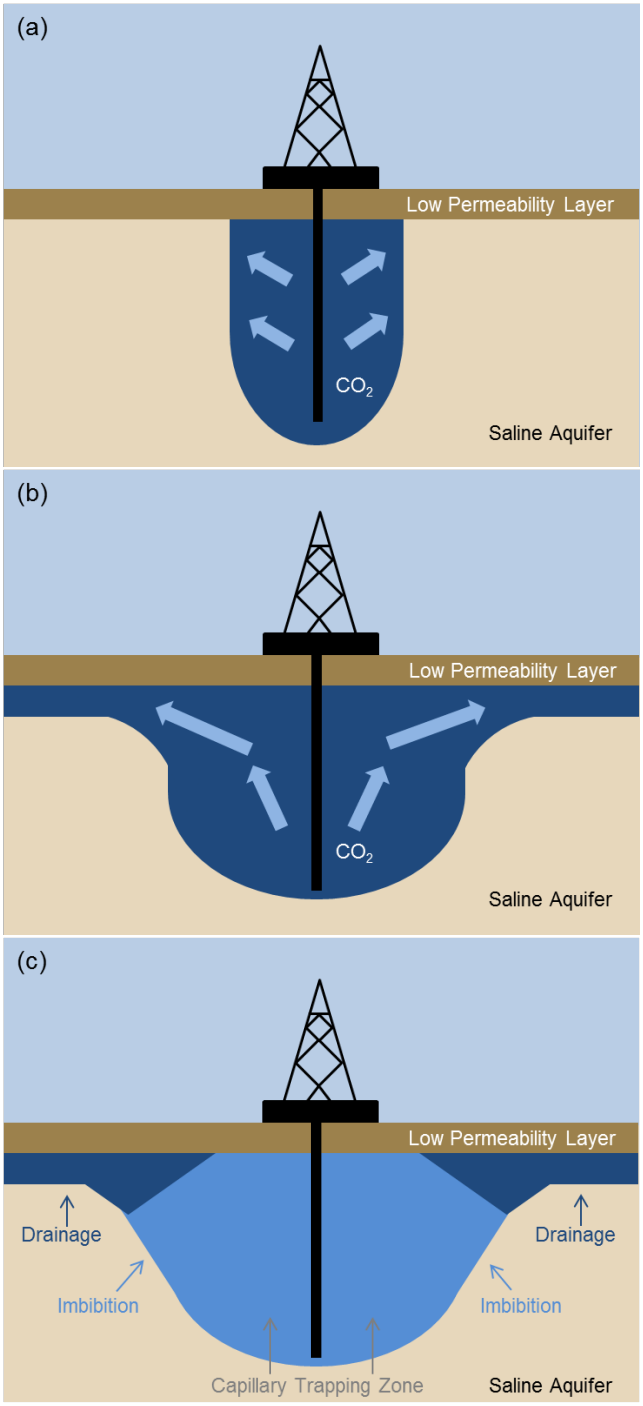

Figure 1.4. Schematic of CO_2 trapping by capillary forces in a saline aquifer (yellow) beneath a caprock (brown). We start (a) by injecting CO_2 underground where the CO_2 will be at its supercritical phase (a high density gas, dark blue), (b) the supercritical CO_2 will move upwards due buoyancy forces and then laterally when it reaches the caprock, and (c) the host brine will fill the supercritical CO_2 place and traps the supercritical CO_2 by capillary forces (light blue).

1.4.1. Wettability

Wettability is the preference of the solid to be in contact with one fluid in a system of two or more immiscible fluids [*Craig*, 1971]. In an oil-water reservoir, wettability can be divided into four categories:

(1) Water-wet, where the rock surface prefers to be coated with water and thus the rock has a high affinity to water, allowing water to spread on the surface and hence occupy the small pores.

(2) Intermediate-wet, where the surface has an almost equal tendency to be coated by one of the fluids either oil or water.

(3) Oil-wet, where the rock prefers to be in contact with oil.

(4) Mixed-wet, where parts of the rock prefer to be in contact with oil and the other parts prefer to be in contact with water.

Figure 1.5 shows contact angle measurements of a droplet of brine on a rock surface filled with oil with different wettability states. This measurement can give us a direct indication of the rock's wettability. However, the method requires a smooth surface which is not realistic as real rocks have rough surfaces with potentially very different effective contact angles [*Morrow*, 1975, *Morrow et al.*, 1994]. Table 1.1 shows the expected contact angle for each wettability state. Wettability has an impact on the residual saturation, spontaneous imbibition, capillary pressure, relative permeability, and electrical properties [*Anderson*, 1987]. Therefore, these properties can show us indirect indications of wettability.

The contact angle (θ) can be measured using the equilibrium of interfacial tension (σ) using Young's equation [*de Gennes et al.*, 2004]:

$$\cos\theta = \frac{\sigma_{S-O} - \sigma_{S-B}}{\sigma_{O-B}} \tag{1.1}$$

where subscripts: S, O, and B denote solid, oil, and brine respectively.

Due to the effect of hysteresis, which means history dependence, the contact angle of brine is different in drainage than imbibition, Figure 1.6. The reason for this inconsistency can be attributed to the chemical inhomogeneities and the roughness of the surface. On rough surfaces, the advancing contact angle θ_A in imbibition (increase in water saturation) is found to be larger than the receding contact angle θ_R in drainage (reduction in water saturation). The intrinsic contact angle θ_I is measured at rest on a smooth surface [*Morrow*, 1975]. Figure 1.7 shows contact angle hysteresis between the flooding cycles measured by *Morrow* 1975.

Another way to estimate the wettability of the rock at the macro-scale is by using an Amott test, *Amott* [1959]. This test quantitatively measures the wettability since the

amount spontaneously imbibed is a function of wettability. In this test we compare the recoverable amount of oil by spontaneous water imbibition to the amount recovered by forced water injection to give us the Amott water index, I_w. Similarly, we can estimate the Amott oil index, I_o, by comparing the amount of water recovered by spontaneous oil imbibition to the amount recovered by forced oil injection. Figure 1.8 shows schematics of the experimental Amott test for I_w and I_o.

To calculate the Amott indices, we use the following equations:

$$I_w = \frac{S_{wsi} - S_{wc}}{1 - S_{wc} - S_{or}} \tag{1.2}$$

$$I_o = \frac{S_{osi} - S_{or}}{1 - S_{wc} - S_{or}} \tag{1.3}$$

where I is the Amott index, S_{wsi} is the water saturation after spontaneous water imbibition, S_{wc} is the connate water saturation, S_{or} is the residual oil saturation, and S_{osi} is the oil saturation after spontaneous oil imbibition. Subscripts w and o denote water and oil respectively.

Strongly water-wet rocks would have an I_w of 1 and I_o of 0. More oil-wet rocks would have lower I_w and higher I_o. Mixed-wet rocks have I_w, $I_o > 0$–they spontaneously imbibe both oil and water. Intermediate-wet rocks would have $I_w \approx I_o \approx 0$.

To explain the intermediate behaviour further, if we consider the system has $\theta_I \approx 90^\circ$, then based on Figure 1.7 on contact angle hysteresis, we will have $\theta_A > 90^\circ$ and $\theta_R < 90^\circ$. This means that the medium is non-wetting to both water during waterflooding and oil in oil invasion leading to no spontaneous imbibition of either phase.

Clean reservoir rocks or minerals (quartz or calcite) tend to be water-wet coated with water layers. Once these minerals stay in contact with crude oil, due to oil migration, for sufficient time, the heavy polar components of the crude oil (resins and asphaltene) precipitate on the surface forming an oil layer making the rock more oil-wet [*Buckley*, 1995, *Buckley and Liu*, 1998]. In addition, the composition of brine, pH and composition of crude oil have significant impact on the wettability alteration process [*Buckley et al.*, 1996, *Buckley*, 2001]. Hence, most of the oil reservoirs in the world tend to be mixed-wet or intermediate-wet [*Anderson*, 1987, *Treiber and Owens*, 1972].

In this thesis, we use the term "altered-wettability" to refer to a rock which has been in contact with oil: it may be weakly water-wet, intermediate-wet, mixed-wet, or oil-wet. Figure 1.9 shows the possible configuration of oil and water saturations in water-wet, mixed-wet and oil-wet porous media. The applications of wettability can be viewed in our daily life. For instance, rain coats, umbrellas, wool on sheep and even ducks' feathers are made to be oil-wet in order to repel water and prevent it from soaking into the material by spontaneous imbibition. On the other hand, towels and tissues, in general, are made to be water-wet to soak up water.

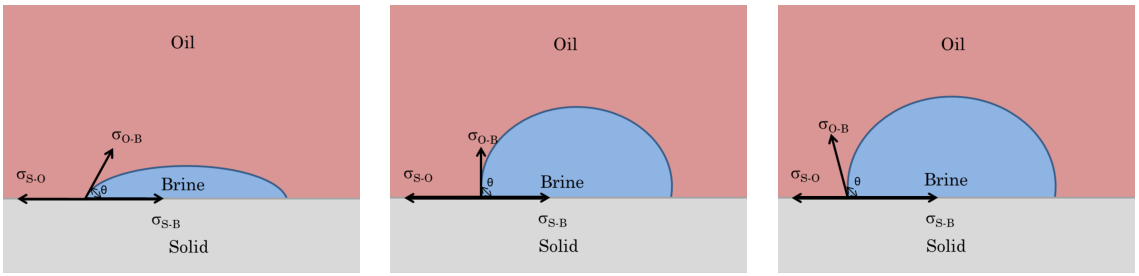

(a) (b) (c)

Figure 1.5. Contact angle measurement on a solid surface on (a) water-wet, (b) intermediate-wet, and (c) oil-wet solids.

Table 1.1. Wettability classification based on the contact angle of the water droplet on a rock surface.

Wettability State	θ [°]
Water-wet	<90
Intermediate-wet	≈90
Oil-wet	>90

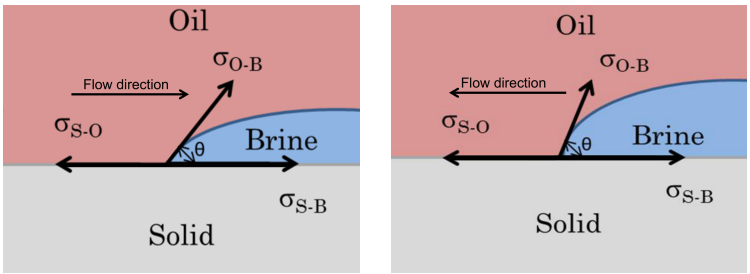

(a) (b)

Figure 1.6. Contact angle hysteresis, depending on the flow direction, on a solid surface during (a) drainage with the receding contact angle (denser phase receding) and, (b) imbibition with the advancing contact angle (denser phase advancing).

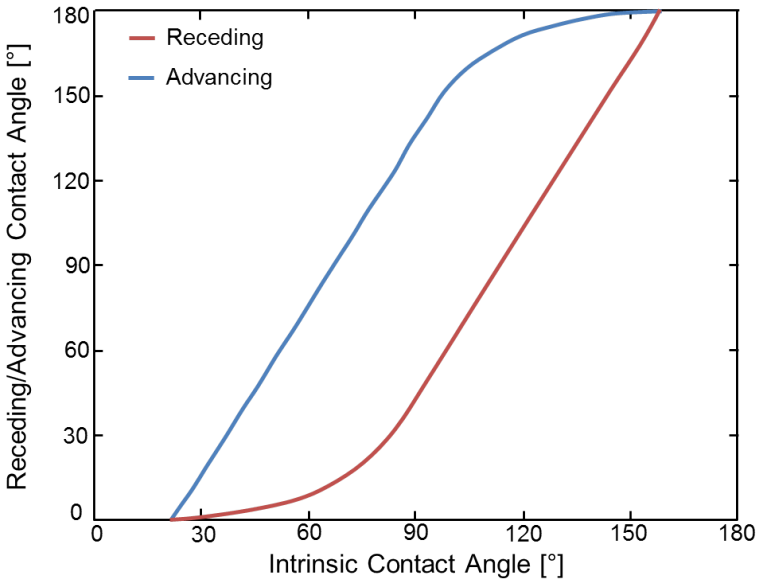

Figure 1.7. Relationship between intrinsic contact angle and the advancing and receding contact angles, measured by *Morrow* 1975.

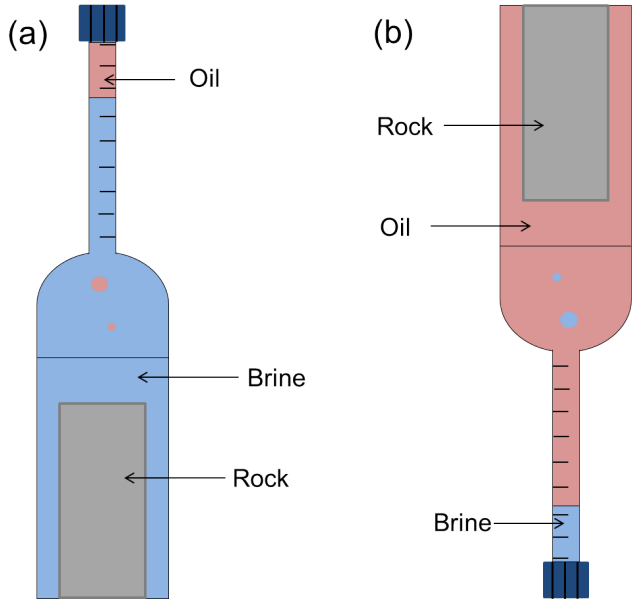

Figure 1.8. Schematic of the Amott experimental test with (a) the Amott water index where we place a rock filled with oil and water into the cell. We fill the cell with brine and then the rock will spontaneously imbibe water and will displace the oil upwards due to buoyancy forces. Then we measure the amount of oil recovered by spontaneous imbibition and compare to the waterflood recovery to obtain the Amott water index, Equation 1.2. Similarly for the Amott oil index (b) which is opposite to the water index, we fill the cell with oil and the oil will displace the water for mixed-wet and oil-wet systems. Here we show the cell to be inverted as brine is denser than oil and will travel downwards.

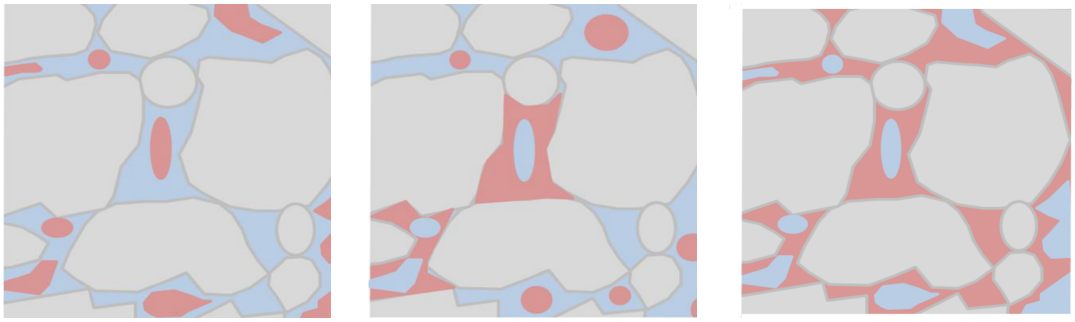

(a) water-wet (b) mixed-wet (c) oil-wet

Figure 1.9. Possible water and oil distribution in (a) a water-wet system where oil (red) remains in the centre of the pores and fills the large pores. (b) A mixed-wet system where oil has displaced water (blue) from some surfaces but still trapped in the center of the water-wet regions. (c) An oil-wet system where water remains in the centre of the pores and fill the large pores while the oil surrounds the water.

1.4.2. Capillary Pressure

Capillary pressure is the pressure difference across the interface of two immiscible fluids. In other words, it is the difference between the non-wetting phase and the wetting phase and from the Young-Laplace equation:

$$P_c = P_{nw} - P_w = \sigma \left(\frac{1}{R_1} + \frac{1}{R_2} \right) \tag{1.4}$$

where P_c is the capillary pressure, P_{nw} is the non-wetting phase pressure, P_w is the wetting phase pressure, σ is the interfacial tension, and R_1 and R_2 are the principal radii of curvature of the interface.

Capillary pressure can be divided into drainage (non-wetting phase increasing saturation) and imbibition (wetting phase saturation increasing) and can be measured using the Porous Plate (PP) technique, centrifuge, dynamic/semi-dynamic methods, and Mercury Injection Capillary Pressure (MICP) [*Tiab and Donaldson*, 2011, *Lenormand et al.*, 1995, *Pini et al.*, 2012].

Drainage

Drainage is the displacement of the wetting phase by the non-wetting phase. The displacement is opposed to the adhesion force. Therefore, it is not spontaneous. The non-wetting phase advances in a connected piston-like displacement in the porous medium [*Tiab and Donaldson*, 2011].

When oil migrates from the source rock into a brine saturated reservoir, this process is primary drainage, Figure 1.10. Since oil migration is upward due to the buoyancy

forces between the oil and the host brine, it displaces the brine downwards or laterally depending on the local heterogeneity. The oil invades the larger pores first and then progressively smaller pores as it progress until the brine reaches a connate water saturation where the water saturation cannot be reduced any further regardless of an increase in the applied capillary pressure. At this stage, the water will be squeezed in the corners of the pore spaces coating the surface of the rock in the form of layers. The injection of CO_2 in brine aquifers for storage is also a drainage process as the CO_2 (non-wetting phase) displaces brine (wetting-phase).

An oil/brine reservoir may have several wettability states which can be correlated to the drainage capillary pressure. After primary drainage, surface-active compounds in the oil may adhere to the solid surface changing the wettability of the system for subsequent water invasion as discussed previously. For instance, mixed-wet wettability behaviour tends to be located within the Transition Zone (TZ) in the reservoir, which is a zone between the oil/water contact (OWC) to where the water saturation is at or near its irreducible value. The wettability in the transition zone is mixed-wet with a higher fraction of water-wet areas near the OWC, and becomes less water-wet as we reach the top part of the oil reservoir since most of the rock surface is contacted by oil [*Masalmeh et al.*, 2007], Figure 1.11.

In this thesis, we will study rocks with different initial saturation and wettability. These features influence oil recovery by water injection [*Jadhunandan and Morrow*, 1995].

The drainage capillary pressure curve is a function of the rock type (different permeability and pore structure), different rock types have different capillary pressure curves, Figure 1.12.

Capillary pressure can be expressed in dimensionless form, which takes account for different interfacial tensions and average pore size (Leverett J-function) [*Tiab and Donaldson*, 2011]. This expression is used to scale laboratory data that may be performed with different fluid pairs and condition, than the field condition. The Leverett J-function is written as follows:

$$J(S_w) = \frac{P_c}{\sigma \cos\theta} \sqrt{\frac{k}{\phi}} \tag{1.5}$$

where $J(S_w)$ is the dimensionless J-function, P_c is capillary pressure [Pa], σ is interfacial tension (0.48 N/m for mercury/air system), θ is the contact angle (40° for mercury/air system, measured through air), ϕ is porosity, and k is permeability [m^2]. Figure 1.13 shows the J-function of the drainage capillary curves in Figure 1.12.

From the mercury injection test, we can relate the capillary pressure to the pore size distribution. First, we use Equation 1.4 to convert the capillary pressure to throat radius, assuming piston-like displacement into a circular tube. This assumption is not realistic in describing the rock; however, it is a common practice in the petroleum industry. We can, for non-circular pores, assume that the radius represents the inscribed radius of the

pore. Then, we define an effective radius, r_p, as a function of saturation:

$$r_p = \frac{2\sigma \cos\theta}{P_c(S_w)} \tag{1.6}$$

This can be further interpreted by using the probability distribution function (f) of a pore entry radius (r_p):

$$r_p f(r_p) = r_p \frac{dS_w}{dr_p} = -P_c \frac{dS_w}{dP_c} = -\frac{dS_w}{dlnP_c} \tag{1.7}$$

This is an approximate relation as it assumes that the throats are circular in cross-section and assigns all the change in saturation–which may be due to subsequent filling of layer regions–to that throat size.

Figure 1.14 shows the pore entry distribution for the rocks used in Figure 1.12. The terms homogeneous and heterogeneous rocks are based on the pore size distribution in Figure 1.14. We can see that both homogeneous rocks have a uni-modal distribution while the heterogeneous rock has a bi-modal distribution of pore size. In this thesis, the emphasis will be on carbonates which are heterogeneous with, typically, a bi-modal pore size distribution.

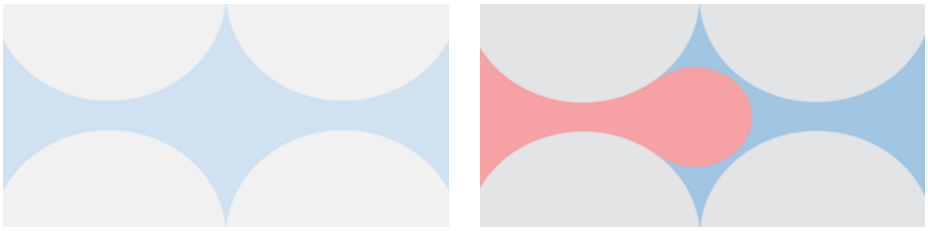

(a) (b)

Figure 1.10. Pore-scale representation of showing (a) a brine reservoir before oil migration and (b) oil displacement in primary drainage.

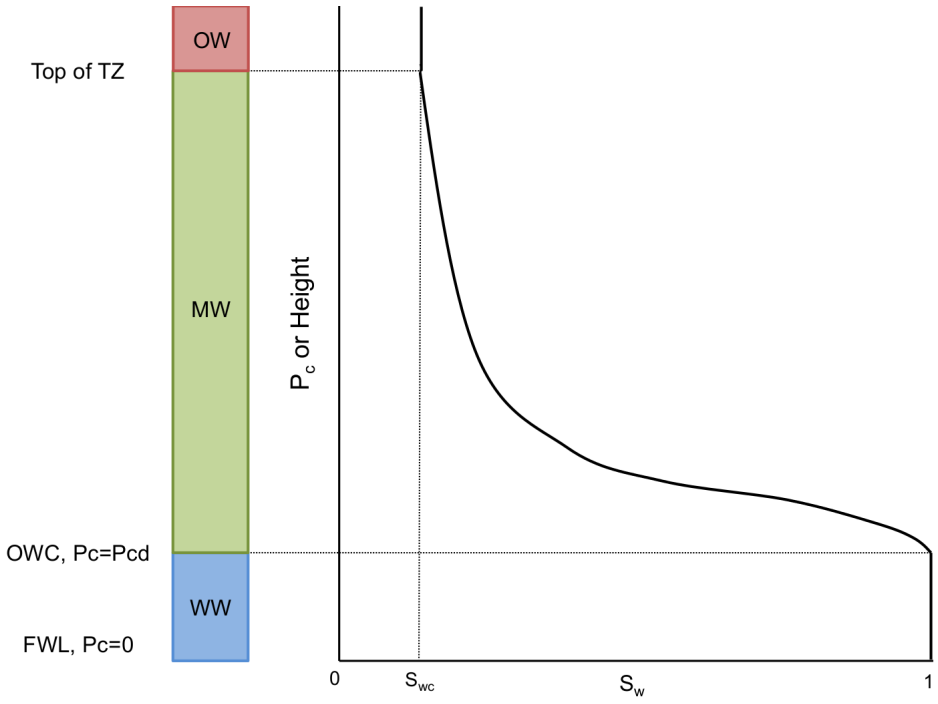

Figure 1.11. Schematic diagram to show the wettability distribution in the reservoir based on the drainage capillary pressure.

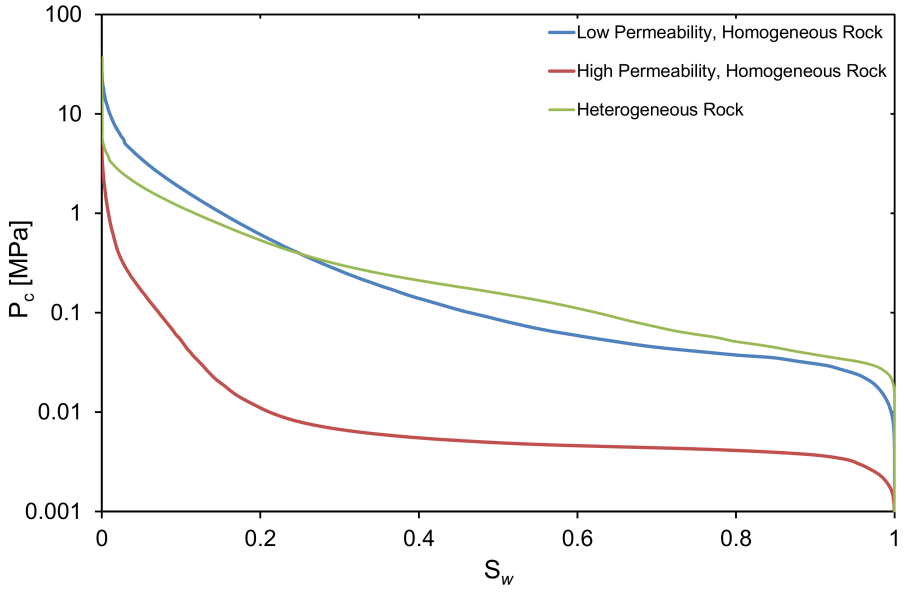

Figure 1.12. Different drainage capillary pressure curves based on different rock properties from mercury injection capillary pressure (MICP) measurements. The low permeability, homogeneous rock is Springwell sandstone with a porosity, ϕ of 17% and mercury absolute permeability, $k_{Hg} = 3 \times 10^{-14}\text{m}^2$, The high permeability, homogeneous rock is Doddington sandstone with ϕ of 21% and k_{Hg} of $1 \times 10^{-12}\text{m}^2$, The heterogeneous rock is Indiana limestone with ϕ of 14% and k_{Hg} of $1 \times 10^{-14}\text{m}^2$. These results were obtained from Weatherford Laboratories at East Grinstead, UK.

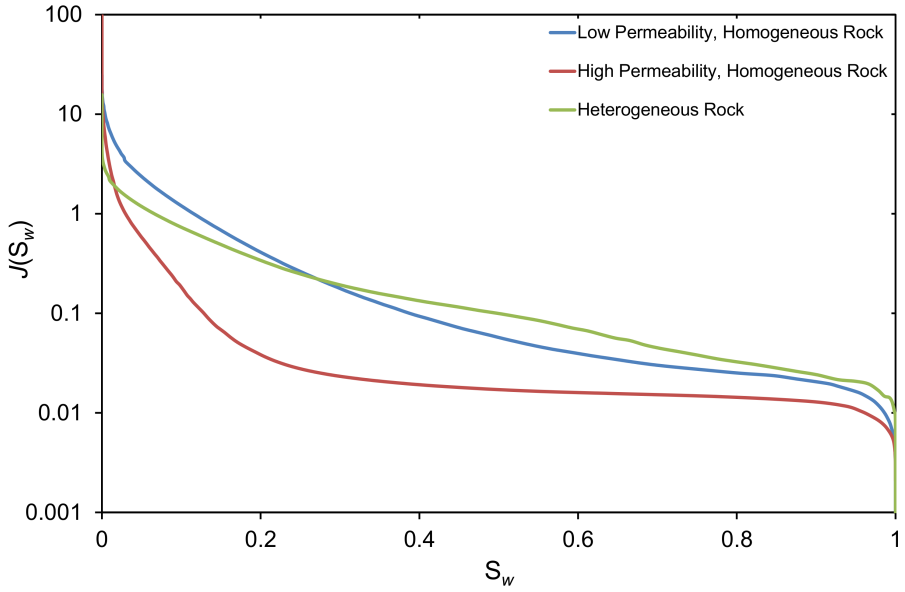

Figure 1.13. Capillary pressure J-function versus saturation for the rocks used in Figure 1.12.

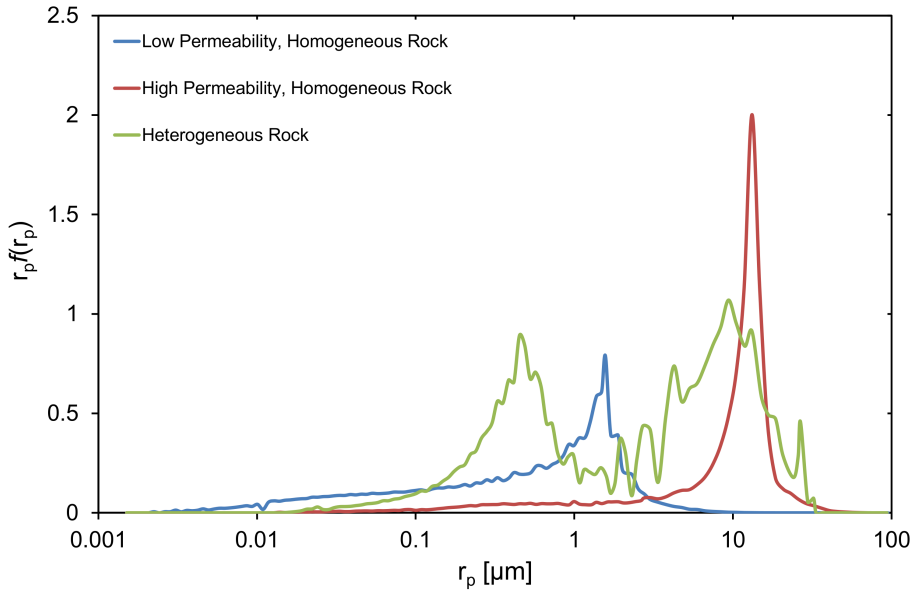

Figure 1.14. The pore size distribution against pore throat radius for the rocks used in Figure 1.12.

Water Re-saturation

Water re-saturation can be divided into two parts: imbibition and forced displacement. Imbibition is the opposite process to drainage and here the wetting phase displaces the non-wetting phase. During forced displacement it no longer makes sense to refer to the invading phase as wetting, as the capillary pressure is now negative. To emphasise this, we often refer to imbibition as spontaneous since $P_c > 0$ and water is at a lower pressure than oil. When $P_c < 0$ we have forced displacement where water is at a higher pressure than oil.

Spontaneous Imbibition

Spontaneous water imbibition is the invasion of the water into a porous medium due to capillary forces and can only occur in water-wet and mixed-wet systems [*Morrow and Mason*, 2001]. Spontaneous imbibition can occur in two different modes: co-current and counter-current. Co-current is when the brine and oil flow in the same direction, Figure 1.15a. Counter-current imbibition occurs when the oil and brine flow in opposite directions from the same inlet, Figure 1.15b. In the reservoir, counter-current displacement will dominate if matrix blocks are completely surrounded by water; however, if the rock matrix blocks are not fully surrounded by water and if gravity segregation occurs, then co-current is the dominant flow [*Bourbiaux and Kalaydjian*, 1990, *Pooladi-Dravish and Firoozabadi*, 2000]. The rate of water imbibition into the porous medium is a function of permeability, relative permeability, capillary pressure, initial water saturation, boundary conditions, viscosity, interfacial tension, and wettability [*Zhang et al.*, 1996, *Graue and Fernø*, 2011, *Mason and Morrow*, 2013].

In spontaneous imbibition, it is possible to render the non-wetting phase immobile by the wetting phase. The trapped non-wetting phase is called the residual saturation. There are two mechanisms of achieving residual saturation: a) piston-like advance and b) snap-off [*Lenormand et al.*, 1983].

Piston-like advance occurs when the invading wetting phase moving from a wetting-filled pore, large gap between grains, or throat, narrow restriction connected to pores, displaces the non-wetting phase from neighbouring pore or throat, Figure 1.16. This mechanism is favoured in the narrow throats but impeded in the wide pores, since water wants to be in the narrow regions of the pore space.

The threshold capillary pressure for this mechanism is approximately:

$$P_c = \frac{2\sigma \cos\,\theta}{r} \tag{1.8}$$

where P_c is the threshold capillary pressure for piston-like advance, σ is the interfacial tension, θ is the contact angle, and r is the radius of the pore or throat being filled.

Since the capillary pressure is inversely proportional to the radius, then larger pores will require lower capillary pressure to fill them. In imbibition following drainage, the water fills the pore space in decreasing order of capillary pressure. In other words, water fills the narrowest throats with the highest capillary pressure first. However, the constraint is that the water cannot invade a throat unless the neighbouring pore or throat is water-filled.

Snap-off occurs in water-wet media when wetting layers in the corners swell–in a narrow throat– until the non-wetting phase loses contact with the solid surface resulting in a rapid invasion of the throat, Figure 1.17.

The threshold capillary pressure for this mechanism for a throat of square cross-section and inscribed radius r_t:

$$P_c = \frac{\sigma(\cos\,\theta - \sin\,\theta)}{r_t} \tag{1.9}$$

The ratio of the capillary pressure for snap-off to piston-like advance is:

$$\frac{r}{2r_t}(1 - \tan\,\theta) \tag{1.10}$$

The ratio demonstrates that the mechanism with the highest capillary pressure is favoured for large aspect ratio, the ratio of the pore radius to throat radius, and $\theta < 90°$ (a water-wet system). Snap-off fills narrow throats, leaving non-wetting phase in the large pores. The non-wetting phase will be trapped, if all the surrounding throats are filled. On the other hand, piston-like advance has the tendency to fill pores with water if the neighbouring throats are filled with water leading to little trapping [*Lake*, 1989, *Lenormand and Zarcone*, 1984]. For this reason, we see most trapping in strongly water-wet rocks. There will be less trapping in intermediate-wet rocks with $\theta \approx 90°$, since snap-off will not be favoured: in Equation 1.9, P_c must be positive for the process to occur which requires $\theta < 45°$.

There are many examples of spontaneous imbibition from our daily life. For example, the process when tissue paper soaks water even without applying any force. Another example, when we add sugar cubes to coffee (we ignore the dissolution process) we see air bubbles produced on the surface of the coffee and that because the coffee (water based) imbibes into the sugar cube (porous medium) and replaces the air inside the system.

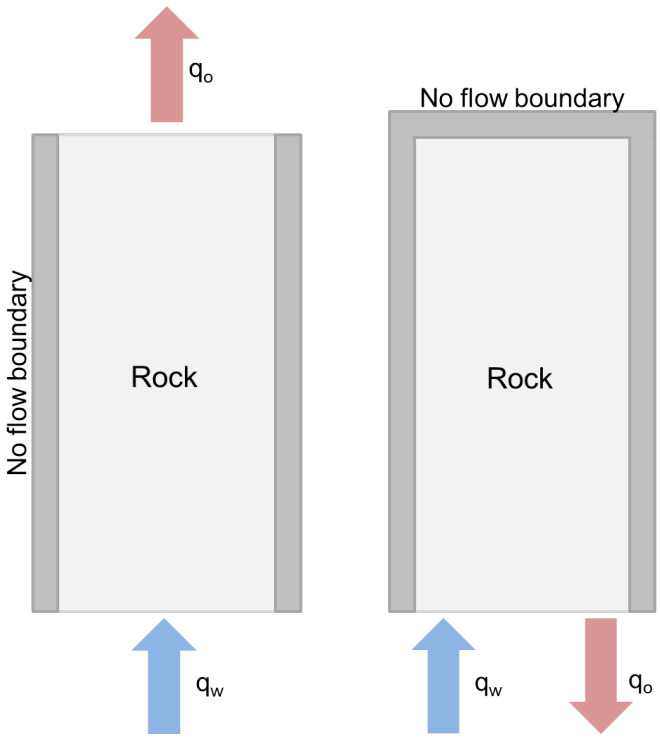

Figure 1.15. Schematics representing spontaneous water imbibition under (a) co-current imbibition and (b) counter-current conditions.

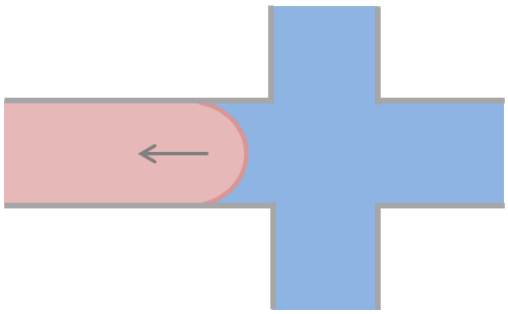

Figure 1.16. Schematic of piston-like advance in square capillaries. This figure is reproduced from *Lenormand and Zarcone* 1984.

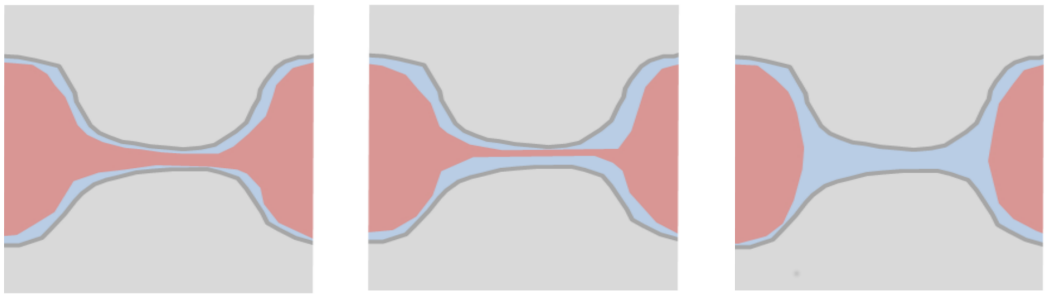

(a) (b) (c)

Figure 1.17. Schematic of oil distribution in a pore at (a) after drainage when oil is well connected, (b) at the early time of imbibition where the water layers swell, and (c) after long imbibition time of water where the oil totally disconnects to become trapped in the pore due to snap-off.

Forced Displacement

Forced displacement or waterflooding occurs after spontaneous imbibition to recover the oil that was not recovered by spontaneous imbibition. In forced displacement, we need to inject water at a higher pressure than oil to displace the oil thus yielding a negative capillary pressure, Equation 1.2. Forced displacement behaviour is different depending on the wettability of the rock and the initial saturations.

For a water-wet system, the displacement is simple, the water will flow in the narrow throats leaving the oil stranded in the large pores. The residual oil saturation can be achieved in the spontaneous imbibition phase. However, in a weakly water-wet system, we will observe additional oil recovery by forced displacement leading to lower residual oil saturation.

As the system becomes more oil-wet, oil layers are formed. We now expect oil to be in the narrow throats while the water will be in the large pores as water is the non-wetting phase, leaving the wetting oil as a layer sandwiched between water in the center of the pore and water is retained in the corners after primary drainage, Figure 1.18. In order to collapse these oil layers, a sufficient water pressure is required. This gives slow oil layer drainage during forced displacement. We refer to a remaining saturation, rather than a residual saturation as more oil is slowly recovered as more water is injected. Acquiring the residual state will require thousands of water pore volumes to be injected [*Salathiel*, 1973]. Since the snap-off trapping mechanism does not occur in an oil-wet system, we expect higher oil recovery and less trapping than a water-wet system.

With a high initial oil saturation, water is forced right into the corners of the pore space, giving more stable layers and less trapping than for lower initial saturation, Figure 1.18. This is one explanation for the non-monotonic trapping curve presented in Chapter 4.

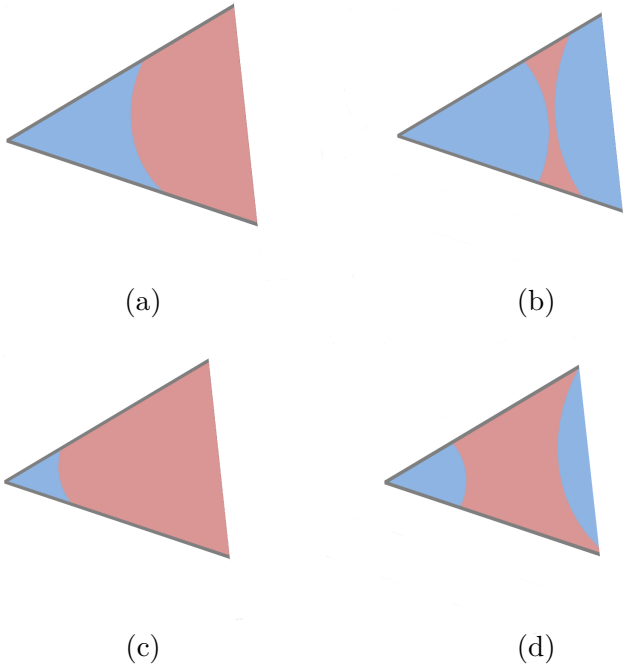

Figure 1.18. Schematic of different possible saturation configurations in an oil-wet pore. (a) For a low initial oil saturation, after waterflooding we see a thin oil layer that will collapse with a small increase in water pressure (b). (c) For a high initial oil saturation, in contrast, after waterflooding the oil layer is fatter and more stable (d).

Capillary and Bond Numbers

Multi-phase flow in porous media is governed by the interplay between capillary, viscous, and gravitational forces [*Wong et al.*, 1999]. The capillary number is the ratio of capillary to viscous forces. The capillary number is defined as:

$$N_{Ca} = \frac{q\mu}{\sigma} \tag{1.11}$$

where q is the Darcy velocity of the fluid [m/s], μ is the viscosity of the fluid [mPa s], and σ is the interfacial tension [N/m]. Typical capillary number values for the field-scale displacement are 10^{-8} to 10^{-6} [*Chatzis and Morrow*, 1984]. Generally, of these two forces, capillary forces dominate at the pore scale where viscous forces dominate in the large (inter-well) scale. Our experiments were run at low capillary numbers 10^{-8} giving capillary-controlled conditions. Viscous forces suppress snap-off and mobilise ganglia, leading to less trapping.

The Bond number is the ratio of the gravity to capillary forces. The Bond number affects vertical flood experiments and is defined as:

$$N_{Bo} = \frac{\Delta\rho g k}{\sigma} \tag{1.12}$$

where $\Delta\rho$ is the density difference between the displacing and displaced phases [kg/m^3], g is the acceleration due to gravity [9.8 m/s^2], k is the absolute permeability [m^2], and σ is the interfacial tension [N/m]. Again, typically $N_{Bo} \ll 1$ in reservoir displacements.

Waterflood Capillary Pressure Curves

There are different behaviours of waterflood curves depending on the wettability of the rock [*Anderson*, 1987]. For a **water-wet rock**, Figure 1.19a, we start from primary drainage where the capillary pressure is positive and the water saturation has reached its connate/irreducible water saturation (S_{wc}/S_{wir}) which will have a negligible reduction in saturation regardless of any higher pressure that is applied. This is the same initial condition regardless of the wettability of the rock during waterflooding. During waterflooding, the water imbibes into the rock spontaneously, with no force required if the rock remains water-wet, until the capillary pressure reaches zero. For water-wet media, most or all of the oil will be recovered during spontaneous imbibition. Then, when we apply pressure to force the oil out, very little additional oil will be recovered.

For an **intermediate-wet rock**, Figure 1.19b, there is little or no oil recovery by spontaneous water imbibition since the rock has neutral affinity to water, followed by significant recovery by forced water injection. There is less trapping, as there is little or no snap-off, but oil can be surrounded by water as the non-wetting phase, leaving some residual saturation.

For an **oil-wet rock**, Figure 1.19c, there are only well-connected oil-wet pathways yielding no recovery by a spontaneous water imbibition, followed by significant recovery by forced water injection.

For a **mixed-wet rock**, Figure 1.19d, we have both well-connected water-wet and oil-wet pathways resulting in medium oil recovery by spontaneous water imbibition followed by significant further recovery by forced water injection.

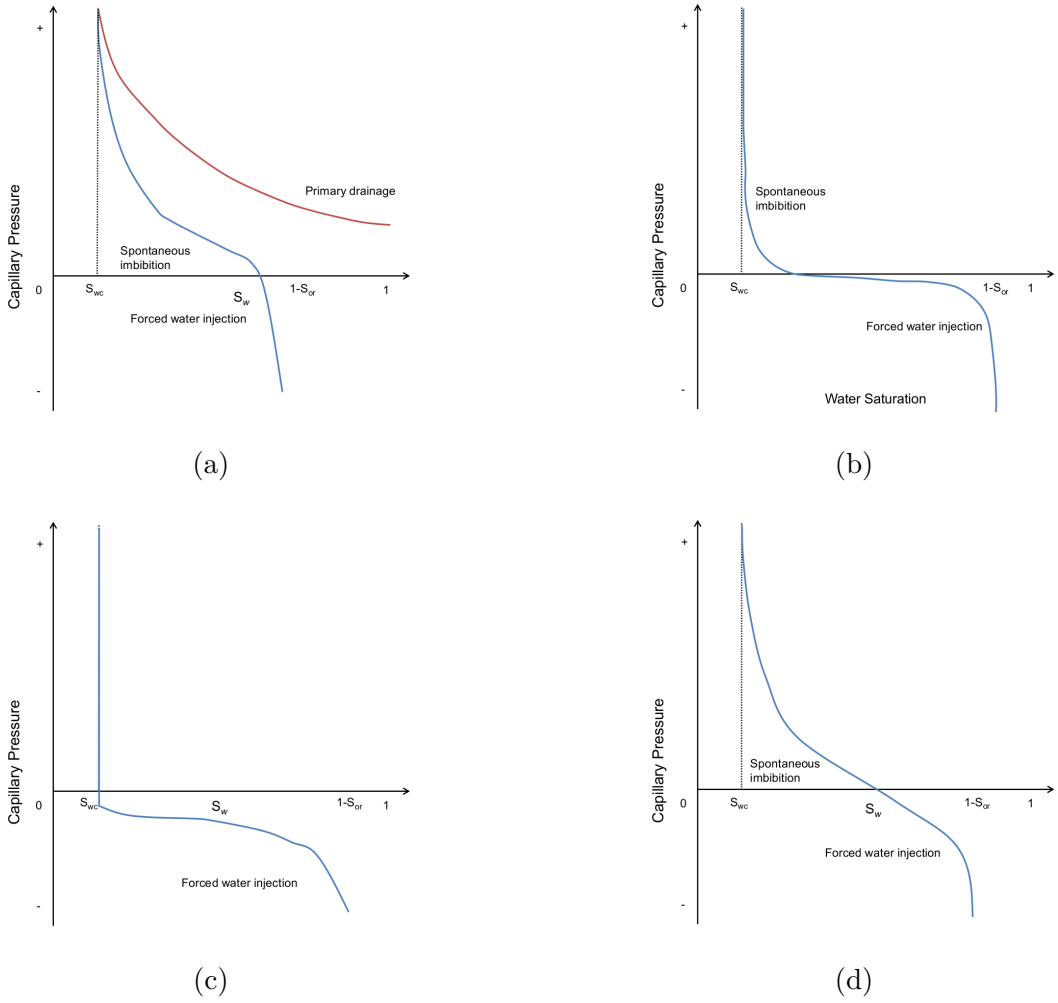

Figure 1.19. Schematic exemplar waterflood capillary pressure curve for (a) a water-wet rock, (b) an intermediate-wet rock, (c) an oil-wet rock, and (d) a mixed-wet rock.

1.4.3. Relative Permeability

Relative permeability is the ratio of the effective permeability, which is the permeability of one fluid in the presence of another fluid, to the absolute permeability. There are three main factors affecting relative permeability: pore geometry, wetting properties, and fluid saturation. Relative permeability is essential to understand oil recovery and thus plan proper injection schemes. There are two ways of measuring relative permeability (a) steady state method or (b) unsteady state (displacement method).

To define the relative permeability, we need to extend Darcy's law to multiple phases:

$$q_w = -\frac{kk_{rw}}{\mu_w}\left(\nabla P_w - \rho_w g\right) \tag{1.13}$$

$$q_o = -\frac{kk_{ro}}{\mu_o}\left(\nabla P_o - \rho_o g\right) \tag{1.14}$$

where q is the Darcy flow rate per unit area [m/s], k is the absolute permeability [m^2], k_r is the relative permeability, ∇P is the pressure gradient [Pa/m], μ is the viscosity [Pa.s], ρ is the density of the fluid [kg/m^3], and g is the gravitational force constant which is 9.8 [m/s^2]. Subscripts w and o denote water and oil respectively.

Relative Permeability Curves

Similar to capillary pressure, relative permeability is also a function of wettability [*Anderson*, 1987]. For a **water-wet system**, Figure 1.20a, the water relative permeability is lower than the oil relative permeability because water fills the narrow pores while the oil fills the large pores, giving the water poor connectivity. For the same reason, oil has higher relative permeability than water, as oil fills the large pores giving good connectivity. The residual oil saturation is high though, since oil can be trapped in the centres of the larger pore spaces by snap-off, as discussed earlier. This is discussed further in the next section.

For an **intermediate-wet system**, Figure 1.20b, both oil and water have comparable relative permeabilities since the surface has equal tendency to be coated by either fluid.

For an **oil-wet system**, Figure 1.20c, it is the reverse of the water-wet scenario where oil has a lower relative permeability than water since oil will now fill the narrow pores. Water, on the other hand, will fill the large pores giving low flow conductance to oil. However, the oil remains connected in layers until a low residual saturation is reached.

For a **mixed-wet system**, Figure 1.20d, the behaviour is characterised by low oil and water relative permeabilities and also low residual oil saturation. This can be explained by the low conductance of oil layers, and because it is hard for water to flow across different wettability fractions [*Gharbi and Blunt*, 2012].

Oil-wet and mixed-wet rocks tend to have lower S_{or} than water-wet rocks since oil layers maintain connectivity, see Figure 1.18, however, there will be continued, slow production after water breakthrough even after 5000 pore volumes of water injected [*Salathiel*, 1973]. This contrasts with water-wet rocks where residual saturation is reached at breakthrough or after a few pore volumes injected [*Abdallah et al.*, 1986]. For intermediate-wet rocks, S_{or} can also be low since snap-off is suppressed. From the capillary trapping perspective which is the trapping of the non-wetting phase by the wetting phase: in the oil-wet and the mixed-wet cases with oil layers, little oil will be trapped, while on the other hand, water will be trapped during secondary oil injection, since it is the non-wetting phase.

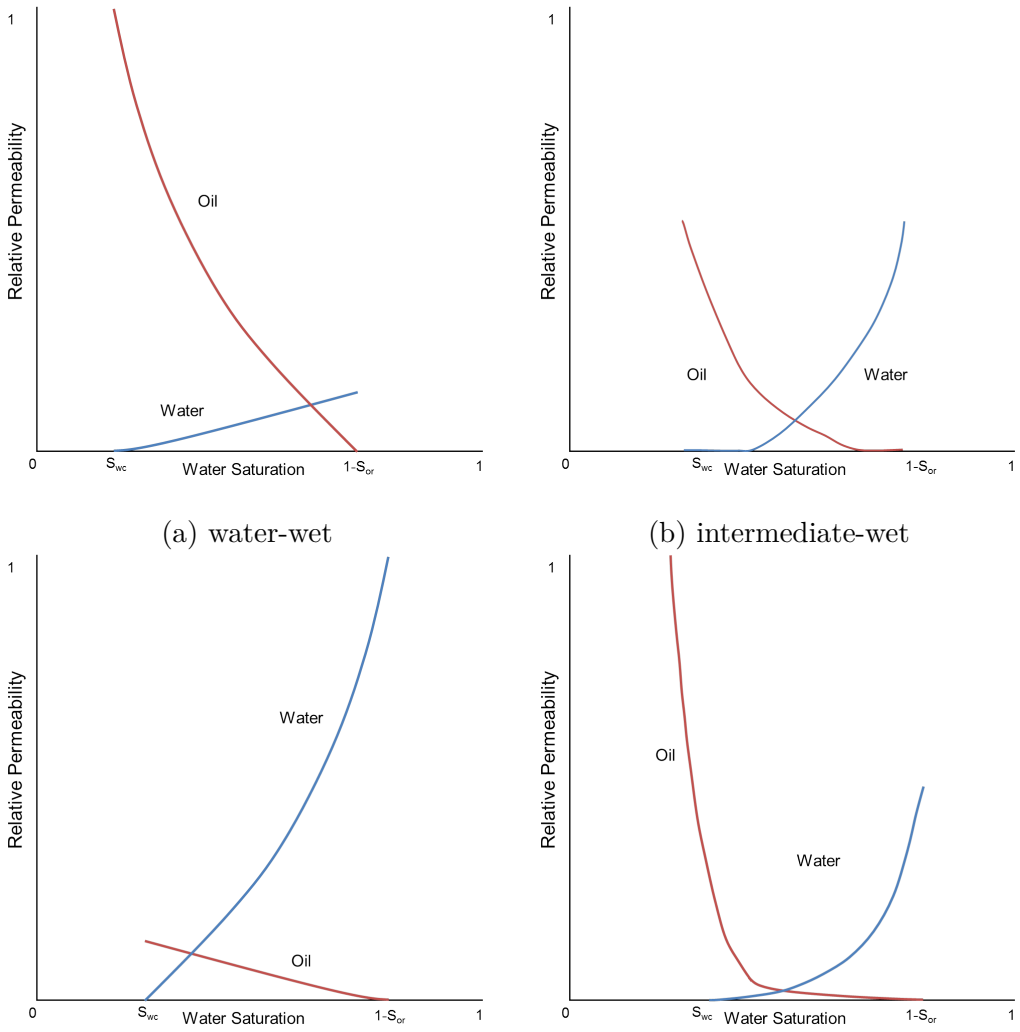

(a) water-wet

(b) intermediate-wet

(c) oil-wet

(d) mixed-wet

Figure 1.20. Schematic exemplar waterflood relative permeabilities for (a) water-wet, (b) intermediate-wet, (c) oil-wet, and (d) mixed-wet rocks.

1.5. Capillary Trapping Laboratory Methods

There are several labratory methods where we can measure the trapping curve which is the relationship between the initial non-wetting phase saturation (S_{nwi}) to residual non-wetting phase saturation (S_{nwr}). These methods include: centrifuge, unsteady state, steady state, and porous plate.

1.5.1. Centrifuge Method

In this method, we can measure the drainage and waterflood capillary pressure curves. For drainage, we place a core sample filled with the wetting phase and place it in a cell surrounded by the non-wetting phase, Figure 1.21a. We centrifuge the cell at several speeds starting from low to high. At each speed, we measure the amount of fluid displaced during the process until we see no further production at high speeds [*Tiab and Donaldson*, 2011]. For the waterflood capillary pressure curve, the cell will be reversed compared to drainage as the oil phase is usually less dense than water, Figure 1.21b.

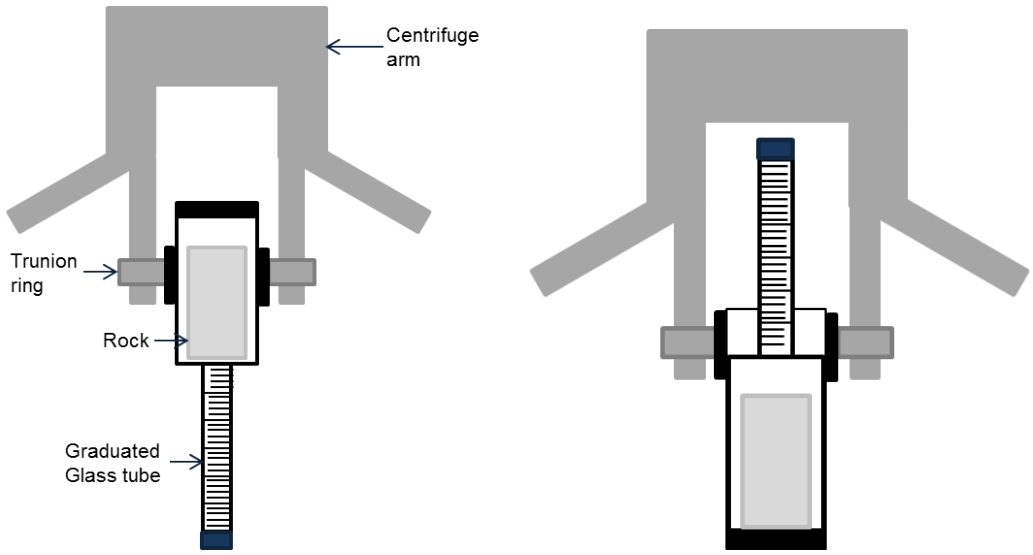

Figure 1.21. Schematic of the centrifuge laboratory method where (a) is the position to measure the oil displacing water capillary pressure while (b) is the position to measure the water displacing oil capillary pressure curve.

1.5.2. Unsteady State (USS) Method

In an unsteady state measurement, Figure 1.22, the rock or the core is saturated with one fluid (water or oil) and then the other fluid is injected to displace the first fluid. During unsteady state displacement, the flow rates of both fluids and pressure drop are recorded. Applying this method is cheap and relatively quick; however, this method

requires interpretation of the results, since relative permeability, is not measured directly [*Dullien*, 1991]. However, if this method is used strictly to achieve the trapping curve, then the method becomes simpler and less time consuming.

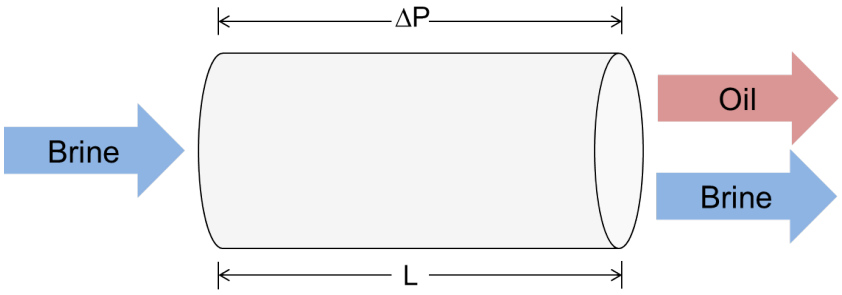

Figure 1.22. Schematic of an unsteady state waterflood coreflood relative permeability experiment.

1.5.3. Steady State (SS) Method

In the steady state approach, both fluids are injected simultaneously; the flow rate and pressure drop are measured to find the relative permeability, Figure 1.23. This method is primarily used to measure the relative permeability [*Tiab and Donaldson*, 2011]. Nevertheless, the trapping curve can be achieved as a by-product and does not require additional steps.

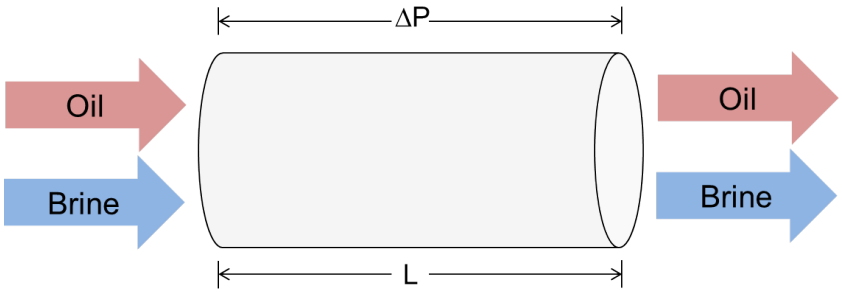

Figure 1.23. Schematic of a steady state coreflood relative permeability experiment.

1.5.4. Porous Plate (PP) Method

In this thesis, we mainly perform capillary trapping experiments using a porous plate (PP, which is a low permeability water-wet ceramic disc, this disc will retain the oil in the core and will let the water pass through the outlet) to establish various initial saturations and eliminate the capillary end effect which is a saturation gradient from the inlet to the outlet of the core [*Lamy et al.*, 2010, *Pentland et al.*, 2011, *El-Maghraby and Blunt*, 2013, *Tanino and Blunt*, 2013]. The advantages of using the PP technique is

the ability to establish low initial saturations compared to the unsteady state technique, and also to establish a homogeneous distribution of saturation inside the rock. The disadvantage of this method is that it is time consuming. The experimental procedure of this experiment is similar to the work of *Pentland et al.* 2010 and it is as follows:

(1) Saturate the rock with 100% water saturation, Figure 1.24a.

(2) Insert the PP at the downstream face of the rock and inject the oil in the upstream face at a constant capillary pressure, Figure 1.24b.

(3) When there is no further water production in step 2, the initial oil saturation is achieved, then, remove the PP and inject brine at a very low flow rate to ensure capillary dominated flow is applied to reach the residual oil saturation, Figure 1.24c.

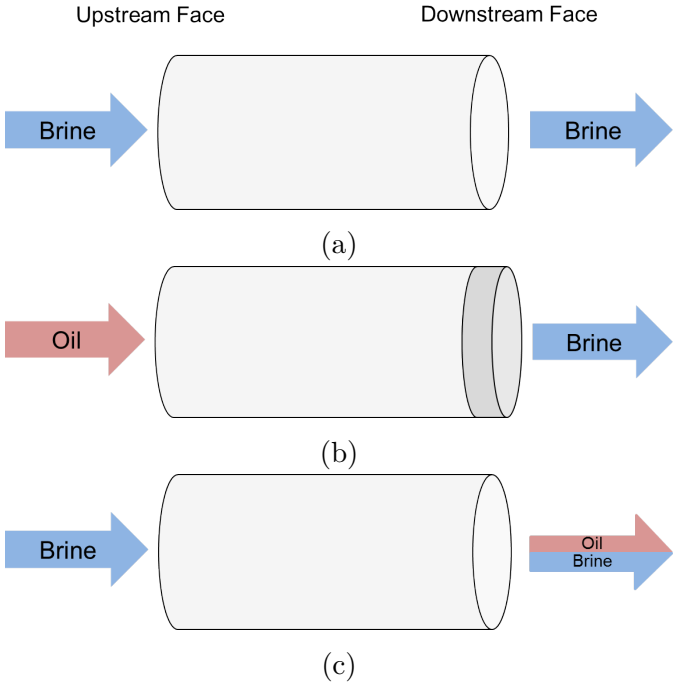

Figure 1.24. Schematic of a capillary trapping coreflood experiment where we start with (a) saturating the core with 100% brine, followed by (b) inserting a water-wet porous plate disc at the downstream of the core to retain the oil and let the brine pass. Then we inject oil at a constant capillary pressure until no further water is produced. Finally, (c) we waterflood the core at a low capillary dominated flow rate.

If we look at the capillary trapping experiment from the capillary pressure perspective, Figure 1.25, we can see that different applied capillary pressures in step 2 will result in different initial oil saturations on the drainage curve and when we go to step 3 we will achieve different corresponding remaining saturations. Note that the profile between the initial saturation and the remaining saturation is known as the scanning curve which

represents capillary pressure hysteresis. The final trapping curve would look similar to the example displayed in Figure 1.26 corresponding to the points from Figure 1.25.

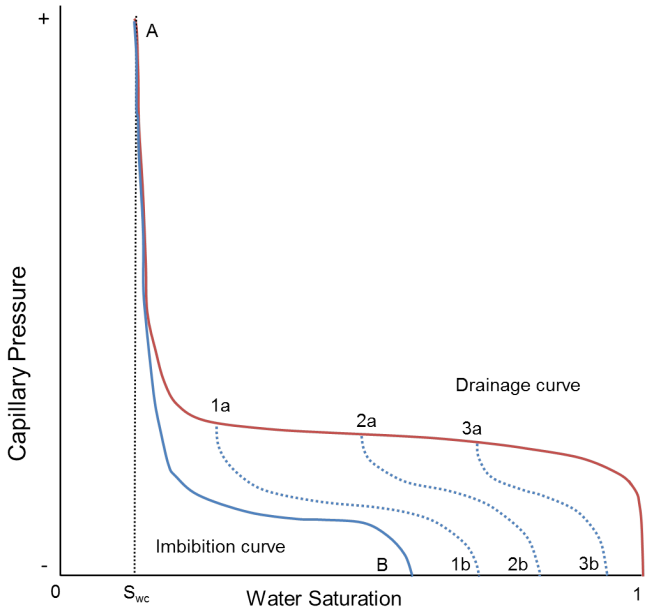

Figure 1.25. A schematic scanning curve where the drainage capillary pressure ends at different stages and yields at different corresponding S_w during waterflooding, including different residual saturations at the end of the experiment.

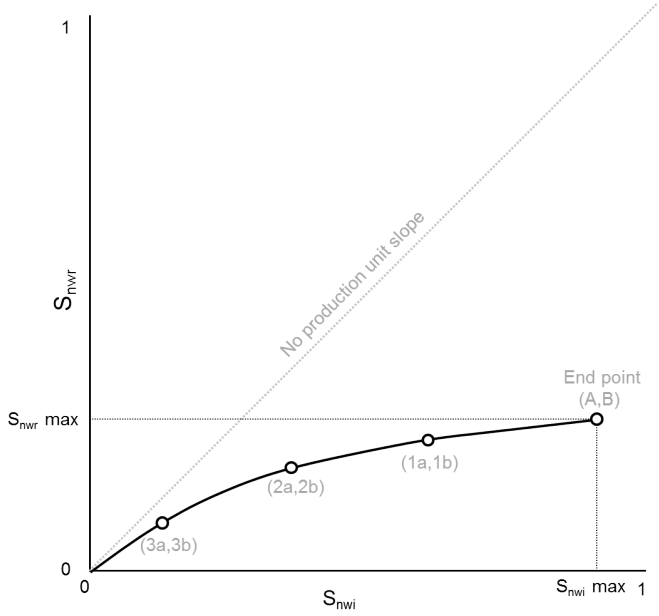

Figure 1.26. A schematic capillary trapping curve of water-wet porous media where the S_{nwr} monotonically increases with an increase in S_{nwi}.

1.6. Previous Studies of Capillary Trapping in Water-Wet Media

Several studies have discussed the trapping curve in water-wet media. Figure 1.27 shows a selected literature survey of trapping curves of water-wet rocks while Table 1.2 shows further details of these studies. In these cases the experiments were performed on clean rock samples that were assumed to be water-wet: *Fernø et al.* 2010 and *Graue et al.* 1999 showed that this was the case by measuring an Amott water index of 1, while *Tanino and Blunt* 2013 demonstrated strong spontaneous imbibition for the rocks they studied. The main point is that all the studies show a monotonic increase between the non-wetting phase residual saturation as a function of initial non-wetting phase saturation. In other words, the studies show, the more saturation in will yield in more saturation trapped. However, the data points do not collapse in one curve and vary, due to different rock types, different fluid properties, and different experimental conditions.

In water-wet rocks, it is safe to say that the final residual saturation is reached in the experiments after only a few pore volumes of water injection since trapping is principally caused by snap-off with little oil production after water breakthrough. In addition, the increasing trend between initial and residual saturations can be explained by simply saying that snap-off will render more non-wetting phase immobile if there is more non-wetting phase in the system.

In addition, we do not observe a different trend between the homogeneous sandstone and the heterogeneous carbonate rocks. This indicates that the monotonic increasing trend is a property of the water-wet rocks regardless of the complexity of the rock's pore structure. As more non-wetting phase is introduced into the rock, more is trapped. Although, as we show in the next chapter, carbonates can show a very wide range of pore size, this does not change the trend in trapping compared to sandstones. The generic similarity of trapping for carbonates and sandstones for CO_2 systems specifically has also been observed in a recent literature review by *Krevor et al.* 2015.

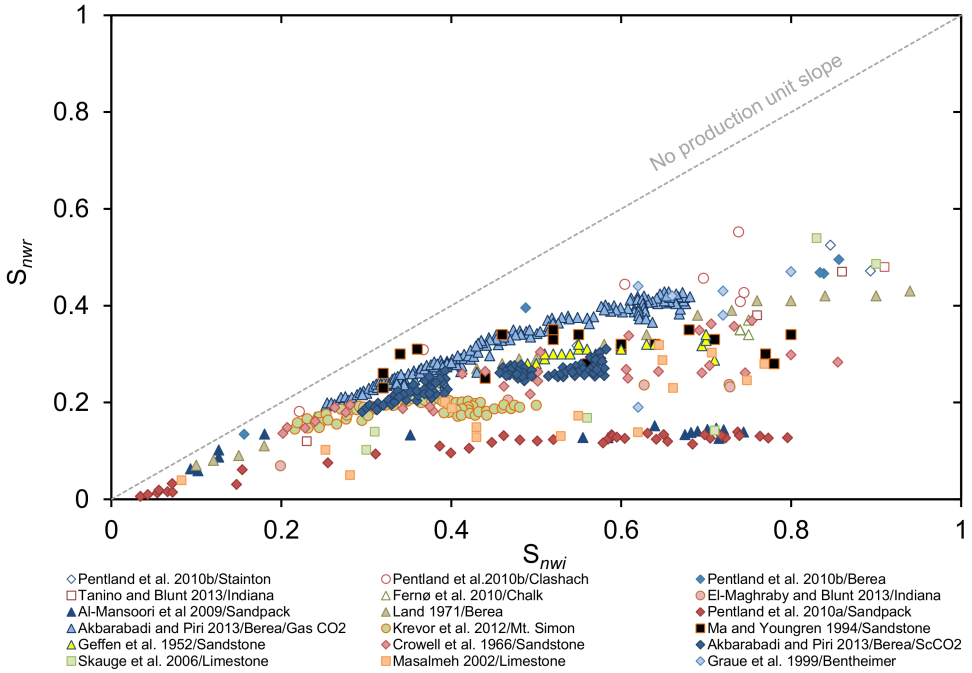

Figure 1.27. Literature database of the capillary trapping curve for water-wet porous media.

Table 1.2. Futher information regarding the studies plotted in Figure 1.27 for water-wet rocks.

Reference	Rock/Type	Fluids
Pentland et al. 2010	Stainton/Sandstone	n-decane/brine
Pentland et al. 2010	Clashach/Sandstone	n-decane/brine
Pentland et al. 2010	Berea/Sandstone	n-decane/brine
Tanino and Blunt 2013	Indiana/Limestone	n-decane/brine
Fernø et al. 2010	Chalk/Limestone	n-decane/brine
El-Maghraby and Blunt 2013	Indiana/Limestone	CO_2/brine
Al Mansoori et al. 2009	Sandpack	air/brine
Land 1971	Berea/Sandstone	N_2/oil
Pentland et al. 2010	Sandpack	octane/brine
Akbarabadi and Piri 2013	Berea/Sandstone	Gas CO_2/brine
Akbarabadi and Piri 2013	Berea/Sandstone	$ScCO_2$/brine
Krevor et al. 2011	Mt. Simon/Sandstone	$ScCO_2$/water
Ma and Youngren 1994	Sandstone	gas/water
Geffen et al. 1952	Sandstone	gas/water
Crowell et al. 1966	sandstone	gas/water
Skauge et al. 2006	Limestone	n-decane/brine
Masalmeh 2002	Limestone	(refined oil/n-decane)/brine
Graue et al. 1999	Bentheimer/Sandstone	crude oil/brine

1.7. Previous Studies of Capillary Trapping in Altered-Wettability Media

The literature for cores whose wettability has been altered is more limited compared to the water-wet survey. Figure 1.28 shows the trapping curve in altered-wettability porous media and Table 1.3 shows further details of these studies. In this figure, we do not see a distinct trend compared to water-wet rocks. This inconsistency in trend can be attributed to the difficulty of reproducing these experiments; since ageing these rocks to establish the wettability depends on the composition of the oil, the experimental conditions, and the rock type. Here we are mixing results from different–generally unknown–rock types and wettabilities.

In general though we see less trapping than in water-wet media. This is because, at the pore scale, the oil remains connected in layers for oil-wet and mixed-wet systems, Figure 1.18, and thus low residual saturations may be achieved if sufficient water is injected. For intermediate-wet rocks, the amount of trapping is controlled by the degree of snap-off: we expect less trapping but a monotonic trend with initial saturation. Furthermore, in many altered wettability samples there is significant, yet slow, oil production after breakthrough and the "residual" saturation reported may simply be the remaining value at the end of the experiment, rather than a true residual.

Another important feature observed by *Tanino and Blunt* 2013 is a non-monotonic trend of residual saturation with initial saturation. For water-wet media, where the degree of trapping is controlled by snap-off, the more the pore space is initially filled with oil, the more oil can be trapped. However, for oil-wet and mixed-wet media, with oil layers, the amount of trapping is controlled by when these layers collapse. As we showed in Figure 1.18, oil layers are more stable for higher initial oil saturation, which can result in less trapping than for a lower initial oil saturation where the layers are thinner and may collapse earlier in the displacement. We will return to this phenomenon later in the thesis.

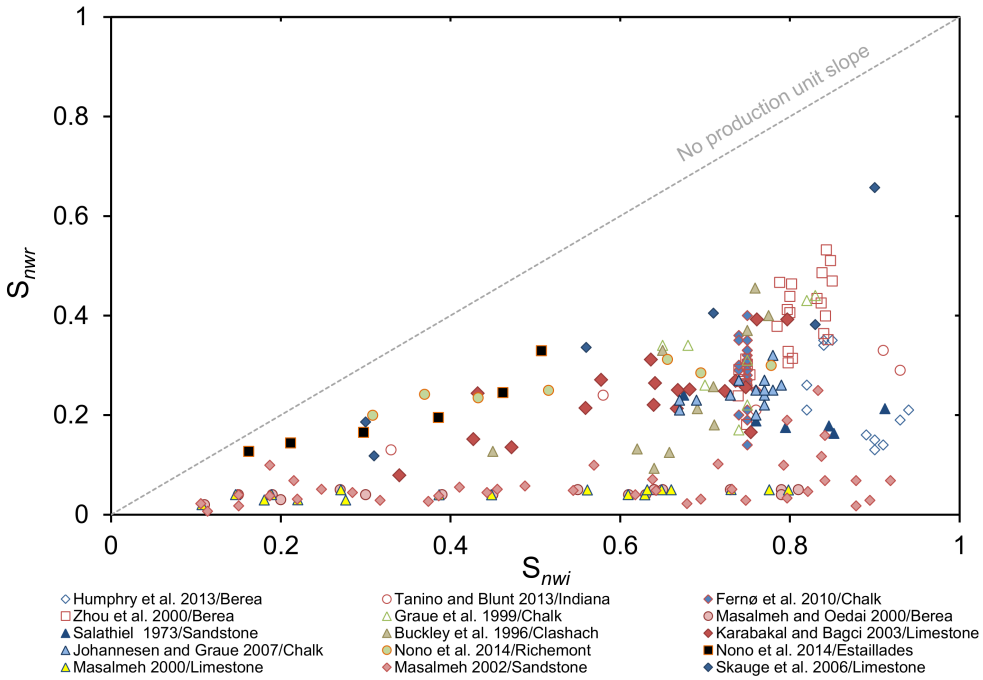

Figure 1.28. Literature database of the capillary trapping curve for altered-wettability porous media.

Table 1.3. Further information regarding the studies plotted in Figure 1.28 for altered-wettability rocks.

Reference	Rock/Type	Ageing Fluid
Humphry et al. 2013	Berea/Sandstone	Crude oil
Tanino and Blunt 2013	Indiana/Limestone	Organic acid
Fernø et al. 2010	Chalk/Limestone	Crude oil
Zhou et al. 2000	Berea/Sandstone	Crude oil
Graue et al. 1999	Chalk/Limestone	Crude oil
Masalmeh and Oedai 2000	Berea/Sandstone	Crude oil
Salathiel 1973	Sandstone	Crude oil
Buckley et al. 1996	Clashach/Sandstone	Crude oil
Karabakal and Bagci 2004	Limestone	Mineral oil
Johannesen and Graue 2007	Chalk/Limestone	Crude oil
Nono et al. 2014	Richemont/Limestone	Crude oil
Nono et al. 2014	Estaillades/Limestone	Crude oil
Masalmeh 2000	Limestone	Crude oil
Masalmeh 2002	Sandstone	Crude oil
Skauge et al. 2006	Limestone	Crude oil

1.8. Aims and Objectives

Understanding wettability and its influence on capillary trapping is a key factor in estimating storage and recovery efficiencies. Studies on CCS and EOR have different emphasis; for instance, in CCS we aim to drain the reservoir of its original fluid and replace it with CO_2 (primary drainage), while in EOR we try to maximise the gas/oil recovery by waterflooding. However, in capillary trapping experiments both drainage and imbibition (or waterflooding) need to be performed, and hence a better understanding of both is required. In this thesis, we will mainly focus on capillary trapping in altered wettability rocks and oil recovery as a function of the amount of water injected, since it has not been studied extensively, especially, in carbonates due to their inherit complexity.

In this thesis, we will also address the recovery of spontaneous imbibition and the capillary trapping mechanism in water-wet systems with application to fractured carbonates.

Therefore, we will:

1. Develop an understanding of spontaneous imbibition of uniformly water-wet media experimentally and compare it with the newly derived analytical solution for capillary dominated flow. This is important to understand recovery in fractured reservoirs.

2. Discuss how to use spontaneous imbibition experiments, in combination with other, more traditional measurements, to determine capillary pressure and relative permeability.

3. Develop an understanding of the trapping curve based on different wettability states by using (a) an organic acid and (b) a crude oil, as wettability alteration agents and performing them in different experimental conditions.

4. Measure the amount of recovery as a function of the amount of water injected.

5. Interpret the results in terms of pore-scale displacement processes and to provide guidelines for experimental measurements in complex carbonates.

1.9. Thesis Outline

This thesis comprises of six chapters and appendices:
Chapter 1 has given an introduction of the topic with a brief literature review.
Chapter 2 consists of a detailed description of the rocks used in this thesis.
Chapter 3 presents experimental and analytical solution of spontaneous water imbibition in water-wet media.
Chapter 4 presents waterflooding experiments under water-wet and altered-wettability systems by using an organic acid at ambient conditions and a crude oil at elevated temperatures to alter the wettability of the rocks.
Chapter 5 comprises a final conclusion of the thesis and recommendations for future work.
The Appendices contain detailed measurements and procedures of all the steps that were not explained in detail in the previous chapters.

2. Rock Properties

2.1. Introduction

In this chapter, we discuss in detail the three carbonate rocks we use in this thesis. We characterise the rocks based on their mineral composition, porosity, and permeability. In addition, we discuss the mercury injection capillary pressure and nuclear magnetic resonance data. We also provide a pore-scale analysis based on micro-CT images of the samples.

2.2. Rock Characterisation

We use three different types of carbonate rock in our study. I measured the porosity and permeability of these rocks using different methods. Full details of the techniques used and the results are provided in Appendix A.1 for porosity and Appendix A.3 for permeability. I also measured interfacial tensions, contact angles, viscosities and densities of the fluids used in this thesis–again full details are provided in the Appendices. Table 2.1 shows the porosity and permeability range for each rock based on all measurements on many samples of each rock type conducted in this thesis.

One reason for the choice of the rocks described below is that they have been used as benchmarks for other experiments as part of the Qatar Carbonates and Carbon Storage Research Centre (QCCSRC), Figure 2.1; as a result, we can make use of images acquired at different resolution to interpret the nature of the pore space, as well as independent measurements of mercury injection primary drainage capillary pressure (MICP) and nuclear magnetic resonance (NMR).

Estaillades is a bioclastic limestone, which is almost entirely composed of calcite ($CaCO_3$) which forms 99% of the sample; the remaining 1% accounts for traces of dolomite and silica. This rock comes from the Estaillade Formation, found in the Oppède quarry, south of France [*Watson*, 1911]. Estaillades limestone has a pale white colour. The grain size is medium to coarse. Estaillades limestone formation was deposited during the Late Cretaceous, specifically, between 100-72 million years ago, corresponding to the Cenomanian and Campanian ages. This type of limestone is thought to have been deposited in near-surface terrestrial settings where significant carbonate accumulations have been reported [*Wright et al.*, 1995].

Ketton is an oolitic limestone which is composed of 99.1% calcite; the remaining 0.9% accounts for quartz. This rock comes from the Lincolnshire Formation, located in Rutland, east Midlands, UK [*Andrew et al.*, 2014, *Muir-Wood and F.G.S.*, 1952]. The Ketton limestone has a pale brown colour. The grain size is medium to coarse and it is well sorted. Ketton limestone formation was deposited during the Mid Jurassic between 176-167 million years ago, corresponding to the Toarcian and Bajocian ages. The Lincolnshire Limestone Formation is the major carbonate formation of the Middle Jurassic in the east Midlands. This formation exhibits a very complex internal stratigraphy and a wide range of carbonate textures. These are interpreted as represent a landward migration of an offshore barrier bar complex (the upper Lincolnshire Limestone) across a protected lagoon and back barrier (the middle and lower Lincolnshire Limestone) [*Ashton*, 1980].

Portland is a skeletal-peloidal limestone composed of 96.6% calcite and 3.4% quartz. This rock comes from the Portland quarry, UK. The Portland limestone has a pale grey colour. The grain size is fine to very fine and the grains are well sorted. Portland limestone formation was deposited during the Late Jurassic between 152-145 million years ago, corresponding to the Kimmeridgian and Tithonian ages [*Brenchley and Rawson*, 2006].

The Brunauer-Emmett-Teller (BET) surface areas measured at Weatherford Laboratories at East Grinstead, UK are 0.602 m^2/g, 2.185 m^2/g, and 1.133 m^2/g for Estaillades, Ketton, and Portland respectively: details of this method are provided elsewhere, [*Brunauer et al.*, 1938]. Ketton has the highest surface area since it has the largest amount of small micro-porosity within the larger grains, while Estaillades has the lowest surface area since it has the least micro-porosity. We will discuss this further in the following sections.

Table 2.1. Porosity and permeability range of each rock used in this thesis.

Rock	ϕ [%]	k [$\times 10^{-15} m^2$]
Estaillades	26-28	120-390
Ketton	20-23	1007-3550
Portland	16-22	1.8-35

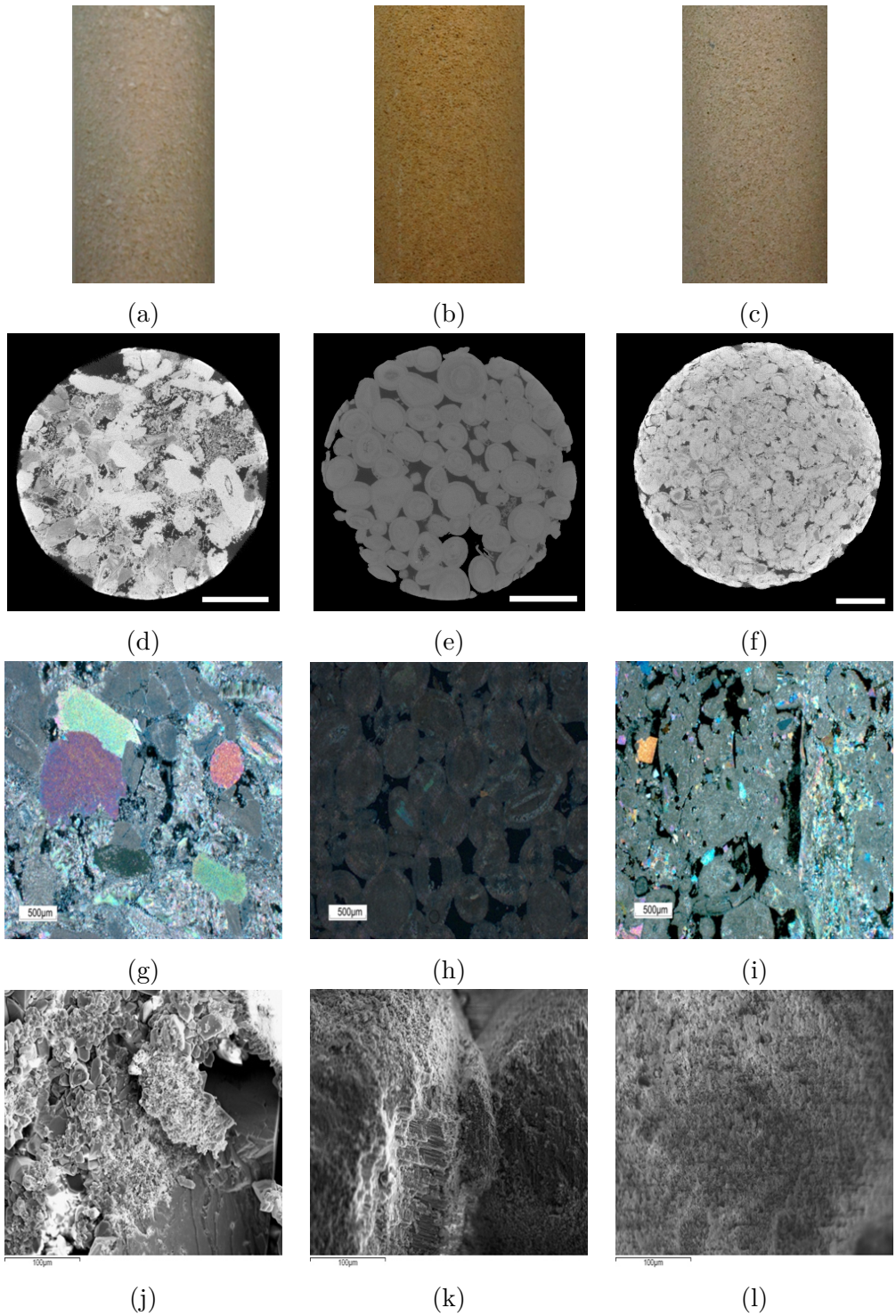

Figure 2.1. Images of 38 mm × 76 mm cores of (a) Estaillades, (b) Ketton, and (c) Portland cores. Slices (two-dimensional sections) of three-dimensional X-ray microtomography scans of (d) Estaillades, (e) Ketton, and (f) Portland. The white bar represents 1 mm. Thin section images of (g) Estaillades, (h) Ketton, and (i) Portland of an angle of 180° at 2× magnification. SEM images of (j) Estaillades, (k) Ketton, and (l) Portland at 1000× magnification. The X-ray microtomography scans, thin section images, and SEM images are obtained from the QCCSRC digital library.

2.3. Mercury Injection Capillary Pressure

Figure 2.2 shows the measured MICP of the three rocks (Autopore IV 9520, Weatherford Laboratories, East Grinstead, UK). We can see that Portland has the highest capillary entry pressure (minimum value of $P/2\sigma\cos\theta$) of approximately 0.18 μm^{-1} and equivalent r_p, Equation 1.6, of 5.6 μm, while Estaillades has a lower capillary entry pressure of approximately 0.029 μm^{-1} and equivalent r_p of 35 μm. Ketton has the lowest capillary entry pressure of approximately 0.017 μm^{-1} and equivalent r_p of 59 μm.

Figure 2.3 shows the pore size distribution: we can see that both Estaillades and Ketton have distinct bi-modal distributions with at least 50% of pore sizes greater than 0.5 μm. Portland has a uni-modal distribution with the majority of the pore sizes less than 0.5 μm.

If we consider r_p=0.5 μm as the cut off value between micro and macro-porosity, then 35%, 44%, and 81% of Estaillades, Ketton, and Portland respectively is micro-porosity. Overall, Figure 2.3 shows that these limestone samples have a wide range of estimated throat size: a range that is typically much larger than in sandstones, as discussed in the previous chapter. Estaillades and Ketton show clear bi-model behaviour associated with inter and intra-granular porosity, while Portland displays a very wide but uni-modal distribution of throat size.

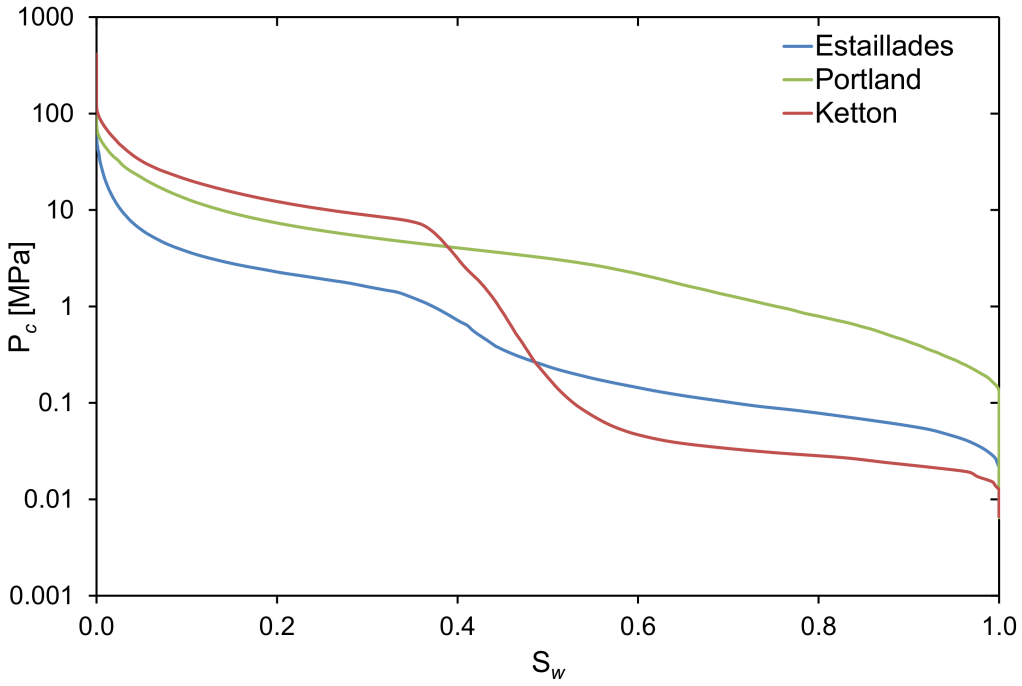

Figure 2.2. Measured capillary pressure (mercury/air) as a function of equivalent water saturation.

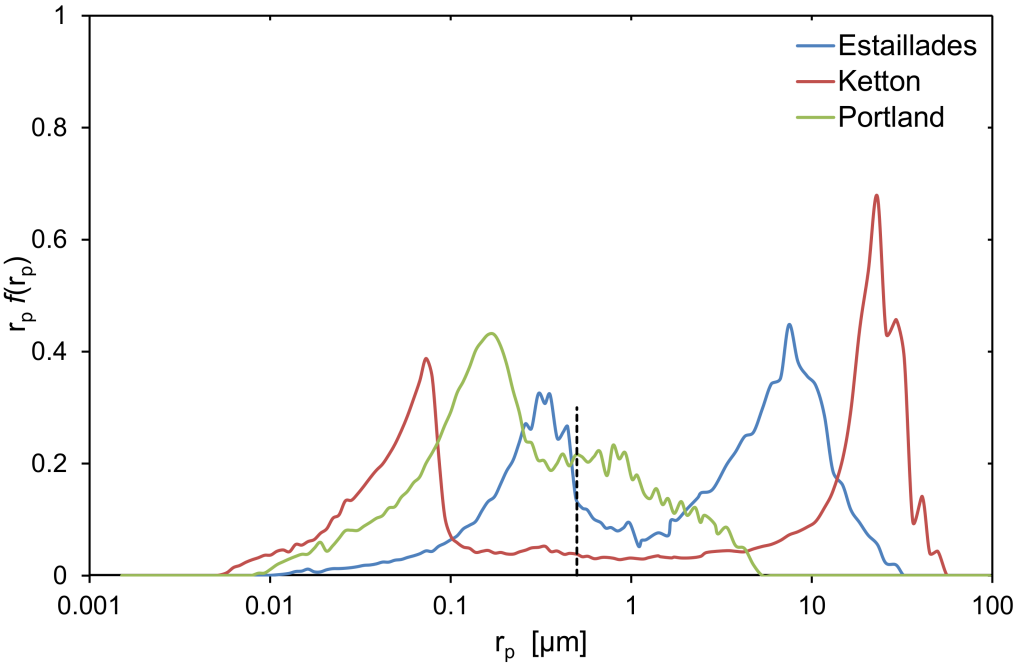

Figure 2.3. The pore size distribution against pore throat radius for the three carbonates. The dashed line depicts r_p= 0.5 μm.

2.4. Nuclear Magnetic Resonance

We also characterise the rocks using the transverse relaxation time (T_2) from NMR in brine saturated cores (MHz Maran Utra NMR system, Weatherford Laboratories, East Grinstead, UK).

The T_2 relaxation time is obtained through controlled radio frequency perturbations of a steady magnetic field that is applied to the brine-saturated samples. The perturbations lead to decay (relaxation) in the transverse magnetization; this relaxation is assumed to be proportional to the volume/surface ratio of a single pore/throat [*Straley et al.*, 1997, *Westphal et al.*, 2005]. Therefore, we can achieve the pore size from the following equation:

$$r = V/S = \rho_2 T_2 \tag{2.1}$$

where V/S is volume/surface ration [μm], ρ_2 is a scaling constant specific to the rock [μm/ms], and T_2 is transverse relaxation time [ms]. This is an approximate relation, assuming spherical pores. NMR detects the size of large pore spaces, while MICP detects the restrictions, or throats.

Figure 2.4 shows the T_2 weighted probability distribution function, $T_2 f(T_2)$ against T_2. Ketton shows a distinct bi-modal distribution, while both Estaillades and Portland show a uni-modal distribution. However, Estaillades has a small peak at T_2 less than 10 ms, which is suggestive of a bi-modal distribution.

To find the pore size from NMR and compare it with the MICP, we need first to find ρ_2. We use a simple approach by plotting pore size distribution of both NMR and MICP using a normalised frequency. We start by having an initial guess of ρ_2 and varying it until the peaks of the macro-pores coincide: see Figure 2.5 for instance. We do the same for the other two rocks which will show later.

Figure 2.6 shows the pore size distribution obtained from NMR. The values of ρ_2 used are 0.02 μm/ms, 0.115 μm/ms, and 0.0044 μm/ms for Estaillades, Ketton, and Portland respectively. If we assume again that r_p= 0.5 μm is the cut-off micro-porosity value then the equivalent T_2 cut off will be 50 ms, 9 ms, and 230 ms for Estaillades, Ketton, and Portland respectively.

From the $T_{2\ cut-off}$, we can measure the macro-and micro-porosity of the rocks. To calculate the percentage of macro-porosity to total porosity, and micro-porosity to total porosity we compute:

$$\frac{\phi_{macro}}{\phi} = \int_{T_{2\ cut-off}}^{\infty} f(T_2) dT_2 \tag{2.2}$$

$$\frac{\phi_{micro}}{\phi} = \int_{0}^{T_{2\ cut-off}} f(T_2) dT_2 \tag{2.3}$$

The micro-porosity fraction based on the NMR data are 8%, 15%, and 77% for Estaillades, Ketton, and Portland respectively. The trend is consistent with the MICP finding; however, the percentage of micro-porosity is less from NMR as the shape of the distribution does not match the MICP distribution. NMR is less able to detect micro-porosity as this causes very rapid relaxation which may not be recorded. The discrepancy between the distributions is not surprising as neither directly measures the size distribution in the rock: MICP emphasises the throats, while NMR records largely the distribution of pore size.

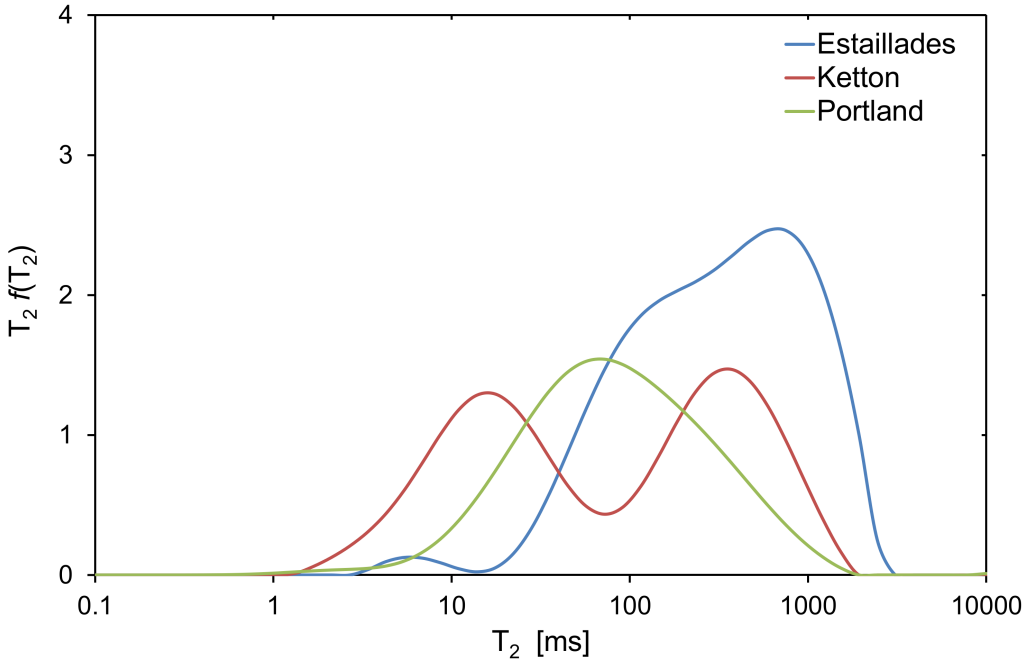

Figure 2.4. $T_2 f(T_2)$ against T_2 from NMR for all the three rocks used in this study.

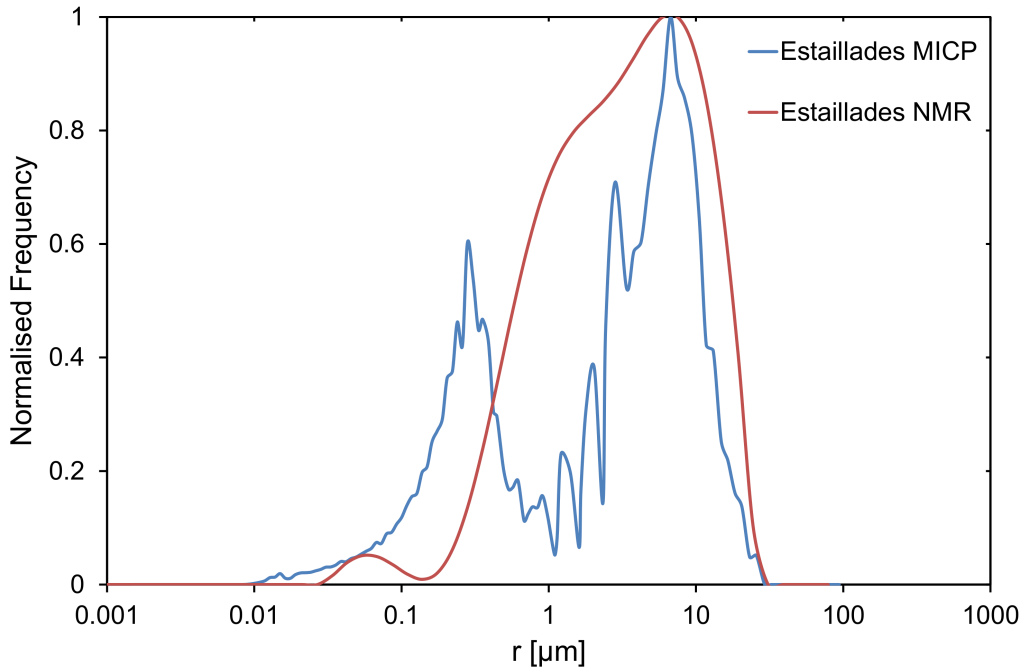

Figure 2.5. Example showing how to convert the T_2 to pore size by adjusting the ρ_2 parameter to fit the peak of macro pores in the MICP distribution.

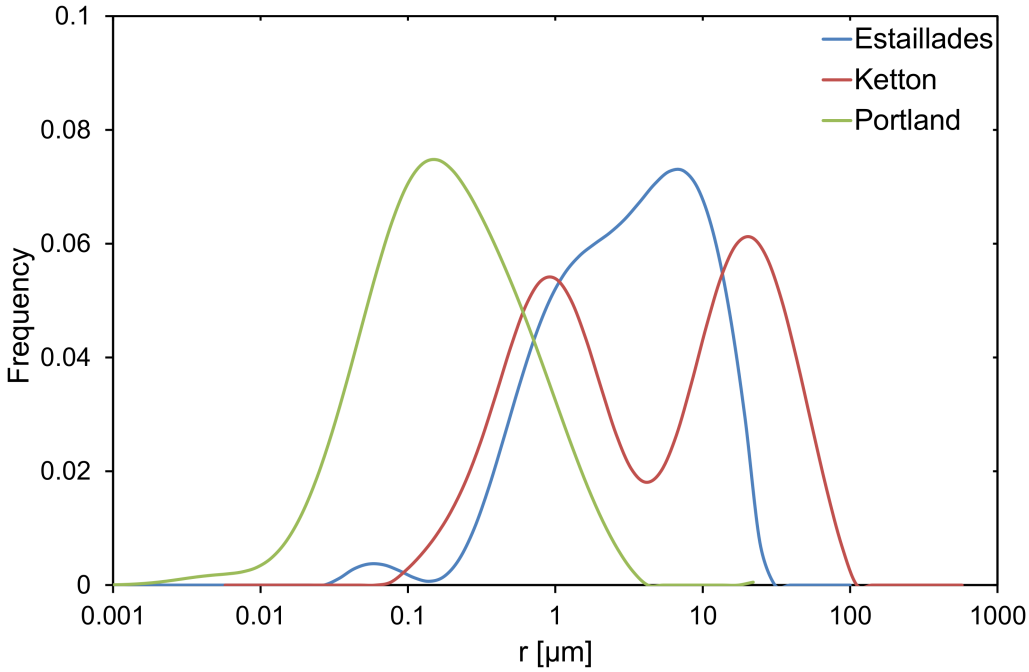

Figure 2.6. Pore size distribution obtained from converting the T_2 to pore size and plotting it against frequency.

2.5. Pore-Scale Modelling

Pore-scale modelling (PSM) is the prediction of flow and transport properties using three-dimensional images of the pore space [*Blunt et al.*, 2013]. We use pore-scale modelling to predict permeability and pore size distribution of the rocks and compare them with the experimental results. To predict the flow properties, we need to go through several stages starting from imaging the rocks by the micro-CT scanner to image processing to network extraction and finally to predict the single-phase properties by simulating fluid flow.

2.5.1. Micro-CT Imaging

Tomographic datasets were obtained and analysed using the micro-CT facility built at Australian National University (ANU) and housed at the newly established digital core laboratory at Maersk Oil Research and Technology Centre, Qatar. The scans were conducted on a 5 mm plugs of each rock with an image resolution of 2.9 μm. The plugs were mounted in an anodized aluminium sample holder, of inner diameter of 5 mm. The holder was scanned through the aluminium-filtered (3 mm) Bremsstrahlung from the polychromatic X-ray source, operated at 80 kV and 110 mA settings. Radiographs (2048×2048 pixel^2) were captured by a flat panel detector. The scans were performed in which 2520 projections were acquired over the helical pitch, at a source-camera distance of 354 mm. Each of these tomograms took about 18 hours to acquire.

2.5.2. Image Processing

Each image was cropped to a cubic base case of 1000^3 voxels for all the three rocks using ImageJ software. These are subsequently segmented to create discrete domains required to compute single phase properties of the rock. The rocks were segmented according to the variation of CT contrast between rock and pore space using multi-thresholding based on Otsu's algorithm [*Otsu*, 1975]. The images were segmented using a three domain algorithm followed by a two domain Otsu classification using Gimp software, Figure 2.7. Due to the high quality of the images applying mean filters and performing ring removal, which may alter the predicted morphology of the rock, was unnecessary. Figure 2.8 shows three dimensional images of the segmented images of each rock.

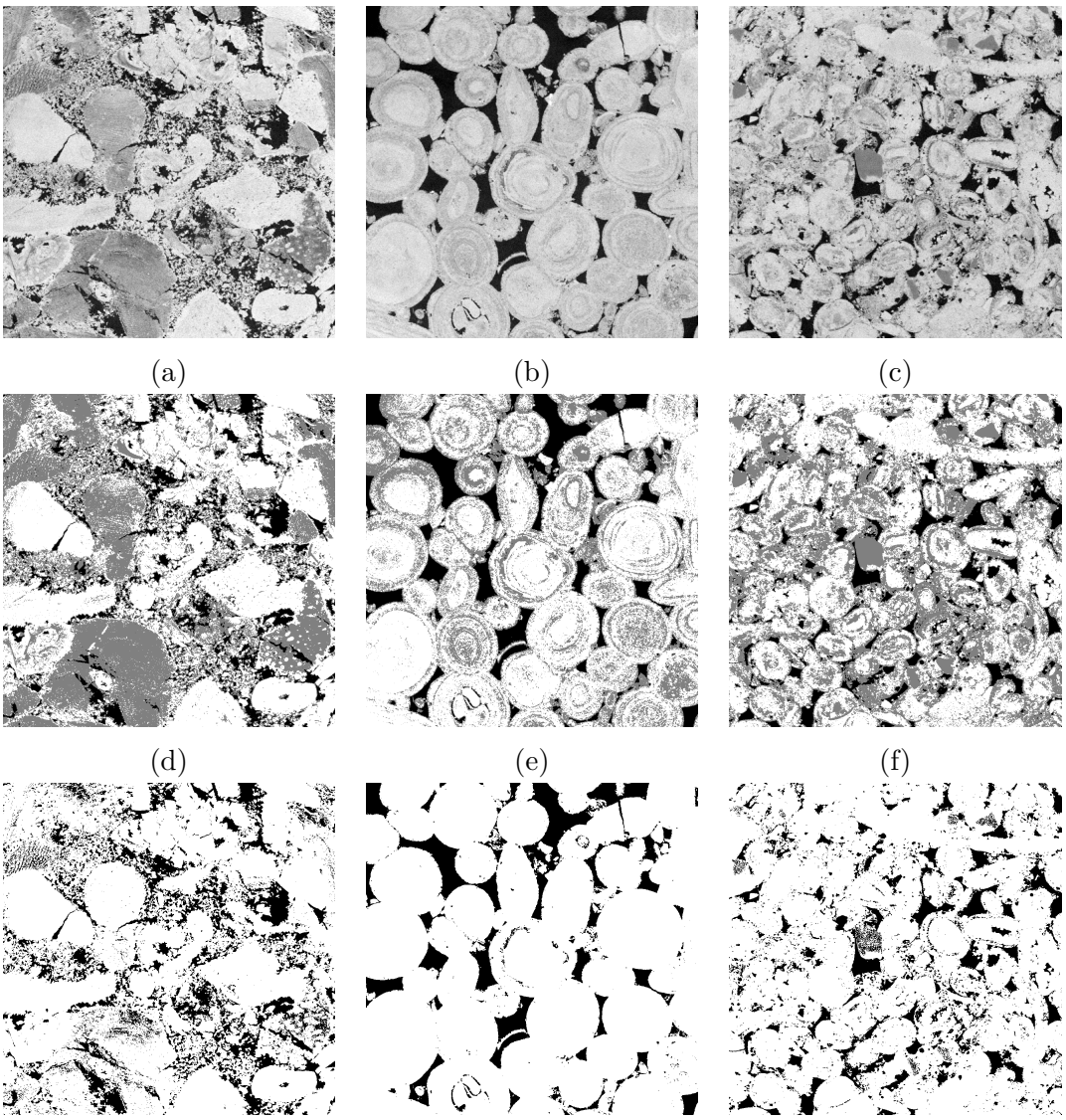

Figure 2.7. Grey scale micro-CT image cross-section for (a) Estaillades, (b) Ketton, and (c) Portland. Three phase multi-thresholding for (d) Estaillades, (e) Ketton, and (f) Portland. Two phase images segmentation for (g) Estaillades, (h) Ketton, and (i) Portland. All these images are 1000×1000 pixel^2 which is equivalent to an area of 8.41 mm^2.

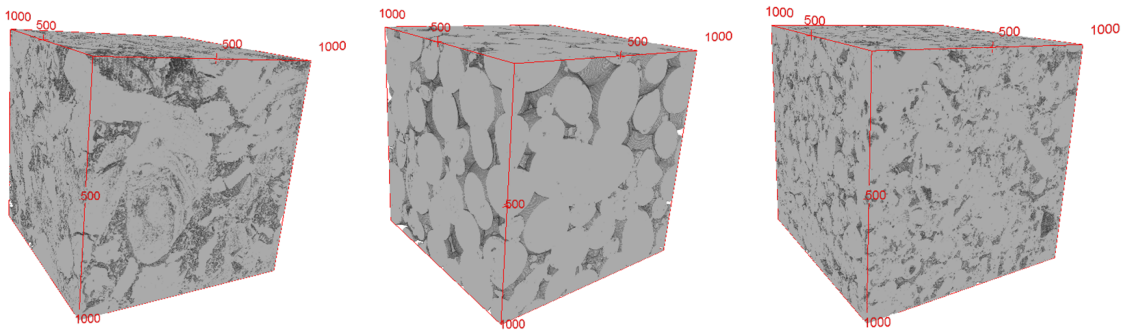

(a) (b) (c)

Figure 2.8. Three-dimensional micro-CT images for (a) Estaillades, (b) Ketton, and (c) Portland representing 1000^3 voxel which is equivalent to a volume of 24.4 mm^3.

2.5.3. Network Properties

We use a maximal ball algorithm to extract topologically representative networks from the images. The method finds the largest spheres that fit in the pore space are pores, while chains of smaller spheres connecting them represent throats. Details of the method are provided elsewhere, *Dong and Blunt* [2009].

Figure 2.9 shows the extracted topological networks from the 3D images. Table 2.2 shows the network properties of the rocks. We can see that Estaillades has the highest number of pores and throats while Ketton has the lowest. From the 2D images we can see that Estaillades is characterised with both large and small pores while Ketton has only few big pores that can be captured by micro-CT imaging. Ketton has the largest average pore and throat radii which might be expected due to its high permeability, while Estaillades has the highest average coordination number. This can be explained by the large number of small throats that contribute to the connectivity of the rock.

The computed pore and throat radii distribution from extracted networks are shown in Figures 2.10 and 2.11 respectively. Note that we do not capture micro-porosity in these images and hence cannot accommodate elements smaller than a few μm in size. This explains the uni-modal distribution of these figures, unlike the MICP and NMR distributions presented in Figures 2.3 and 2.6. We can also see that the distributions peek close to their average values which explains the similarity between the two figures. However, the distributions for all three rocks are similar and show a peak close to the voxel resolution of the image with the possible exception of Ketton. This indicates that the images do not adequately resolve the pore structure and that we cannot reply on network modelling for quantitative predictions of flow properties in these cases.

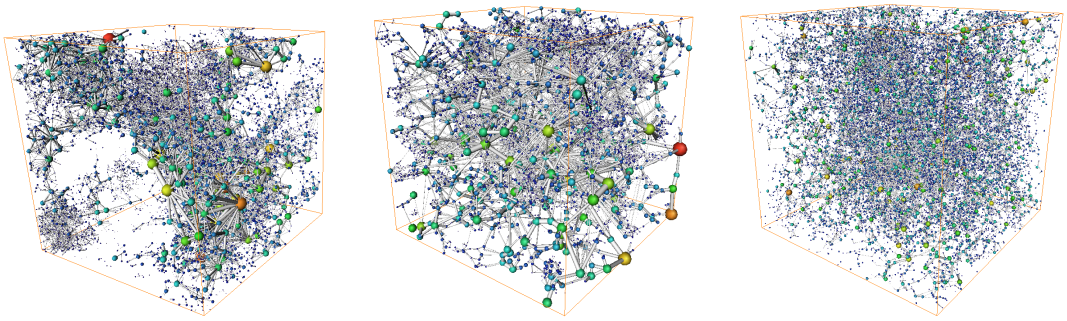

(a) (b) (c)

Figure 2.9. Three-dimensional pore and throat images (generated from the network extraction code [*Dong and Blunt*, 2009] for (a) Estaillades, (b) Ketton, and (c) Portland.

Table 2.2. Network properties of the three rocks.

Rock	Estaillades	Ketton	Portland
Number of Pores	157366	19827	140038
Number of Throats	393524	36362	260670
Average Pore Radius [μm]	5.2	8.0	5.1
Average Throat Radius [μm]	2.4	5.3	2.2
Coordination Number	5.0	3.7	3.7

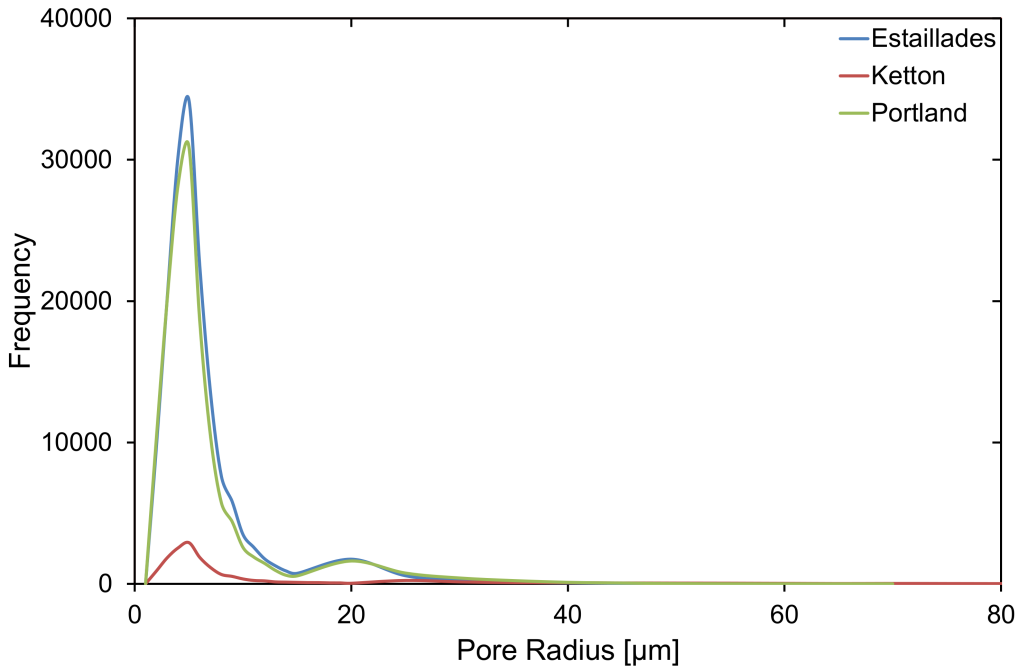

Figure 2.10. Pore radius distribution from the extracted networks for the three different rocks.

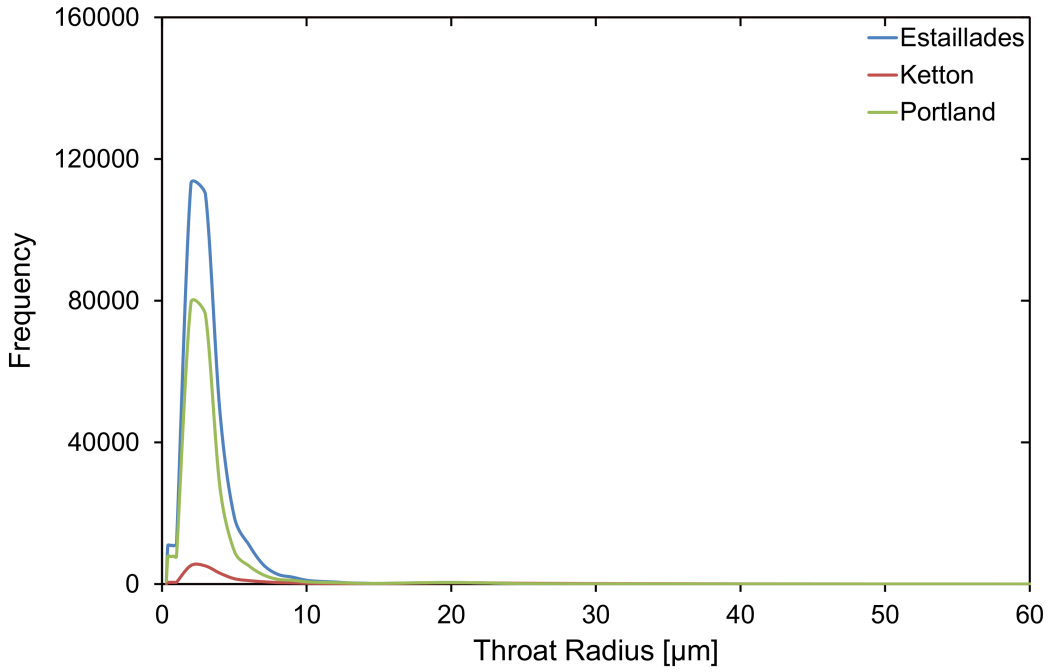

Figure 2.11. Throat radius distribution from the extracted networks for the three different rocks.

2.5.4. Single-Phase Properties

We calculate the porosity of the image by dividing the pore volume in the segmented image to the total volume. The micro-CT images capture at least 54% of the porosity measured directly on several rock samples using different methods. See Appendix A.1 for details of the measurements and Tables 2.1 and 2.3 for a summary of the results.

We also measure permeability for 20 samples of Estaillades, 15 samples of Ketton and 19 samples of Portland limestone (see Appendix A.3). We observe a wide range of values, reported in Table 2.3. However, for the measured MICP and NMR data, as well as for the images, we only consider a single sample. While visual inspection of the rock indicates that the generic pore structures should be similar for different samples of the same rock type, it is evident that the details are different. In the remainder of the thesis we will perform experiments on several samples of each rock type to quantify the range of behaviour, both within a rock type and between rock types.

For the permeability prediction, we use the extracted networks to calculate the single-phase permeability. The computation essentially treats the porous medium as a random resistor network with semi-analytically computed permeabilities for each element *Valvatne and Blunt* [2004]. The predicted permeabilities show reasonable agreement with the experimental values measured on larger core samples although only for Ketton, with

flow clearly defined through the large pores, is our computed value in the measured range. We underestimate the permeability of Estaillades and overestimate it for Portland, despite the wide range of experimental values, Table 2.3. This indicates that with the resolution of the micro-CT scan we are not able to capture representative networks of these structures.

Table 2.3. Summary of the predicted single phase properties, where ϕ_{Image}/ϕ is the ratio of the image porosity to the range of the experimental values measured on the large cores.

Rock	ϕ_{Image} [%]	ϕ_{Image}/ϕ [%]	Predicted k [m^2]	Measured k [m^2]
Estaillades	15.1	54-58	9.49×10^{-14}	$1.2\text{-}3.9\times10^{-13}$
Ketton	14.9	62-71	2.19×10^{-12}	$1.0\text{-}3.6\times10^{-12}$
Portland	13.2	57-70	4.66×10^{-14}	$1.8\text{-}35\times10^{-15}$

2.6. Comparison of Pore Throat Size Distributions

We compare the pore size distribution derived from the three different methods used in this chapter (MICP, NMR, and PSM) against normalised frequency for standard comparison. Note that we use throat size from PSM in this comparison as MICP detects throat size only and the NMR distribution is based on matching the MICP curve.

For Estaillades, Figure 2.12a, we can see a good match between all the three methods in the macro-pores. However, NMR and PSM do not detect the micro-porosity.

For Ketton, Figure 2.12b, PSM underestimates the macro-pores and does not account for the micro-pores compared to MICP. NMR has a good match with MICP for the macro-pores and covers a narrower range in the micro-pores. MICP, on the other hand, has the highest resolution, covering wider range of throat sizes.

For Portland, Figure 2.12c, PSM over-predicts the pore size in the macro-pores and does not detect the micro-pores, while NMR and MICP coincide with a good agreement with one another.

The conclusion of this section is that only MICP analysis gives a good indication of the full range of the throat size distribution in micro-porous rocks. NMR often neglects a large fraction of the micro-porosity, while PSM simply ignores any pores smaller than the image resolution.

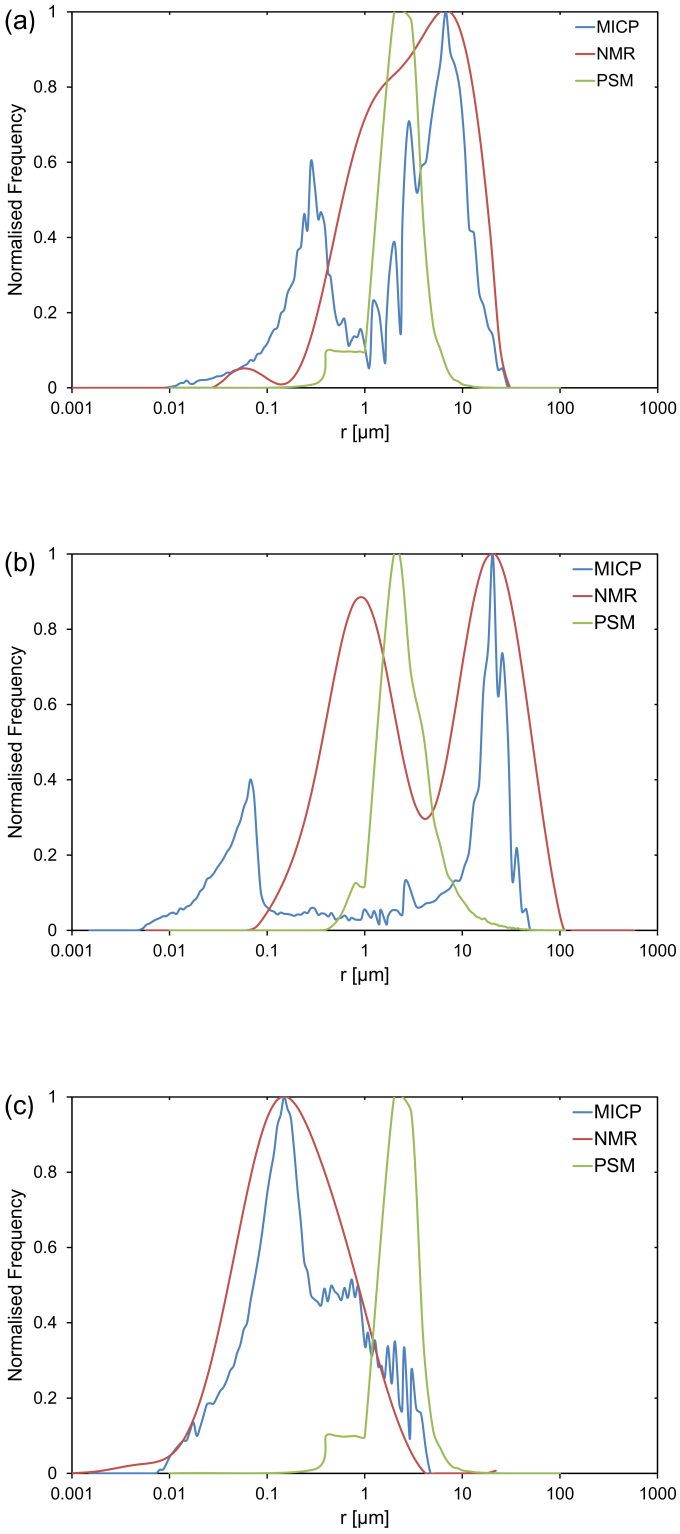

Figure 2.12. Comparison in pore size distribution between MICP, NMR, and PSM for (a) Estaillades, (b) Ketton, and (c) Portland.

2.7. Conclusions

The MICP data and measured T_2 distributions all demonstrate that the rocks have significant micro-porosity (pores smaller than 0.5 μm). In Ketton we have large ooliths that themselves are porous: around half of the porosity is composed of large intra-granular pores, while the remainder is from the inter-granular pores.

Estaillades also has a bi-modal pore size distribution but with a more distributed range of sizes, while Portland has no clear distribution between micro and macro-porosity, showing pores ranging continually in sizes from 0.01-10 μm.

Since we do not capture micro-porosity using our micro-CT images, a more quantitative analysis with PSM has little validity as we ignore a significant fraction of the pore space; the proper incorporation of these effects is the subject of future work. Hence, we will not use PSM to predict multi-phase properties–such as capillary pressure and relative permeability which are affected by micro-porosity (as evident from the MICP results).

3. Spontaneous Imbibition

3.1. Introduction

In this chapter, we perform co-current spontaneous imbibition experiments using a highly sensitive balance to measure the mass imbibed as a function of time for the three carbonate rocks. We use cores measuring 37 mm in diameter and three lengths of approximately 76 mm, 204 mm, and 290 mm. We evaluate the recovery and the rate of imbibition and we validate the derivation of the dimensionless time by *Schmid and Geiger* 2012. In addition, we perform the same experiment again; however, we use a medical CT for in-situ monitoring of the saturation movement inside the rock samples. In this experiment, we use one core of each rock type, 38 mm in diameter and 78 mm in length. We combine the two different experiments to validate the newly derived analytical solution for spontaneous imbibition, SI, by *Schmid et al.* 2011.

3.2. Analytical Solution

Schmid et al. 2011 derived an analytical solution for SI, where displacement is controlled entirely by capillary forces. We present the full derivation from the conservation equation to the exact solution, using my own approach and nomenclature. I have also developed my own way to solve the equations, described below.

The analytical solution makes the following assumptions:

1. Incompressible fluids.

2. That the traditional multi-phase Darcy law is applicable for this process.

3. Gravitational and imposed viscous forces are ignored.

4. We assume that at the inlet the capillary pressure is zero.

5. We will assume that the solutions are a function of the parameter $\omega = x/\sqrt{t}$; this is only valid at early time, before the imbibing water front has reached the far boundaries of the sample.

3.2.1. Equation Derivation

We start from the wetting phase conservation equation in one dimension for incompressible fluids:

$$\phi \frac{\partial S_w}{\partial t} + \frac{\partial q_w}{\partial x} = 0 \tag{3.1}$$

From the multiphase Darcy's law, the wetting phase Darcy velocity:

$$q_w = -\frac{k k_{rw}}{\mu_w} \left(\frac{\partial P_w}{\partial x} - \rho_w g_x \right) \tag{3.2}$$

and the same for the non-wetting phase Darcy velocity:

$$q_{nw} = -\frac{k k_{rnw}}{\mu_{nw}} \left(\frac{\partial P_{nw}}{\partial x} - \rho_{nw} g_x \right) \tag{3.3}$$

where $P_c = P_{nw} - P_w$ is the capillary pressure and k_r is the relative permeability. k_{rnw}, k_{rw}, and P_c are functions of S_w. We define mobilities of the wetting phase and the non-wetting as:

$$\lambda_w = \frac{k_{rw}}{\mu_w} \tag{3.4}$$

$$\lambda_{nw} = \frac{k_{rnw}}{\mu_{nw}} \tag{3.5}$$

$$\lambda_t = \lambda_w + \lambda_{nw} \tag{3.6}$$

since $q_t = q_w + q_{nw}$, is a constant in space for incompressible flow in one dimension, we can rewrite q_w as:

$$q_w = \frac{\lambda_w}{\lambda_t} \left\{ q_t + k \lambda_{nw} \left(\frac{\partial P_c}{\partial x} + (\rho_w - \rho_{nw}) g_x \right) \right\} \tag{3.7}$$

We eliminate the gravitational forces assuming that they are either small at the experimental (cm) scale or the displacement is horizontal. Then Equation 3.7 becomes:

$$q_w = f_w(S_w) q_t + \frac{k \lambda_w \lambda_{nw}}{\lambda_t} \frac{\partial P_c}{\partial x} \tag{3.8}$$

where f_w is the Buckley-Leverett fractional flow which is equal to λ_w / λ_t.

For counter-current imbibition, we set the total velocity (q_t) to zero which means that no fluid is injected and the movement of the wetting phase is matched by the volume of the non-wetting phase leaving the porous media ($q_{nw} = -q_w$), see Figure 1.15. Then Equation 3.7 becomes:

$$q_w = \frac{k \lambda_w \lambda_{nw}}{\lambda_t} \frac{\partial P_c}{\partial x} \tag{3.9}$$

We subsitiute Equation 3.8 for co-current imbibition in the wetting phase conservation equation, Equation 3.1, to become:

$$\phi \frac{\partial S_w}{\partial t} + \frac{\partial}{\partial x} \left(\frac{k \lambda_w \lambda_{nw}}{\lambda_t} \frac{\partial P_c}{\partial x} \right) + q_t \frac{\partial f_w}{\partial x} = 0 \tag{3.10}$$

We also substitute Equation 3.9 for counter-current imbibition in the wetting phase conservation equation, Equation 3.1, to become:

$$\phi\frac{dS_w}{dt}+\frac{\partial}{\partial x}\left(\frac{k\lambda_w\lambda_{nw}}{\lambda_t}\frac{\partial P_c}{\partial x}\right)=0 \tag{3.11}$$

We can re-write Equations 3.10 and 3.11 as non-linear diffusion equations.
For co-current flow:

$$\phi\frac{\partial S_w}{\partial t}=-q_t f'_w(s_w)\frac{\partial s_w}{\partial x}+\frac{\partial}{\partial x}\left(D(S_w)\frac{\partial S_w}{\partial x}\right) \tag{3.12}$$

and for counter-current flow:

$$\phi\frac{\partial S_w}{\partial t}=\frac{\partial}{\partial x}\left(D(S_w)\frac{\partial S_w}{\partial x}\right) \tag{3.13}$$

where $D(S_w)$ is the non-linear diffusion coefficient:

$$D(S_w)=-\frac{k\lambda_w\lambda_{nw}}{\lambda_t}\frac{\partial P_c}{\partial S_w} \tag{3.14}$$

In the traditional Buckley-Leverett analysis (ignoring capillary forces) we find that the solution is a function of $v{=}x/t$ only, where the dimensionless wavespeed is given by the saturation derivative of the fractional flow ($v_D{=}df_w/dS_w$ where $v{=}q_t/\phi\ v_D$) [*Buckley and Leverett*, 1942, *Dake*, 1983], see Figure 3.1. The times (t_2 and t_3) are stretched versions of t_1 such that $x_1/t_1{=}x_2/t_2$.

We propose an analogy here, but for capillary-controlled flow, which is diffusive: the imbibing front moves a distance x that instead of scaling with t, as in the Buckley-Leverett case, scales as $\sqrt{t}$ [*Garg et al.*, 1996, *Handy*, 1960, *Babadagli and Ershaghi*, 1992, *Li and Horne*, 2001, *Olafuyi et al.*, 2007], see Figure 3.2. Hence, we will now attempt to find a solution that can be written as a function of:

$$\omega=\frac{x}{\sqrt{t}} \tag{3.15}$$

We will show that this assumption is valid for our experiments. However, some experiments show a deviation from $\sqrt{t}$ [*Mason et al.*, 2010, 2012, *Fernø et al.*, 2014]. *Mason et al.* 2012 reported that for n-decane and brine counter-current flow, the imbibition scales linearly with time when the flow and the associated resistance is not entirely related to one-dimensional flow in the core, as assumed here. The scaling we use is only valid under the assumptions mentioned at the beginning of the section, and specifically when the flow is entirely driven by capillary forces within the rock.

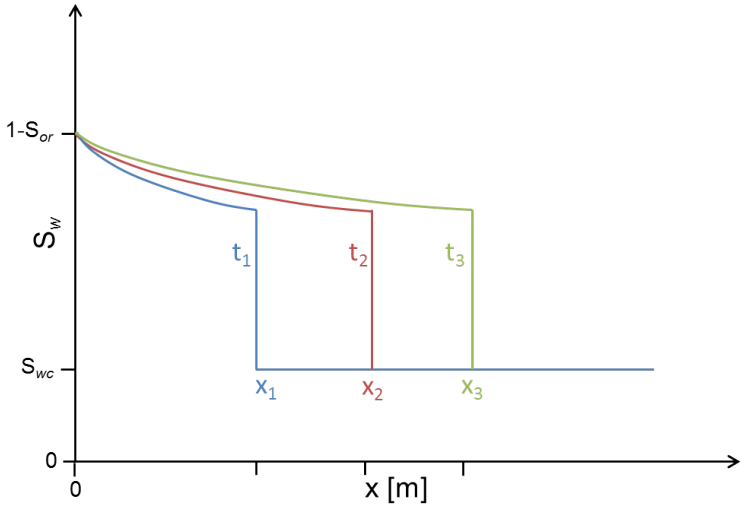

Figure 3.1. Typical Buckley-Leverett profile of water saturation as a function of distance for viscous dominated flow where gravity is ignored. The distance travelled scales linearly with time.

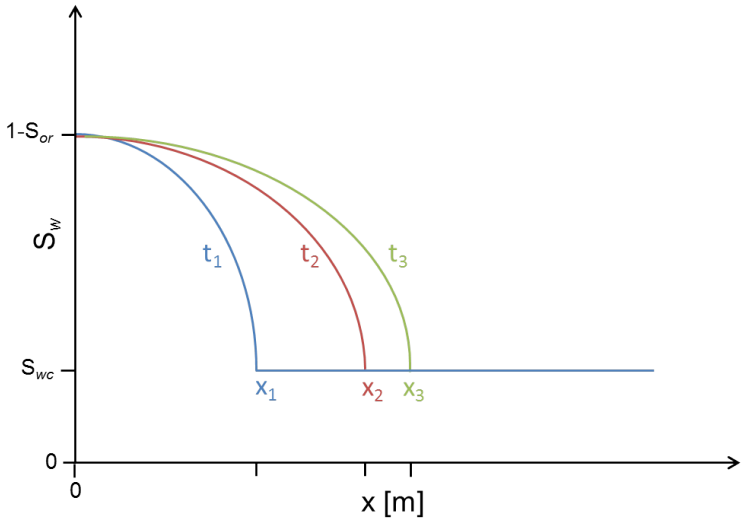

Figure 3.2. Saturation profile for capillary dominated flow where the profile is equally spaced in time but not in space. The distance travelled scales as the square root of time.

Then from analogy with the Buckley-Leverett analysis, we state that for some capillary fractional flow $F(1 \geq F \geq 0)$ and constant C:

$$\omega = \frac{2C}{\phi} F'(S_w) \tag{3.16}$$

Hence

$$\frac{d\omega}{dS_w} = \frac{2C}{\phi} F''(S_w) \tag{3.17}$$

The factor $2C/\phi$, where C is a constant is introduced to make F dimensionless. The dimensions of C are length/$\sqrt{time}$ or m.s$^{-1/2}$. Then we define the following derivatives:

$$\frac{\partial S_w}{\partial t} = \frac{\partial S_w}{\partial \omega}\frac{\partial \omega}{\partial t} = -\omega\frac{1}{2t}\frac{\partial S_w}{\partial \omega} \tag{3.18}$$

$$\frac{\partial S_w}{\partial x} = \frac{\partial S_w}{\partial \omega}\frac{\partial \omega}{\partial x} = \frac{1}{\sqrt{t}}\frac{\partial S_w}{\partial \omega} \tag{3.19}$$

With these derivations, we can rewrite Equation 3.10 as an ordinary differential equation for co-current flow:

$$\omega\frac{\partial S_w}{d\omega} + 2\frac{\partial}{\partial \omega}\left(D(S_w)\frac{\partial S_w}{\partial \omega}\right) - 2Cf'_w(S_w)\frac{\partial S_w}{\partial \omega} = 0 \tag{3.20}$$

and rewrite Equation 3.11 for counter-current flow:

$$\omega\frac{\partial S_w}{\partial \omega} + 2\frac{\partial}{\partial \omega}\left(D(S_w)\frac{\partial S_w}{\partial \omega}\right) = 0 \tag{3.21}$$

Then we integrate once, for co-current flow:

$$\int(\omega - f'(S_w))dS_w = -\frac{2D}{\phi}\frac{dS_w}{d\omega} \tag{3.22}$$

and for counter-current flow:

$$\int \omega dS_w = -\frac{2D}{\phi}\frac{dS_w}{d\omega} \tag{3.23}$$

note that the integration constant is zero since we define *F(S_{wir})=0* and also *D(S_{wir})=0*.

Then, we substitute F in Equation 3.16 and we obtain for co-current flow:

$$(F - f)F'' = -\frac{\phi}{2C^2}D \tag{3.24}$$

for counter-current flow:

$$FF'' = -\frac{\phi}{2C^2}D \tag{3.25}$$

Formally this is an analytic solution to the equations, since they define F and hence the whole solution.

3.2.2. Solving the Equations

Schmid et al. 2011 presents a formal solution to Equation 3.24 as

$$F = \int\int \frac{-\phi}{2C^2}\frac{D}{(F-f)}d^2S_w \tag{3.26}$$

and similarly with $f = 0$ for counter-current flow.

Equation 3.26 is implicit in F and so can only be solved iteratively. *Schmid et al.* 2011 do this by first assuming a functional form for $F(F = S_w$ is the first guess), solving Equation 3.26 and finding a new $F(S_w)$, which is then placed in the integral again.

To evaluate F and the solution $S_w(\omega)$ we do require an iterative method. We instead develop a simple approach to find the solution using a numerical method, using backward-difference, Figure 3.3, giving:

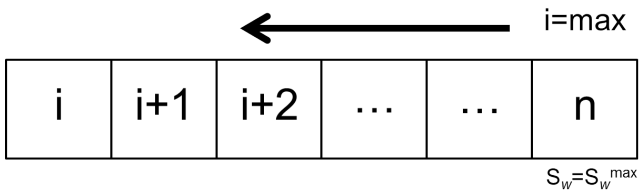

Figure 3.3. Schematic of the backward difference approximation used to find solutions for spontaneous imbibition.

$$F''(y_i) \approx \frac{F(y_{i-2}) - 2F(y_{i-1}) + F(y_i)}{\Delta y^2} \tag{3.27}$$

now, we substitute Equation 3.27 in Equation 3.24 for co-current flow:

$$\left(\frac{F(y_{i-2}) + F(y_i) - 2F(y_{i-1})}{\Delta y^2}\right)(F(y_i) - f(y_i)) = -\frac{\phi}{2C^2}D(y_i) \tag{3.28}$$

similarly, we substitute Equation 3.27 in Equation 3.25 for counter-current flow:

$$\left(\frac{F(y_{i-2}) + F(y_i) - 2F(y_{i-1})}{\Delta y^2}\right)F(y_i) = -\frac{\phi}{2C^2}D(y_i) \tag{3.29}$$

Now, we multiply both sides by Δy^2, for co-current flow:

$$(F(y_i) + F(y_{i-2}) - 2F(y_{i-1}))(F(y_i) - f(y_i)) = -\frac{\phi}{2C^2}D(y_i)\Delta y^2 \tag{3.30}$$

for counter-current flow:

$$(F(y_i) + F(y_{i-2}) - 2F(y_{i-1}))F(y_i) = -\frac{\phi}{2C^2}D(y_i)\Delta y^2 \tag{3.31}$$

Let us assume that $X = F(y_i)$, then Equation 3.30 for co-current flow becomes:

$$X^2 + (F(y_{i-2}) - 2F(y_{i-1}) - f(y_i))X - F(y_{i-2})f(y_i) + 2F(y_{i-1})f(y_i) + \frac{\phi}{2C^2}D(y_i)\Delta y^2 = 0 \tag{3.32}$$

and for counter-current flow:

$$X^2 + (F(y_{i-2}) - 2F(y_{i-1}))X + \frac{\phi}{2C^2}D(y_i)\Delta y^2 = 0 \tag{3.33}$$

from the quadratic formula:

$$\frac{-b \pm \sqrt{b^2 - 4ac}}{2a} \tag{3.34}$$

Hence, the solution for $X = F(y_i)$ for co-current flow:

$$F(y_i) = \frac{\Big(F(y_{i-1}) - 0.5F(y_{i-2}) + 0.5f(y_i)\Big) + \sqrt{0.25\Big(F(y_{i-2}) - 2F(y_{i-1}) - f(y_i)\Big)^2}}{-\Big(f(y_i)(F(y_{i-2}) - 2F(y_{i-1})) + \Big(\frac{\phi}{2C^2}\Big)D(y_i)\Delta y^2\Big)} \tag{3.35}$$

For counter-current flow:

$$F(y_i) = \Big(F(y_{i-1}) - 0.5F(y_{i-2})\Big) + \sqrt{\Big(F(y_{i-1}) - 0.5F(y_{i-2})\Big)^2 - \Big(\frac{\phi}{2C^2}\Big)D(S_w)\Delta y^2} \tag{3.36}$$

Finally, we show the solutions as a function of water saturation (S_w) in equal increments ΔS_w, for co-current flow:

$$F(S_w) = \frac{\Big(F(S_w - \Delta S_w)) - 0.5F(S_w - 2\Delta S_w) + 0.5f(S_w)\Big) + \sqrt{0.25\Big(F(S_w - 2\Delta S_w) - 2F(S_w - \Delta S_w)) - f(S_w)\Big)^2}}{-\Big(f(S_w)(F(S_w - 2\Delta S_w) - 2F(S_w - \Delta S_w)) + \Big(\frac{\phi}{2C^2}\Big)D(S_w)\Delta S_w^2\Big)} \tag{3.37}$$

For counter-current flow:

$$F(S_w) = \Big(F(S_w - \Delta S_w) - 0.5F(S_w - 2\Delta S_w)\Big) + \sqrt{\Big(F(S_w - \Delta S_w) - 0.5F(S_w - 2\Delta S_w)\Big)^2 - \Big(\frac{\phi}{2C^2}\Big)D(S_w)\Delta S_w^2}, \tag{3.38}$$

These equations have been coded into a spreadsheet, where we guess the value of C in an iterative process to satisfy the following conditions:

$$F(S_{wir}) = 0 \tag{3.39}$$

In addition the integrated saturation curve must equal to the total volume imbibed:

$$\int_{S_{wir}}^{S_{w,max}} x(S_w, t)dS_w = \frac{q_w(t)}{\phi} = \frac{2C\sqrt{t}}{\phi} \tag{3.40}$$

where we can re-arrange and approximate the integral to give:

$$\Sigma_{i=1}^{n} F'(S_w, i)\Delta S_w \approx \frac{q_w(t)}{\phi} = \frac{\phi}{2C} = 1 \tag{3.41}$$

We start the process by guessing an initial value of C and we keep changing it until

we satisfy Equation 3.39. This can be done easily by hand to determine C to 3 or 4 significant figures in few steps. For the construction of the analytical solution of co-current and counter-current with an example, please refer to Appendix B.1.

Note that the analytical solution is only valid for the early time of imbibition, t^*, where the flow is entirely governed by capillary forces in the absence of constraining boundaries [*Li and Horne*, 2001, *Suzanne et al.*, 2003, *Olafuyi et al.*, 2007], Figure 3.4. The late time is governed by boundary/diffusion where the water front reaches the boundary and the recovery rate decays exponentially.

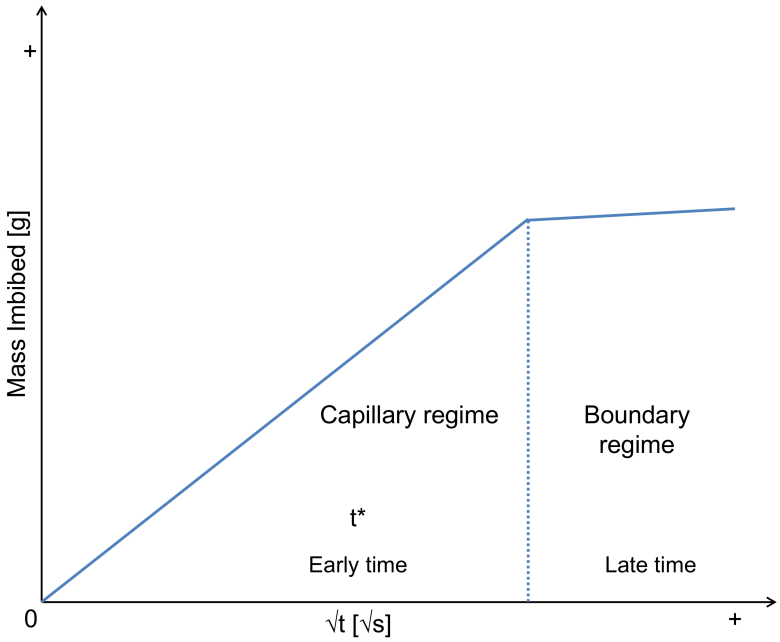

Figure 3.4. Schematic showing the early time of imbibition where the flow is entirely governed by capillary forces and the analytical solution is valid. The late time is governed by boundaries where the analytical solution is not valid.

3.2.3. Scaling Equation

There have been several attempts to scale spontaneous imbibition data from the core-scale to the field-scale [*Washburn*, 1921, *Mattax and Kyte*, 1962, *Ma et al.*, 1997, *Tavassoli et al.*, 2005, *Li and Horne*, 2006, *Mason et al.*, 2012]. This is important to estimate the recovery from naturally fractured reservoirs.

Schmid and Geiger 2012, 2013 also found the closed-form solution for the scaling of early time spontaneous imbibition which has the same functional form for co-current and counter-current spontaneous imbibition:

$$t_D = \left(\frac{2C}{\phi L_c}\right)^2 t \tag{3.42}$$

where

$$L_c = \sqrt{\frac{V}{\Sigma_{i=1}^{n} \frac{A_i}{X_{Ai}}}} \tag{3.43}$$

and L_c is the characteristic length, V is the bulk volume, A_i is the area perpendicular to the ith direction, and X_{Ai} is the distance from A_i to the no-flow boundary [*Ma et al.*, 1997]. For one-dimensional linear flow $L_c = L$, the length of the system. The dimensionless time can be further interpreted as:

$$q_w(t) = 2C\sqrt{t} \tag{3.44}$$

Hence, the dimensionless time becomes:

$$t_D = \left(\frac{q_w(t)}{\phi L_c}\right)^2 \tag{3.45}$$

These equations and their solutions will now be compared to experimental measurements.

3.3. Experimental Procedure

3.3.1. Fluids and Conditions

We conduct our experiments at ambient conditions of atmospheric pressure and room temperature of 20±1°C. We use air as the non-wetting phase and brine, with 5 wt. % sodium chloride (NaCl) and 1 wt. % potassium chloride (KCl) mixed with deionised water, as the wetting liquid phase. In addition, we equilibrate the brine with the carbonate samples for 48 hours by mixing them using magnetic stirrer to eliminate any reaction between the brine and the rock surface which might alter the rock morphology. Then, we leave the brine for additional 48 hours to settle and finally we filter it, using a fine filter paper, to remove the particles that might block the flow pathways of the rocks.

The density of brine is 1,040.8 kg/m^3 measured using Anton Paar DMA 5000 M and the viscosity is reported as 1.0085 mPa s [*Lide*, 2004]. The air/brine interfacial tension is 0.073 N/m measured using Ramé-Hart model 590 device and the air viscosity is reported as 0.0018 mPa s [*Tavassoli et al.*, 2005].

3.3.2. Mass Imbibition

Before we start the spontaneous imbibition experiment, we do our routine analysis by taking the dimensions of the core, measuring the dry weight of the core, and measuring the helium porosity. However, we use the mass balance technique to measure the porosity for the 204.7 and 286.7 mm length cores, where we take the dry weight and compare it to the fully saturated core with degassed brine post spontaneous imbibition experiment,

since the helium porosimeter cell is too small to fit them–for further details on measuring the porosity please refer to Appendix A.1.

We measure the permeability of the core using gas before starting the spontaneous imbibition experiment, or brine after finishing the spontaneous imbibition experiment where we use a Hassler type cell with cylindrical confining fluid. We use three different cell lengths to fit our different core lengths.

To start our SI experiment, we apply heat shrink wrapping to confine the outer boundaries of the core and make sure that only co-current imbibition is applied. Then, we weigh the core again with the heat shrink and after that we attach the core to a Mettler Toledo XP5003S balance with 0.001 g accuracy and we lift the brine reservoir at the bottom of the core surface to be in contact with the core, Figure 3.5. Before that moment we start recording the weight changes over time as the balance is connected to the computer. We have three recording settings; we record 10 points per second, 5 points per second, and 2 points per second. We use the 10 points per second for Ketton, as it has the highest permeability and the imbibition process is the quickest, 5 points per second for Estaillades and 2 points per second for Portland.

After the imbibition process is finished, we weigh the core again and by that we can measure the residual gas saturation (S_{gr}). We assume that since we run the experiments at ambient conditions there is no compression of the gas after it is trapped. After that, we vacuum saturate the cores for 24 hours to make sure that there is no air in the system. Then we insert the core into the Hassler cell to measure the permeability where we keep injecting degassed brine until we reach to the steady state–for further details on measuring the absolute permeability please refer to Appendix A.3.

Finally, we take the core out and weigh it to measure the porosity using the mass balance technique. For consistency, we replicate each experiment with a core from the same block. Table 3.1, summarises the properties of the cores used in the mass imbibition experiment.

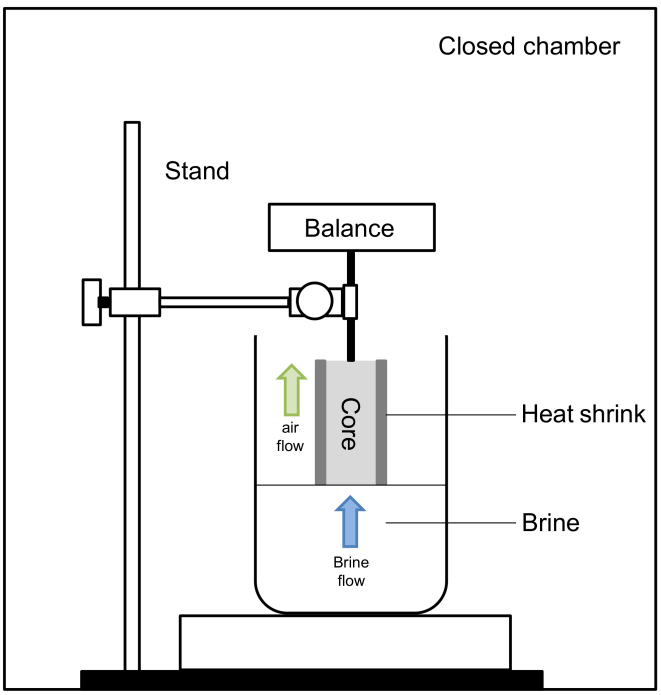

Figure 3.5. Schematic of the experimental apparatus for ambient conditions co-current spontaneous imbibition, where the mass of brine imbibied into the rock is measured as a function of time.

Table 3.1. Summary of the petrophysical properties measured for the mass imbibed experiments. E, K, and P denote Estaillades, Ketton, and Portland respectively.

Core Label	D [mm]	L [mm]	ϕ [%]	k [m^2]	S_{gr}
E1	37.8	76.3	28.0	1.34×10^{-13}	0.29
E2	37.8	76.3	27.8	3.53×10^{-13}	0.28
E3	37.9	204.0	27.5	1.19×10^{-13}	0.25
E4	37.9	204.0	27.5	1.55×10^{-13}	0.25
E5	37.9	292.0	28.2	3.94×10^{-13}	0.23
E6	37.9	293.0	28.0	3.28×10^{-13}	0.23
K1	37.8	76.0	23.4	1.62×10^{-12}	0.35
K2	37.8	76.3	20.5	1.37×10^{-12}	0.27
K3	38.1	205.0	23.2	1.88×10^{-12}	0.34
K4	38.0	205.0	21.7	1.99×10^{-12}	0.28
K5	38.0	280.0	22.7	2.23×10^{-12}	0.29
K6	38.0	293.0	22.5	2.54×10^{-12}	0.35
P1	37.8	76.3	16.1	1.01×10^{-14}	0.21
P2	37.9	76.3	19.6	1.37×10^{-14}	0.25
P3	38.3	205.0	19.8	1.52×10^{-14}	0.24
P4	38.0	205.0	20.0	6.51×10^{-15}	0.22
P5	38.0	280.0	19.5	1.82×10^{-14}	0.36
P6	38.0	282.0	19.0	3.50×10^{-14}	0.26

3.3.3. CT Imaging

We use one core of each rock type (37 mm $\times$ 76 mm) in this study, Table 3.2. We track the movement of the saturation front inside the rock by using a medical X-ray scanning instrument (HD-350E, Universal Systems). The purpose of the CT scanner is to identify the saturation profile and scale it to $\sqrt{t}$ to compare it with the analytical solution derived by *Schmid et al.* 2011 for spontaneous imbibition. We measure the weight of the core before and after we apply the heat shrink, when the core is completely dry. We apply the heat the shrink on the boundary of the core to make sure that co-current flow is applied.

We place the core vertically in the CT scanner domain and we set the scanner operating parameters on a tube current of 225 mA and an energy level of radiation of 120 kV. After setting the scanner, we take a dry scan of the core and keep it as a reference which we will use to measure the saturation inside the core. Then we raise the brine reservoir until it touches the bottom surface of the core. Then, we take multiple scans at different times with one second acquisition time until the saturation front reaches the top of the core. Finally, we take a final scan when the saturation front reaches the top of the core and we use that as a reference scan. We measure the water saturation at each scan after

the dry scan and before it is saturated with brine by using the following Equation:

$$S_w = \frac{CT_{obj} - CT_{dry}}{CT_{brine} - CT_{dry}} \tag{3.46}$$

where S_w is the water saturation, CT_{obj} is the CT value of the processed image, CT_{dry} is the CT value of the dry image, and CT_{brine} is the CT value of fully saturated rock.

Then, we process the images to obtain the saturation profile. Since we know the length of the core, we divide it by the pixels in the y-direction and thus we get the equivalent length of each pixel. Then, we take the average of the CT numbers in the x-axis of each scan we want to measure and compare the dry and fully saturated scans by using Equation 3.46. However, since the fully saturated scan still contains residual saturation, we multiply the equation with the final water saturation from the mass-balance calculation to obtain accurate saturation values. We can then measure the saturation profile.

Table 3.2. Summary of the petrophysical properties measured for the CT scanning co-current spontaneous imbibition experiment.

Core Label	D [mm]	L [mm]	ϕ [%]	k [m^2]	S_{gr}
E*	37.7	76.5	27.6	2.10×10^{-13}	0.28
K*	37.8	76.6	20.7	2.35×10^{-12}	0.28
P*	37.9	76.4	22.1	5.23×10^{-15}	0.29

3.4. Capillary Pressure and Relative Permeability

In the Buckley-Leverett analysis for viscous dominated flow only relative permeability is needed to compute the analytical solution. However, for capillary dominated flow, relative permeability and imbibition capillary pressure are needed to compute the analytical solution. In our theoretical analysis we will assume Corey or power-law expressions for relative permeability and capillary pressure:

$$k_{rw} = k_{rw,max}\left(\frac{S_w - S_{wi}}{1 - S_{wr} - S_{gr}}\right)^n \tag{3.47}$$

where k_{rw} is the water relative permeability, $k_{rw,max}$ is the maximum water relative permeability, S_w is the water saturation, S_{wi} is the initial water saturation, S_{gr} is the residual gas saturation, and n is the Corey water exponent.

$$k_{rg} = k_{rg,max}\left(\frac{1 - S_w - S_{wi}}{1 - S_{wr} - S_{gr}}\right)^m \tag{3.48}$$

where k_{rg} is the gas relative permeability, $k_{rg,max}$ is the maximum gas relative permeability, S_w is the water saturation, S_{wi} is the initial water saturation, S_{gr} is the residual gas saturation, and m is the Corey gas exponent.

$$P_c = P_{c,entry} \left(\frac{S_w - S_{wi}}{1 - S_{wi} - S_{gr}} \right)^{\alpha} \tag{3.49}$$

where P_c is the capillary pressure, $P_{c,entry}$ is the entry capillary pressure, S_w is the water saturation, S_{wi} is the initial water saturation, S_{gr} is the residual gas saturation, and α is the capillary pressure exponent.

Then, we adjust the following parameters: $k_{rw,max}$, n, $k_{ro,max}$, m, $P_{c,entry}$, α so that the experimental results and analytical predictions match. However, this is not a unique determination of multiphase flow parameters since we have three functions–two relative permeabilities and a capillary pressure–to match one measured profile $S_w(\omega)$. We will explore this further in the discussion section.

We use these simplified power-law forms for the relative permeability simply for illustrative purposes and do not claim or imply that these are necessarily valid for complex carbonate samples. However, the use of power-law fitting to carbonate relative permeability has been applied successfully by *Ott et al.* 2014, while other experimental field data can be reasonably captured by these functional forms (see, for instance, *Hafez et al.* 2013).

3.5. Results and Discussion

3.5.1. Measurements of Mass Imbibed

Figure 3.6 shows the mass imbibed as a function of time of the various lengths of each rock. We can see that the rate of mass of water imbibed is a function of the permeability of the rocks, with faster rates for higher permeability rocks. The early imbibition shows a rapid increase of brine flow rate which then decays at late time.

To find the value of C, which is a parameter that quantifies the rock's ability to imbibe, we study the imbibition data, Figure 3.6. We process this figure further by taking $\sqrt{t}$ instead of t, Figure 3.7, on the x-axis. We divide the mass imbibed after converting it to a volume (by dividing by the density of brine) by the area of the core open to water flow and by taking the slope we obtain the parameter $2C$ [m/$\sqrt{s}$]. We divide by 2 to obtain the value of C from Equation 3.44, Figure 3.8.

We see a sudden jump in the mass imbibed at the beginning for the experiment that affects high permeability rocks more. This is cause by a meniscus jump when the core is first put in contact with the brine [*Labajos-Broncano al.*, 2001, *Washburn*, 1921]. We

take the slope after this jump to find C–see Figure 3.8. At late time, when the water reaches the end of the core, again we can see a deviation from $\sqrt{t}$ scaling–this is ignored in our calculation of C. We can see that the constant C is roughly constant regardless of the length of the core, Figure 3.9. The error bars in this plot indicate the uncertainty from ignoring the meniscus jump region: they show the range of different slopes possible from the results.

We plot the results by using the dimensionless time, Equation 3.42, in Figure 3.10. In this case, for co-current spontaneous imbibition, the characteristic length is the same as the actual length of the core as the flow is one-dimensional. The recovery in this figure is the normalised recovery which is the actual recovery divided by the ultimate recovery of the rock. We can see that Ketton does not scale uniformly with time due to the severity of the meniscus jump in this high permeability rock while Portland does not scale uniformly at late time. However, for Estaillades the scaling works well and all the results fall, roughly, onto one universal curve.

The insensitivity of the results to core length implies that gravitational forces are negligible in these experiments. The gravitational pressure drop across the core is at most $\Delta\rho$gL where $\Delta\rho$ is the density contrast. This is at most 2,985 Pa for the largest cores. For comparison the air entry capillary pressure derived from the MICP measurements is 5,515 Pa, 3,447 Pa, and 33,784 Pa for Estaillades, Ketton, and Portland respectively: in all cases the capillary pressure is larger than the gravitational pressure difference.

The higher permeability rocks imbibe faster. For a given driving force, from Darcy's law, the flow rate is proportional to permeability k. However, here the driving force is capillary pressure, which using the Leverett J-function Equation 1.5, scales as $1/\sqrt{k}$. The end result is an imbibition rate that theoretically scales as $\sqrt{k}$. We will test this scaling later in this chapter.

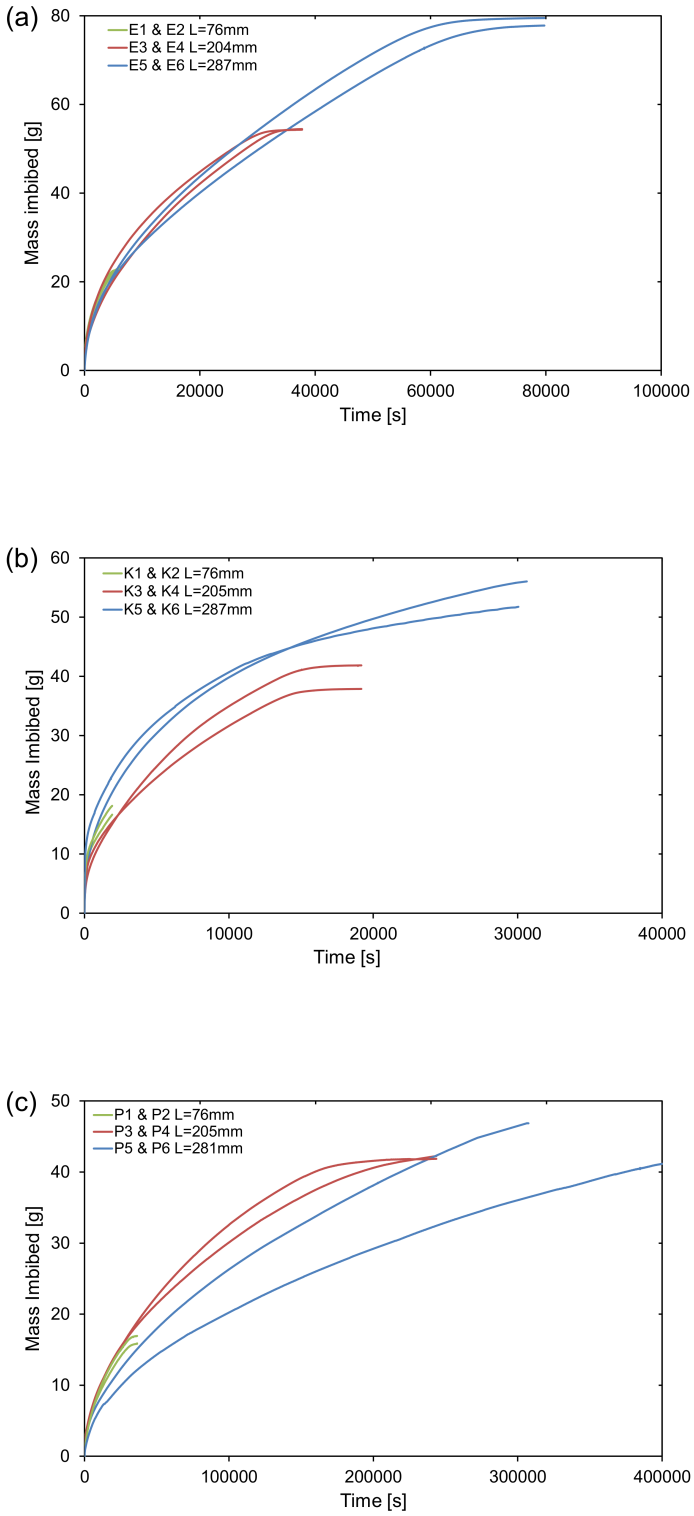

Figure 3.6. Mass imbibed as a function of time for an air/brine system at ambient conditions of varying lengths for (a) Estaillades, (b) Ketton, and (c) Portland.

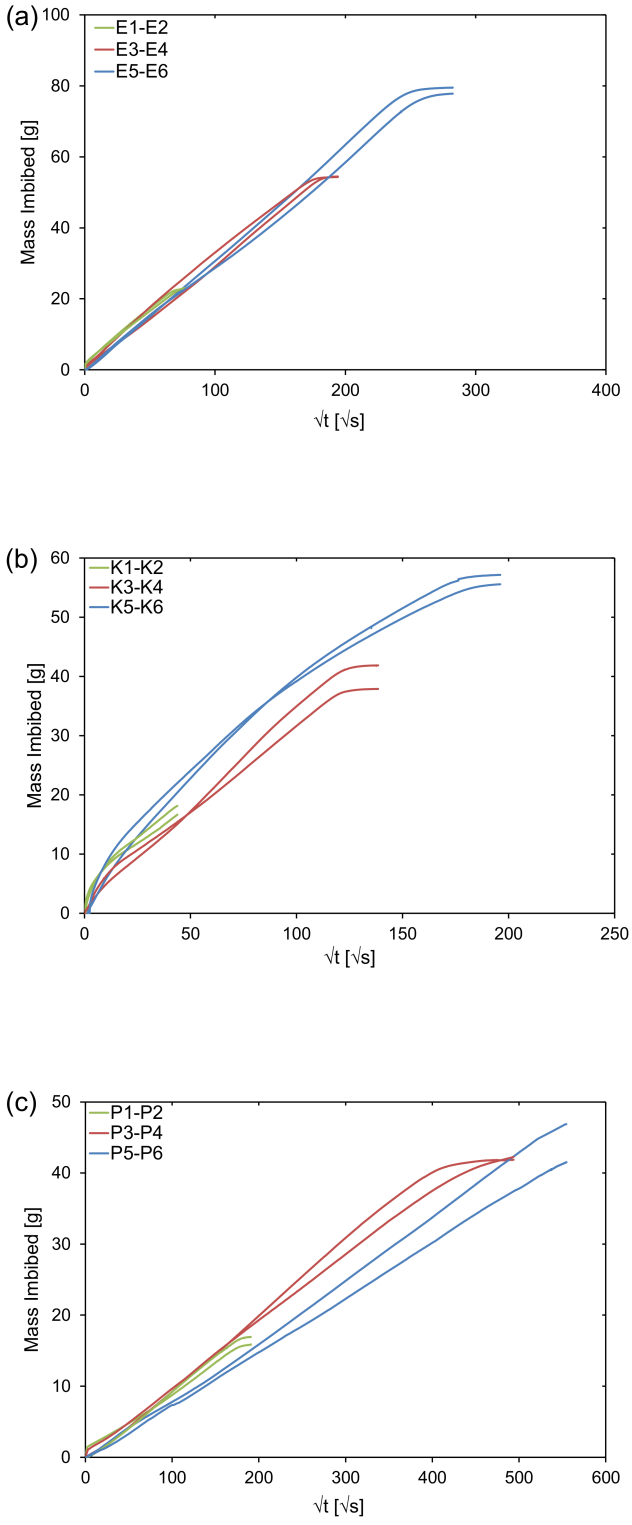

Figure 3.7. Mass imbibed as a function of the square root of time for an air/brine system at ambient conditions of varying lengths for (a) Estaillades, (b) Ketton, and (c) Portland.

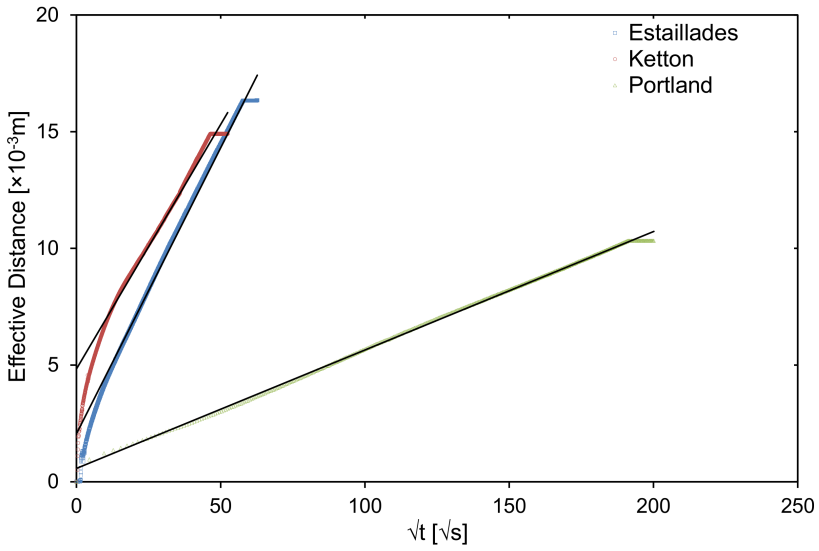

Figure 3.8. The final step in the analysis is dividing the volume by the area and taking the slope. Noting that the slope is equivalent to $2C$ from Equation 3.44 where we need to divide the slope by 2. The black lines are the slopes for each rock after the meniscus jump. Here the results for the shortest cores cores E1, K1, and P1 are shown; the sharp rise at the earliest time is a meniscus jump which is ignored in the analysis as well as the late time.

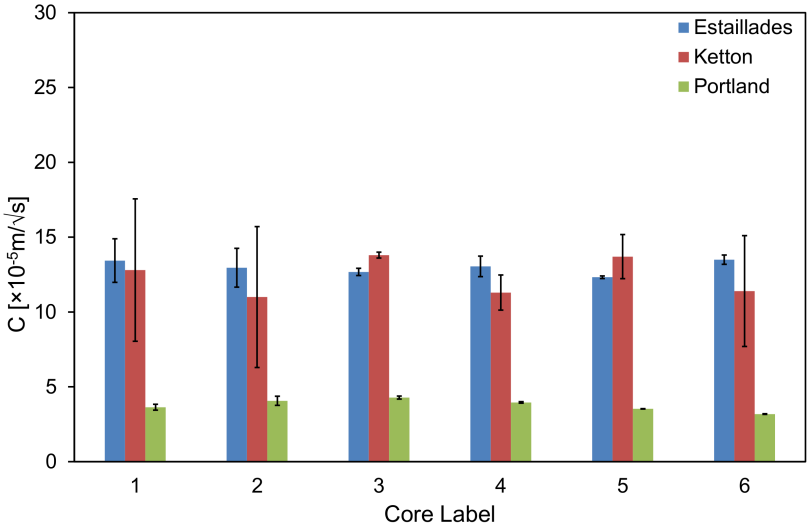

Figure 3.9. The C values from the mass imbibition data for all the rocks in Table 3.1/Figure 3.6.

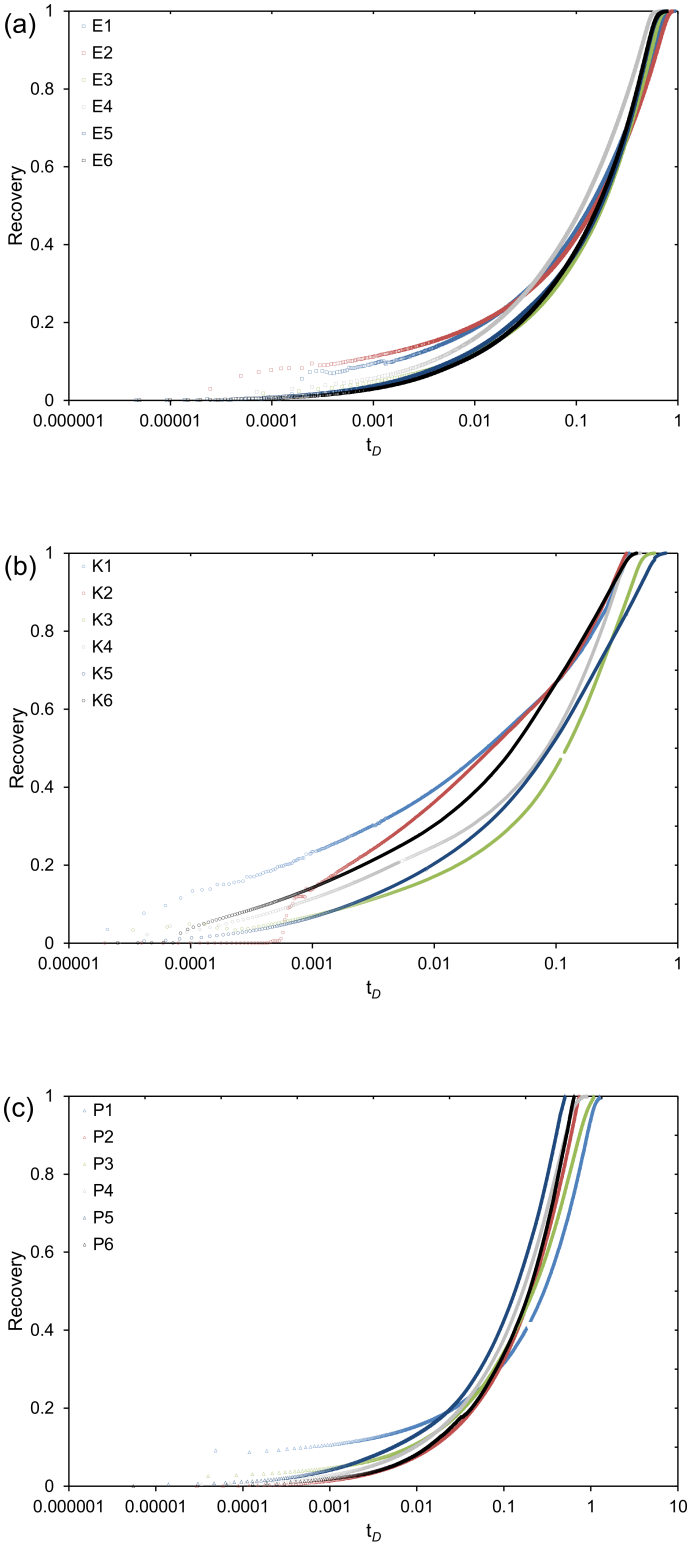

Figure 3.10. Re-processing Figure 3.6 to a dimensionless form by using the *Schmid and Geiger* 2012 expression, Equation 3.42, and using the experimental values of ϕ and L from Table 3.1 and the values of C from Figure 3.9 for (a) Estaillades, (b) Ketton, and (c) Portland. We normalise the y-axis by dividing the recovery by the ultimate recovery (R/R_∞) to have a standard comparison between all the rocks.

3.5.2. CT Imaging Experiments and Comparison with Analytical Solutions

Figure 3.11 shows images of the CT saturation profile of each rock at different times. We can see that Estaillades has a hemi-spherical outwards front, Portland has a hemi-spherical inwards front that merged to form a piston-like front at later times, while Ketton has a piston-like displacement throughout the entire imbibition time. This might be because Ketton is less heterogeneous than the other rocks or an injection configuration artefact or an experimental artefact since heat shrink wrapping are not perfect sealers to isolate the boundaries.

Figure 3.12 shows the slice averaged saturation profile of each rock at different times as a function of distance. The selected times cover wide range of the water distance travelled for Estaillades and Ketton. However, for Portland, the times selected are after the water front merged into a piston-like. We can see the shape is different than the profile for viscous dominated flow (Buckley-Leverett). Figure 3.13 shows the same profile in a normalised length. To further investigate this, we divide the saturation profile by $\sqrt{t}$ (ω), Figure 3.14. We can see that all the curves collapse approximately into one universal curve as a function of ω. Then, we compare the water saturation as a function of ω of each rock experimentally as well as analytically by using the relative permeability and capillary pressure from the matched data, Figure 3.15.

The relative permeability and capillary pressure was tuned to match the experimental results by varying the Corey and capillary pressure exponents by hand. By varying the Corey parameters we found that the water relative permeability and capillary pressure have the most impact on the analytical solution, while the air relative permeability had little impact on the results. This makes physical sense as the air has a low viscosity and is easily displaced–the movement of the water front is essentially entirely controlled by the water relative permeability (the ability to flow) and the capillary pressure (the driving force). Table 3.3 shows the input parameters used to construct the analytical solution that matches the data.

Our best match is when the k_{rw} exponent ≥ 8. Since the core is initially dry, the water relative permeability is low, as water will first preferentially fill the largely immobile micro-porosity, giving a large change in saturation but little increase in relative permeability, indicative of a high Corey exponent. The relative permeabilities and capillary pressures used for the matching are shown in Figures 3.16 and 3.17 respectively. The water saturation will have to increase to a large value in order to gain conductivity through the macro-porosity [*Fernø et al.*, 2013]. As we show in the next chapter, this process also leads to lower values of S_{gr}, Table 3.1, than the residual non-wetting phase saturations in water-wet systems with high initial non-wetting phase saturations. If the rock is initially dry, piston-like advance is favoured over snap-off due to the lack of connected water layers, leading to less trapping. Once the water layers are connected,

snap-off will be favoured and can trap the remaining gas in the rock. The presence of initial water saturation provides better conductivity and thus faster water fronts with smaller Corey exponents [*Zhou et al.*, 2000, *Li et al.*, 2002].

Several studies have estimated relative permeability and capillary pressure from spontaneous imbibition measurements [*Haugen et al.*, 2014, *Li and Horne*, 2005]. In this study, we show that we can estimate the relative permeability and capillary pressure from matching the analytical solution with the experimental data. The solution is not unique since we have only one measured function and three saturation-dependent properties– two relative permeabilities and the imbibition capillary pressure. However, these experiments could be used in conjunction with traditional coreflooding to determine all three functions together. For instance, if we had measured the two relative permeability functions, we should be able to find - uniquely - the capillary pressure that gave the measured imbibition profile. Moreover, by using conventional measurements of relative permeability (steady-state or using Buckley-Leverett theory in an unsteady-state experiment) and the spontaneous imbibition saturation profile, we can measure the imbibition capillary pressure. We could also determine the imbibition relative permeability from a measured capillary pressure and the spontaneous imbibition saturation profile. This is, however, a topic for future work, as we have not independently measured multiphase flow properties for these samples. As it stands, we can match the data but the functions used are not uniquely determined. Furthermore, this approach is only possible if we see $\sqrt{t}$ scaling of the imbibition front: a different method is needed if this is not the case.

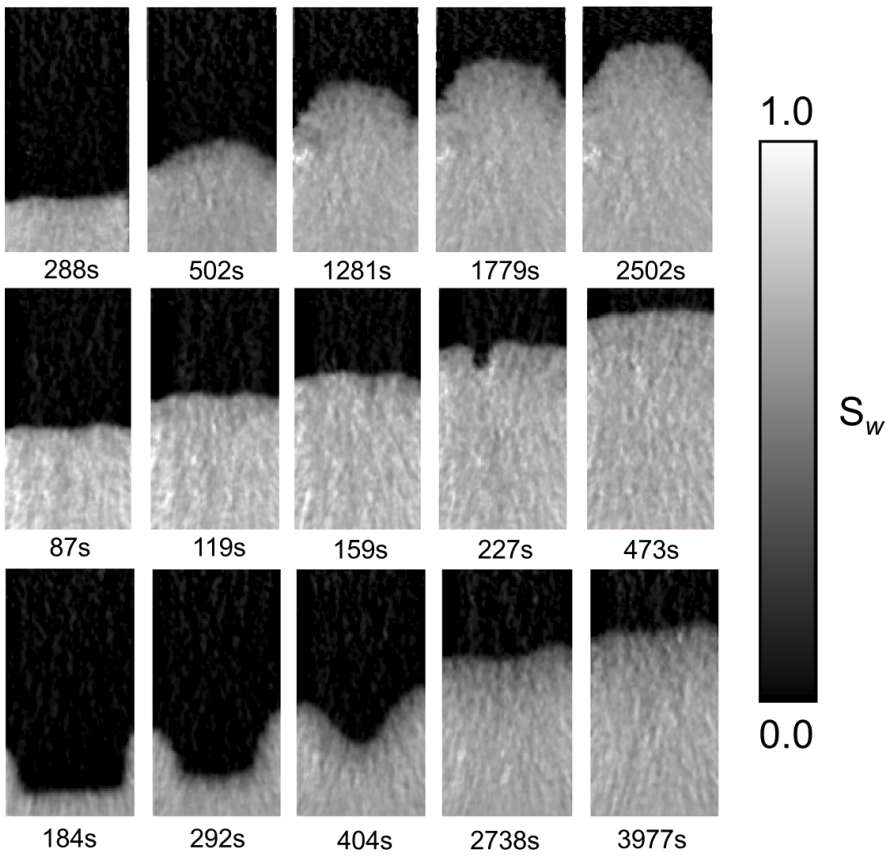

Figure 3.11. CT cross section of air/brine spontaneous imbibition at different time intervals for (top) Estaillades, (middle) Ketton, and (bottom) Portland limestone rocks.

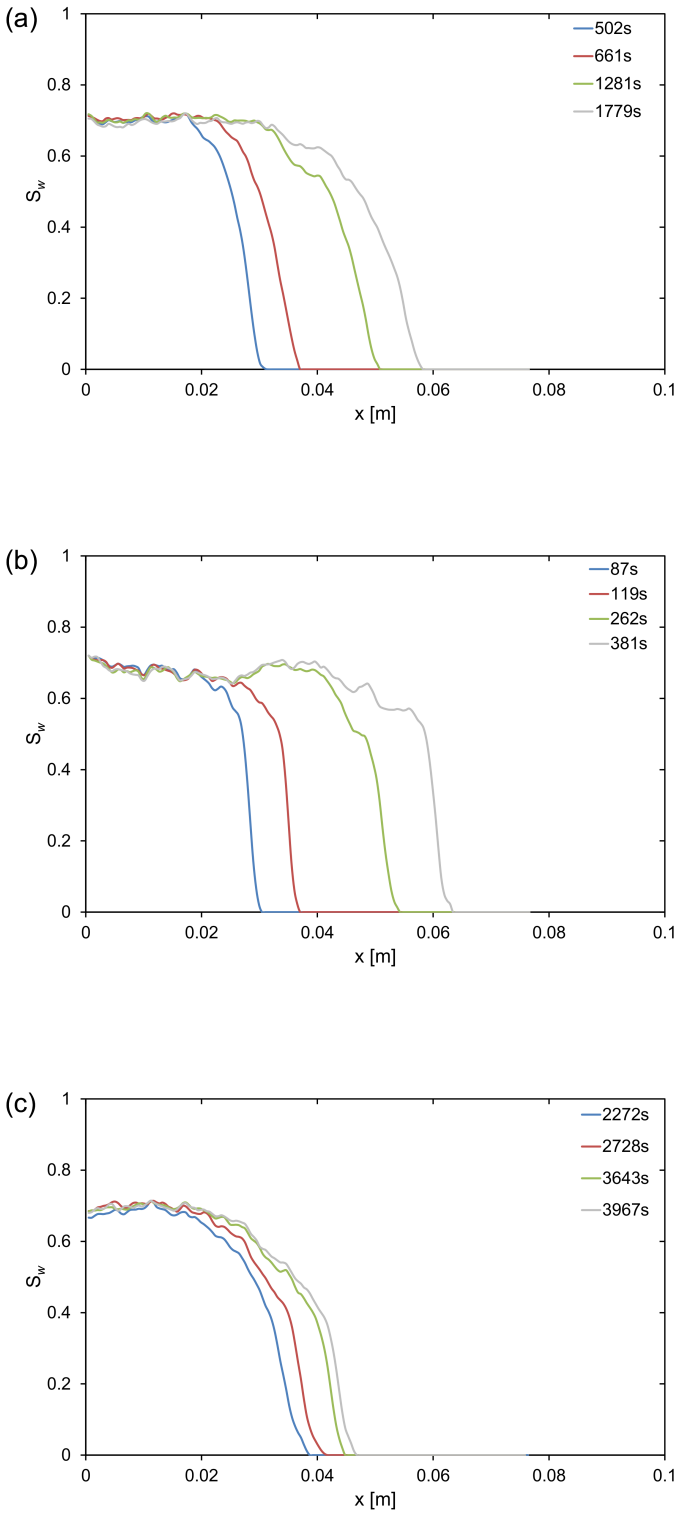

Figure 3.12. Saturation profiles obtained from the CT acquisition as function of distance for (a) Estaillades, (b) Ketton, and (c) Portland.

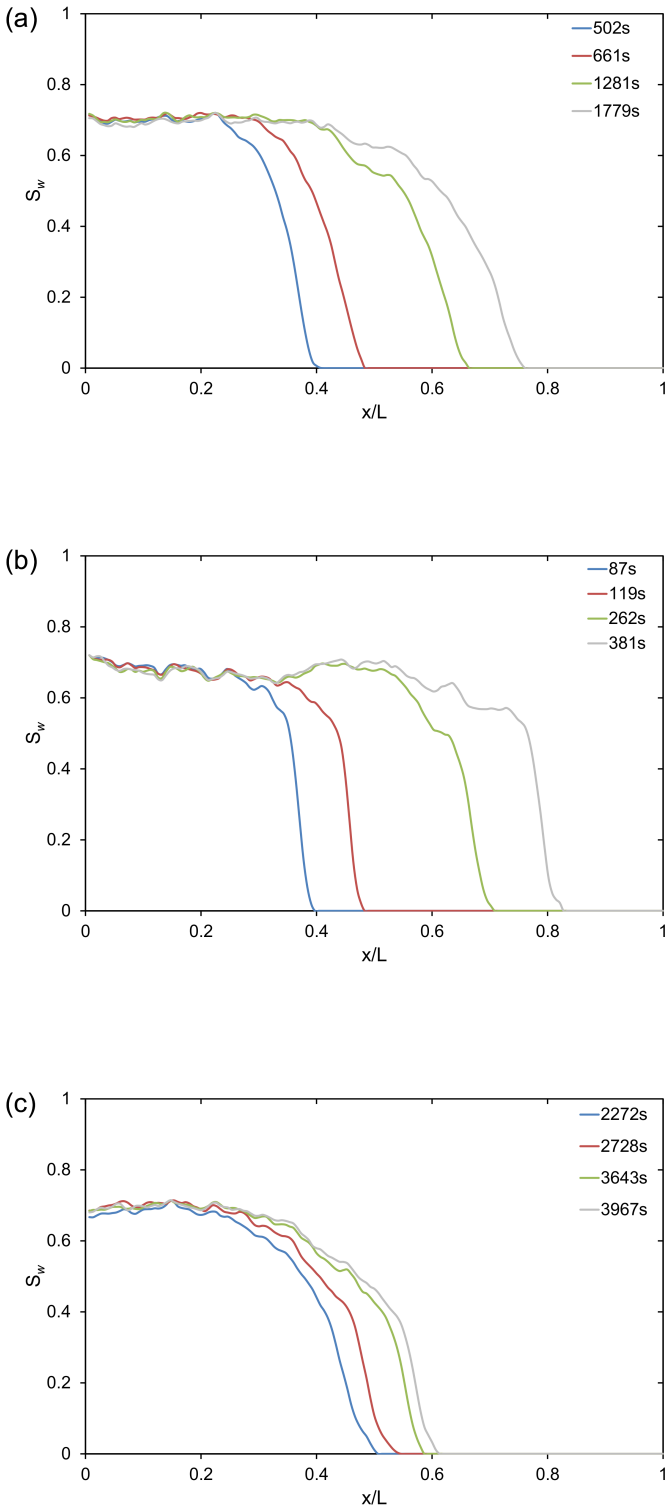

Figure 3.13. Saturation profiles obtained from the CT acquisition as function of normalised length for (a) Estaillades, (b) Ketton, and (c) Portland.

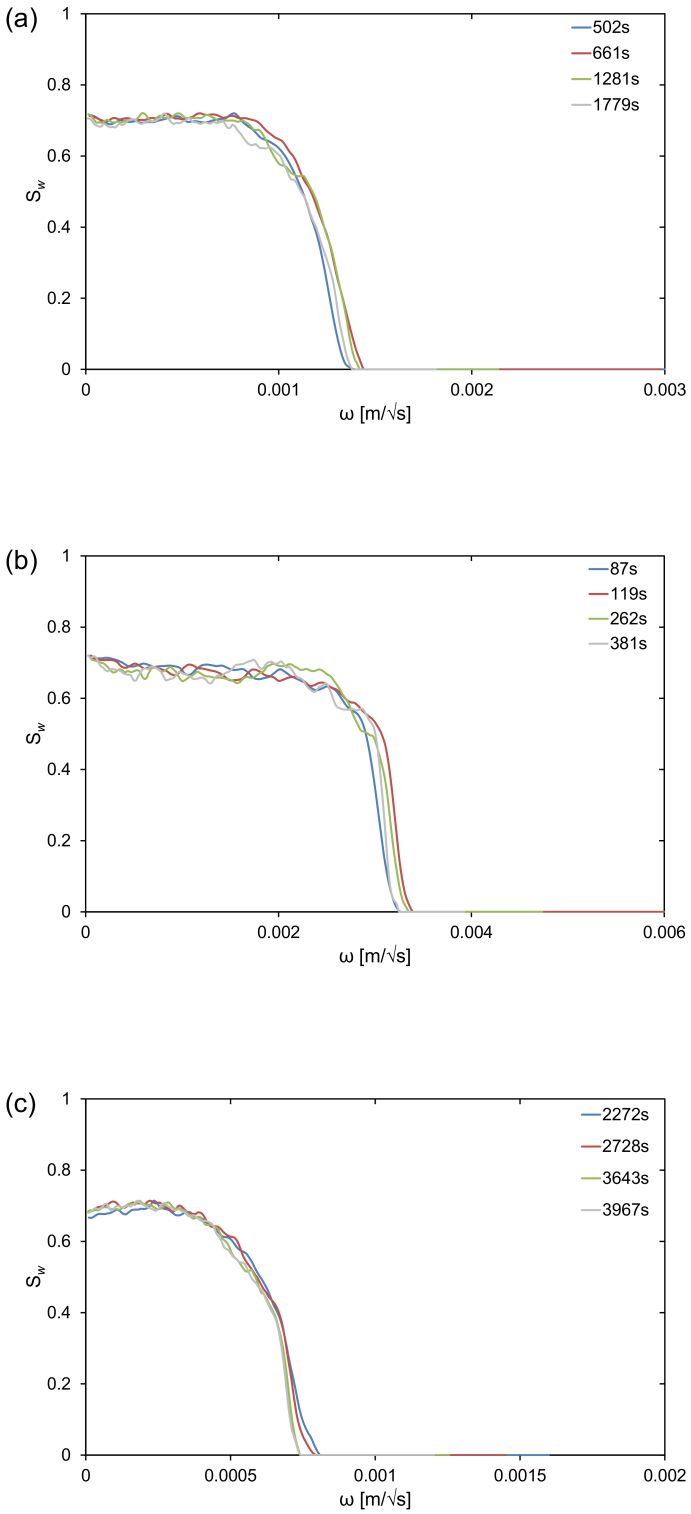

Figure 3.14. The water saturation as a function of $\omega(x/\sqrt{t})$ after re-processing Figure 3.12 for (a) Estaillades, (b) Ketton, and (c) Portland.

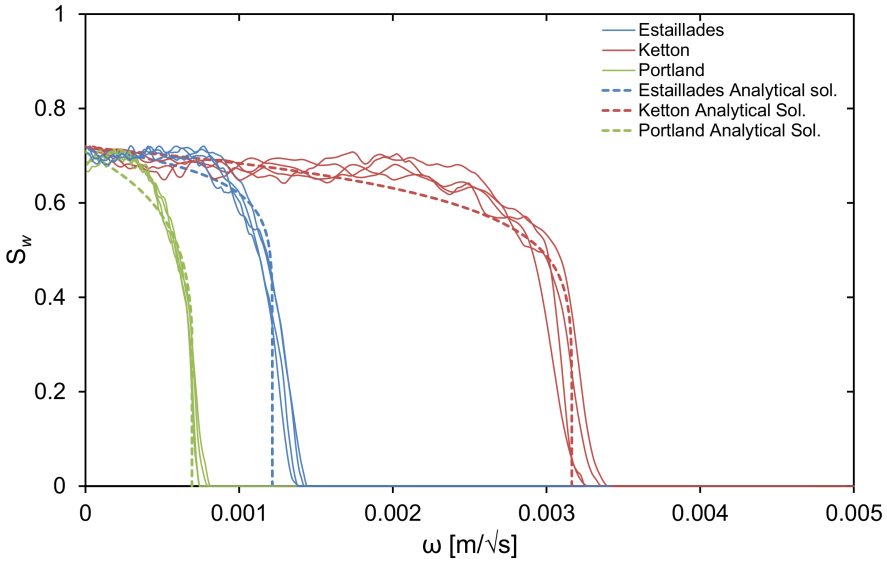

Figure 3.15. The water saturation as a function of $\omega(x/\sqrt{t})$ for the three rocks comparing the experimental results with analytical solutions.

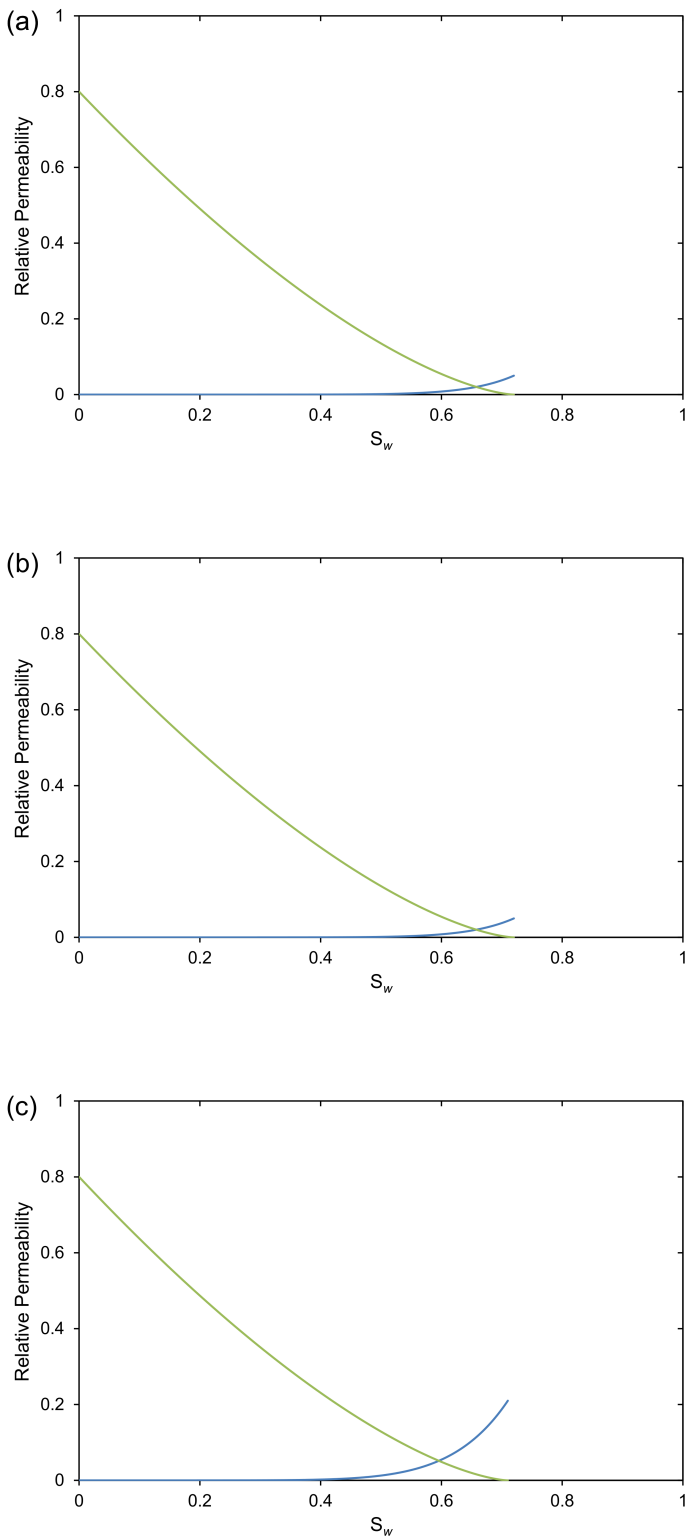

Figure 3.16. Relative permeabilities used to match the analytical solution with the experimental data in Figure 3.15 for (a) Estaillades, (b) Ketton, and (c) Portland.

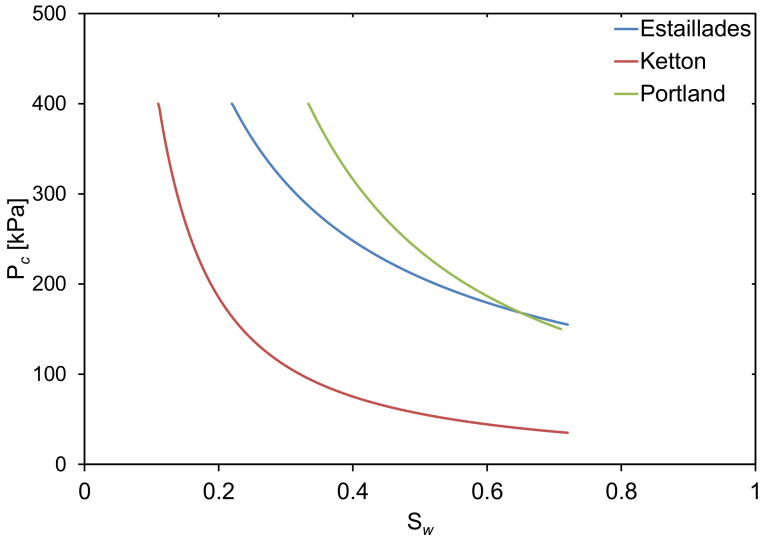

Figure 3.17. Capillary pressures used to match the analytical solution with the experimental data in Figure 3.15 for the three rocks.

Table 3.3. Input parameters used for the construction of the analytical solution to match the experimental data.

Input Parameter	Estaillades	Ketton	Portland
S_{wi}	0	0	0
S_{gr}	0.28	0.28	0.29
n	10	10	8
$k_{rw,max}$	0.05	0.05	0.21
m	1.5	1.5	1.5
$k_{rg,max}$	0.8	0.8	0.8
$Pc, entry$ [Pa]	110000	35000	150000
α	-1.5	-1.3	-1.3
Maximum P_c [Pa]	400000	400000	400000
μ_w [Pa. s]	0.001	0.001	0.001
μ_g [Pa. s]	0.000018	0.000018	0.000018
k [$\times$ 10^{-13} m^2]	2.1	23.5	0.0052
ϕ	0.276	0.207	0.221

3.5.3. Comparison of Mass Measurements and Saturation Imaging

We compare the volume imbibed from the mass imbibition experiments and the CT experiments, Figure 3.18. For this comparison, we use mass imbibition data for all the rocks, Figure 3.6. However, we select the end of early time of the shortest plug for each rock, then we truncate all the data higher than that time for all the lengths to achieve standard comparison. Due to the existence of dead volumes in the CT imaging experiment, an integrated volume of the water imbibed is not possible. Therefore, we

use the C value to calculate the volume imbibed as:

$$V = 2CA\sqrt{t} \tag{3.50}$$

where V is the volume imbibed [m^3], C is a parameter that quantifies the rock's ability to imbibe [$m/\sqrt{s}$], A is the area open to water flow [m^2], and $\sqrt{t}$ is the square root of time [$\sqrt{s}$].

The calculation of the volumes imbibed are based on the C values from the analytical solution: 1.1×10^{-4} $m/\sqrt{s}$, 2.1×10^{-4} $m/\sqrt{s}$, and 4.75×10^{-5} $m/\sqrt{s}$ for Estaillades, Ketton, and Portland respectively.

The mass imbibition and the CT experiments do not show agreement with Estaillades and Portland, where the imbibition rate is faster in the CT scanning experiment for Portland and shorter for Estaillades. Although the mass imbibition and CT experiments overlap, the C value in the CT experiments is much higher than the mass imbibition experiments. While it is simple to measure the mass imbibed, the CT imaging experiment is more reliable, less susceptible to early-time artefact and provides additional valuable information on the shape of the imbibition profile. As a result, this is the recommended technique for the analysis of SI.

From the definition of the Leverett J-function, Equation 1.5, and the non-linear capillary dispersion, Equation 3.14, we expect the the rate at which the mass is imbibed, indicated by the fitted parameter C, to scale as the square root of permeability, $\sqrt{k}$ as discussed previously. Figure 3.19 shows the C plotted as a function of $\sqrt{k}$ for the three rocks. Within each rock type, for samples with different permeability, we see an increasing trend in the CT experiments while the trend flattens out at higher permeabilities for the mass imbibition experiments. This indicates that mass imbibition experiments are unreliable and incompatible with the CT measurements because of the meniscus jump and hence we recommend CT with in-situ monitoring as a way forward.

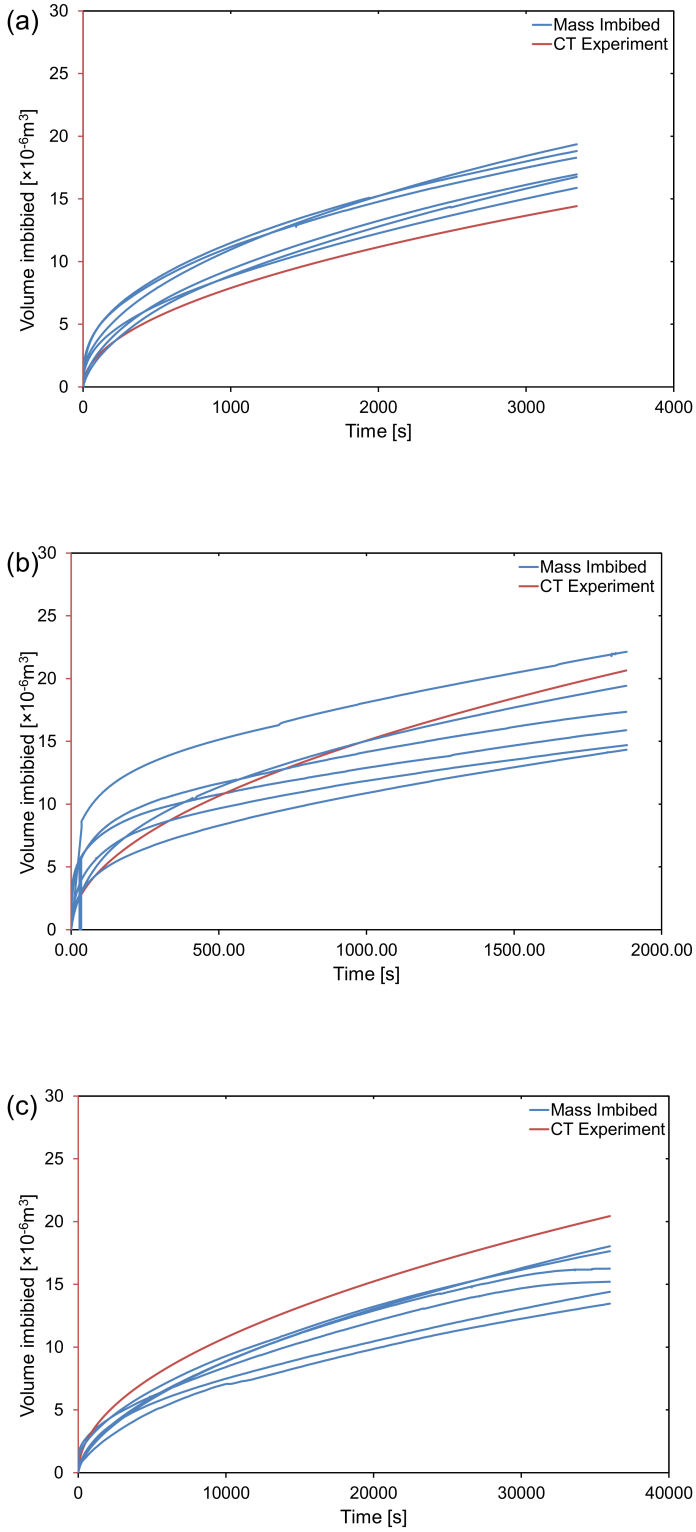

Figure 3.18. Volume imbibed as a function of time from the mass imbibition experiments Figure 3.6 and calculation of the volume imbibed based on the C values from the analytical solution for (a) Estaillades, (b) Ketton, and (c) Portland.

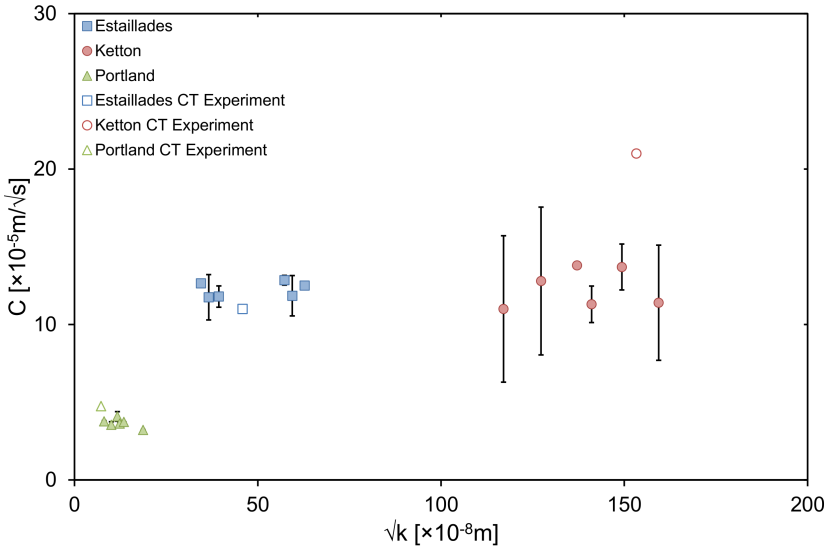

Figure 3.19. Relationship between C, giving the rate of imbibition, and the square root of permeability $\sqrt{k}$ for all our experiments.

3.5.4. Analytical Comparison of Co- and Counter-Current Imbibition

We are dealing with an air/brine fluid pair, with a very large viscosity ratio ($\mu_w/\mu_g \approx 560$). The difference between the co-current and counter-current analytical solution Equations 3.24 and 3.25 respectively, is the inclusion of the Buckley-Leverett fractional flow. In our system this term will be close to 0 since we have a very high viscosity ratio. Figure 3.20 shows the Buckley-Leverett fractional flow along with the co-current and counter-current fractional flows based on the matched relative permeability and capillary pressure Figures 3.16 and 3.17 respectively. We can see that the Buckley-Leverett fractional flow is close to 0 while the co-current and counter-current fractional flows are close to each other. Figure 3.21 shows the ω as a function of water saturation for both co-current and counter-current for the three rocks. The front for the co-current case is only slightly faster than the counter-current case indicting that the behaviour of co-current and counter-current showed be the same when dealing with air/brine fluid pair. This difference is something that could be tested experimentally in future work, ideally with fluids of more similar viscosity, such as oil and water.

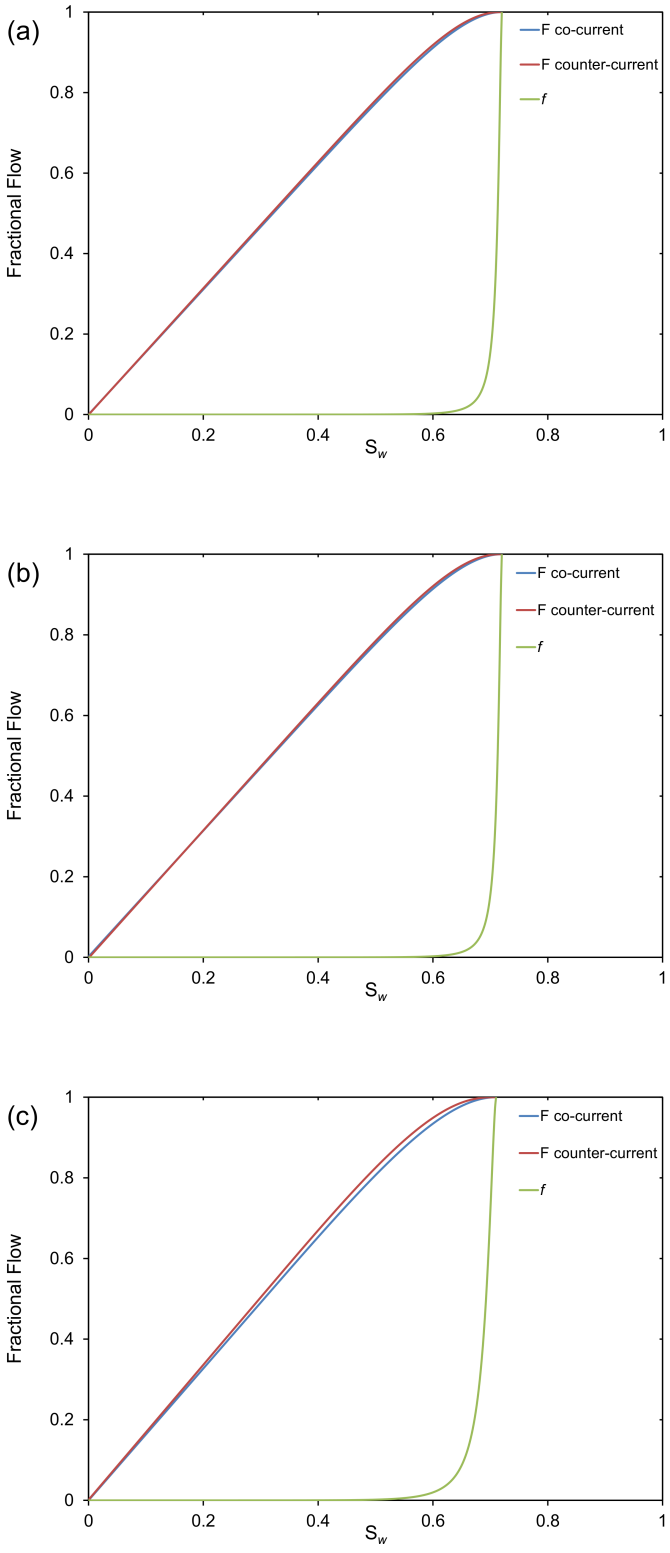

Figure 3.20. Buckley-Leverett, co-current, and counter-current fractional flows for (a) Estaillades, (b) Ketton, and (c) Portland, based on the matched relative permeability and capillary pressure data.

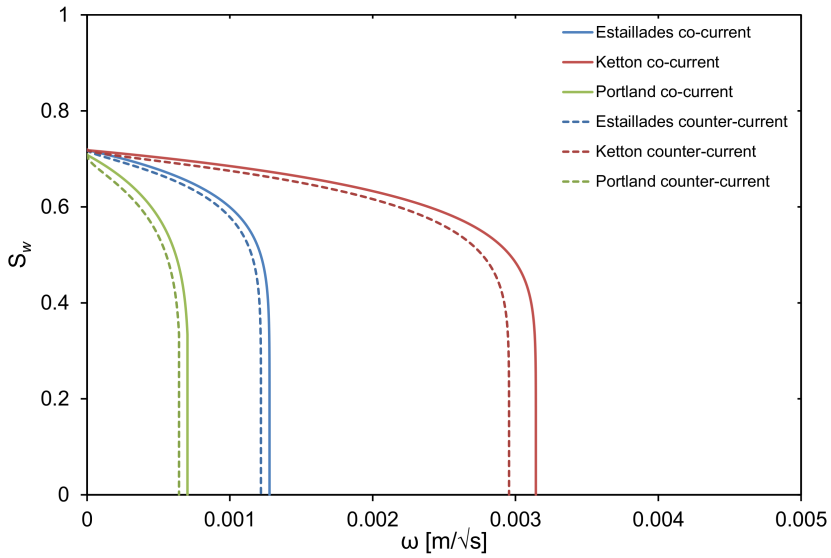

Figure 3.21. ω as a function of water saturation comparing the behaviour of co-current and counter-current flow based on the matched relative permeabilities and capillary pressures of the three rocks.

3.6. Conclusions

We have used the analytical solution for spontaneous imbibition derived by *Schmid et al.* 2011 and their derivation for the closed-form dimensionless time, *Schmid and Geiger* 2012, to compare to direct experimental measurements and have shown its current applications and discussed its potential future applications. We have shown how to obtain the constant C, which determines the imbibition rate, from a simple mass imbibition experiment which can be used to scale laboratory experiments to the field scale, and is also an important input parameter in the analytical solution. We show that regardless of the length of the core, the measured value of C appears to be constant.

CT spontaneous imbibition experiments can give us the saturation profile along the core's length which is comparable to the saturation profile shape derived by *Schmid and Geiger* 2012 for capillary dominated flow. At early time, before the imbibing water front reaches the end of the core, saturation profile is a function only of the distance divided by the square-root of time. This form is a function of imbibition relative permeabilities and capillary pressure. If we measure two of these three functions of saturation in the lab then we could find the other function by matching to the analytical solution, providing a robust determination of multiphase flow properties.

Future work could extend this preliminary study to mixed-wet systems, and, as mentioned above, to complement and constrain traditional core analysis measurements of relative permeability and capillary pressure.

4. Capillary Trapping and Oil Recovery

4.1. Introduction

We perform waterflood experiments at ambient conditions and elevated temperatures on the three carbonate rocks at water-wet and altered-wettability conditions. The rocks are 38 mm in diameter and 76 mm in length. We use 1.5 wt.% of cyclohexanepentanoic acid in n-decane to alter the wettability into a more oil-wet state. This organic acid is reported in the literature to be a fast way to alter the wettability of calcite into more oil-wet state at ambient conditions and it is commercially available [*Wu et al.*, 2008].

We use both the porous plate technique and the USS method to establish different initial oil saturations. We waterflood subsequently to find the residual oil saturation.

For the experiments conducted at elevated temperatures, we use a crude oil with a high asphaltenic content and high viscosity. We age at a temperature of 70°C to alter the wettability and establish the initial oil saturation. Again, we use the porous plate and USS methods to establish a wide range of initial oil saturations before waterflooding.

4.2. Experimental Procedure

4.2.1. Ambient Condition Waterflooding

Core and Brine Preparation

- Measure the dimensions and the mass of the dry core.
- Prepare brine of 5 wt.% NaCl and 1 wt. % KCl with a molality of 1.05 mol.kg^{-1}.
- Add smaller samples of the carbonate rock to the mixing of the brine to establish chemical equilibrium between the brine and rock and eliminate any further reaction with the rock.
- Mix the brine for 48 hours and leave it to equilibrate for 4 days as discussed in Chapter 3.
- After that, filter the brine using very fine filter papers.
- After preparing both the core and brine, insert the core into a Hassler cell and vacuum for 12 hours.

- In parallel, insert the brine into a vacuum chamber and vacuum for 3-5 hours and vacuum saturate the intended porous plate. This step saves time while saturating the core with brine (primary brine saturation) as the porous plate is very impermeable.

Figure 4.1 shows the experimental apparatus for the ambient conditions experiment.

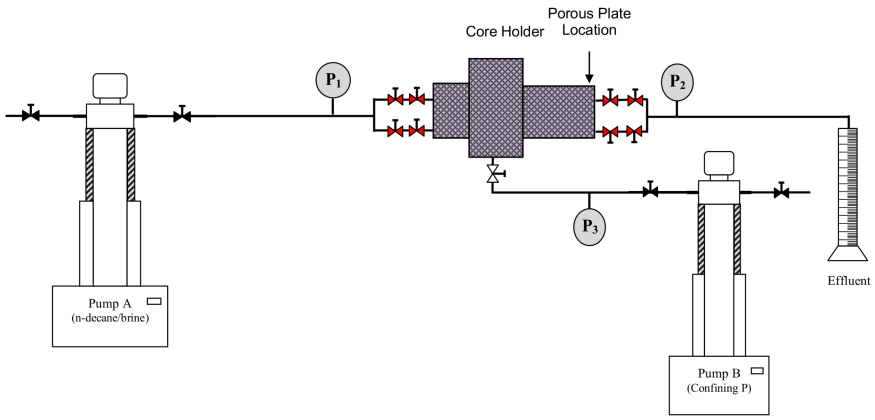

Figure 4.1. Schematic of the ambient conditions coreflood apparatus.

Water-wet Scenario

Brine Saturation

- Inject several pore volumes, PV, of degassed brine into the core at an average flow rate of 2 ml/min, using a Teledyne pump, ISCO 1000D or 500D, until no changes in the differential pressure readings due to any air being dissolved in brine are observed.
- Decrease the pore pressure slowly to atmospheric pressure and then decrease the confining pressure to atmospheric pressure as well.
- Extract the core and weigh it in a beaker filled with degassed brine using a balance with 0.001 g accuracy.
- Insert the core back into the Hassler cell and also insert the brine saturated porous plate in the downstream part of the core.
- To ensure a continuous flow between the core and the porous plate, insert a filter paper between them that will block any disintegrated particle from the core to enter the porous plate and hence block it.
- Inject 5 PV of degassed brine to make a continuous brine phase and also to dissolve any air that might have entered the core while extracting the core before.
- The injection scheme should be at a constant differential pressure mode and set

the pressure to be slightly lower than the porous plate's differential pressure. Since there are three different types of porous plates (1, 5, and 15 Bar; 1 Bar $\approx 10^5$ Pa), set the pressures accordingly.

- All the experiments can be performed with the 15 Bar porous plate; however, it will take a longer period of time to displace the brine through it as it is the least permeable but can sustain higher pressures. The other two porous plates are more permeable but they cannot sustain more than their intended pressures or they will let air through. For example, using a 5 Bar porous plate for a 4 Bar differential pressure will take less time to reach equilibrium than using a 15 Bar porous plate.
- After fully injecting the 5 PV, seal the core holder to start primary drainage.

Primary Drainage

- Inject n-decane (non-wetting phase, Sigma Aldrich, purity $\geq 99\%$) at a constant pressure from the upstream end. The porous plate will retain the n-decane and maintain a fixed brine pressure downstream. The difference between the upstream and the downstream pressures is the capillary pressure. The selection of the capillary pressure depends on the mercury capillary pressure data, Figure 2.2. In brief, select capillary pressures in the transition zone to give different initial oil saturations inside the core.
- Keep track of the differential pressure from the pressure transducers upstream and downstream, as well as the volume of n-decane injected from the pump and the amount of water produced.
- The drainage process ends when there is no further decrease in the volume of n-decane inside the pump is observed and no change in the volume of the brine effluent is detected. Normally, the drainage process takes from 3 days up to 20 days depending on the permeability of the rock and the capillary pressure selected. Higher permeability rocks take less time to reach capillary equilibrium since it is faster for the non-wetting phase to access the rock. Furthermore, low capillary pressures take less time to reach to capillary equilibrium as they access the larger, more permeable, portions of the rock.
- In order to drain the core with the USS method, follow the same procedure as before but do not insert the porous plate and instead inject the n-decane at a constant flow rate for several PVs until the differential pressure across the core becomes constant.

Spontaneous Water Imbibition

- Then, take the core out; however, first reduce the pore pressure and then the confining pressure to atmospheric pressure.

- Remove the core and weigh it and then insert it into an Amott cell, Figure 1.8 [*Amott*, 1959].
- Fill the base part of the Amott cell by one third of degassed brine.
- Seal the Amott cell and open the top part and keep injecting degassed brine until the volume reaches the full minus 1-2 ml.
- Monitor the spontaneous water imbibition until no further n-decane is produced at the top of the cell.
- Take the core out and weigh it and re-insert it back in the core holder for waterflooding.

Waterflooding (Forced Water Injection)

- Apply confining pressure and inject 5-10 PV of degassed brine until the residual oil saturation is reached. More precisely, this is the oil saturation remaining at the end of injection and may not be the true residual, reached after an infinite amount of waterflooding in systems with an altered wettability. This subtlety is discussed later. The injected flow rate is 0.1 ml/min which represents a capillary number of 3.0×10^{-8}, which is in the capillary-controlled regime [*Chatzis and Morrow*, 1984].
- Monitor the amount of n-decane produced after finishing the experiment to find the residual saturation. For more information on how to measure the initial and residual saturations, please refer to Appendix A.4.

Altered-Wettability Scenario

To alter the wettability of the rock at ambient conditions, we add 1.5 wt. % of cyclohexanepentanoic acid (Sigma Aldrich, purity = 98%) in n-decane which we refer to as fluid A. The procedure for the altered-wettability coreflooding experiments is exactly the same as the water-wet experiments discussed above; however, the only differences are that instead of injecting pure n-decane, we inject fluid A, place the altered core in the Amott cell for a duration of 30 days or more, and waterflood the core with 10 PV of brine.

We assume that this is sufficient to reach the residual oil saturation. We hypothesize that only those surfaces contacted by the initial oil saturation have an altered wettability. We are simply measuring the remaining oil saturation after this amount of water injection. In any event, this is much more water than injected overall in any field-scale waterflood.

The selected drainage capillary pressure ranges from 30-1200 kPa for all the rocks to cover a range of initial oil saturations.

We also notice that the addition of 1.5 wt. % of cyclohexanepentanoic acid in n-decane

to alter the wettability artificially without crude oil sometimes ages the porous plate to oil-wet conditions allowing oil production from the downstream end. These experiments are excluded in this study.

The waterflood starts at 0.1 ml/min for the first 2 PV and then we increase the flow rate gradually to reach 30 ml/min for Estaillades and Ketton. However, for Portland we inject up to a rate of 0.35 ml/min since it has a very low permeability and increasing the flow rate will build up the pressure too high to be able to confine the fluids easily. We keep increasing the flow rate because *Masalmeh* 2012 indicated that injecting many PVs at low rate does not lead to better estimation of S_{or} for oil-wet or mixed-wet rocks; the only way to get to S_{or} is to increase the rate to overcome the capillary end effect. This is consistent with studies employing a constant flow rate, where 10 PV is insufficient to reach the residual oil saturation in altered-wettability rocks [*Salathiel*, 1973, *Jadhunandan and Morrow*, 1995, *Tanino and Blunt*, 2013].

The fluid properties used in this study are shown in Table 4.1. We measure the n-decane/brine and Fluid A/brine interfacial tensions and the intrinsic contact angles on smooth calcite surfaces by using Ramé-Hart model 590 device; for the detailed procedure for measuring these properties please refer to Appendix A.5 and A. 6 for interfacial tension and contact angle respectively. It is worth mentioning that we submerge the calcite crystals in Fluid A to alter the surface wettability of the calcite and then we measure the contact angle. In addition, we measure the density and viscosity of the fluids at 20°C using Anton Paar DMA5000 M and Rheotek U-tube viscometer respectively. Also, we calculate the total acid number (TAN) in Fluid A, which is a measurement of acidity that is determined by the amount of potassium hydroxide in milligrams that is needed to neutralise the acids in one gram of oil [*Jingyan et al.*, 2012, *Buckley and Fan*, 2007]. *Buckley* 2001 indicated that calcite surfaces highly adsorb organic acids, while quartz surfaces adsorb organic bases, which might explain the reason behind the strong wettability alteration.

Table 4.1. Properties of the oil phase fluids used in this study at ambient conditions.

Fluid	ρ [kg/m^3]	μ [mPa s]	TAN [mg KOH/g oil]	σ [mN/m]	θ_I [°]
n-decane	728.8±0.02	0.92	-	53.8±0.1	37.9±2
A	731.5±0.02	0.91	4.57	19.8±0.3	130±3

4.2.2. High Temperature Waterflooding

Core and Fluid Preparation

- Vacuum the core for 12 hours while the oven which contains the cell heats to 70°C, Figure 4.2.

- Prepare the brine of 5 wt.% NaCl and 1 wt.% KCl with a molality of 1.05 mol.kg^{-1} and mix it with smaller pieces of each rock. This mixing happens at 70°C; smaller amounts of $CaCO_3$ and Magnesium carbonate ($MgCO_3$) have been shown to dissolve at higher temperatures [*El-Maghraby et al.*, 2012].
- Vacuum the brine for 12 hours in a vacuum oven at 70°C. The density of brine at 70°C is reported as 1,018 kg/m^3 [*Al Ghafri et al.*, 2012].
- Vacuum saturate both the core and the porous plate inside the vacuum oven for 12 hours and then weigh the core before inserting it into the Hassler cell.
- Inject 5 PV of heated brine into the core to dissolve any air that might have entered the core. All the pumps are heated to 70°C using a water bath and heating jackets and the tubes connected to the cell from outside the oven are covered with heating insulation, Figure 4.2.
- Fill the pump with crude oil and leave it for 6 hours before starting the injection in order for the crude oil properties to settle at 70°C.

Table 4.2 shows the the composition of the crude oil and Table 4.3 shows the properties of the crude oil and n-decane at 70°C; these measurements were provided by Shell Rijswijk, Netherlands, along with the crude oil.

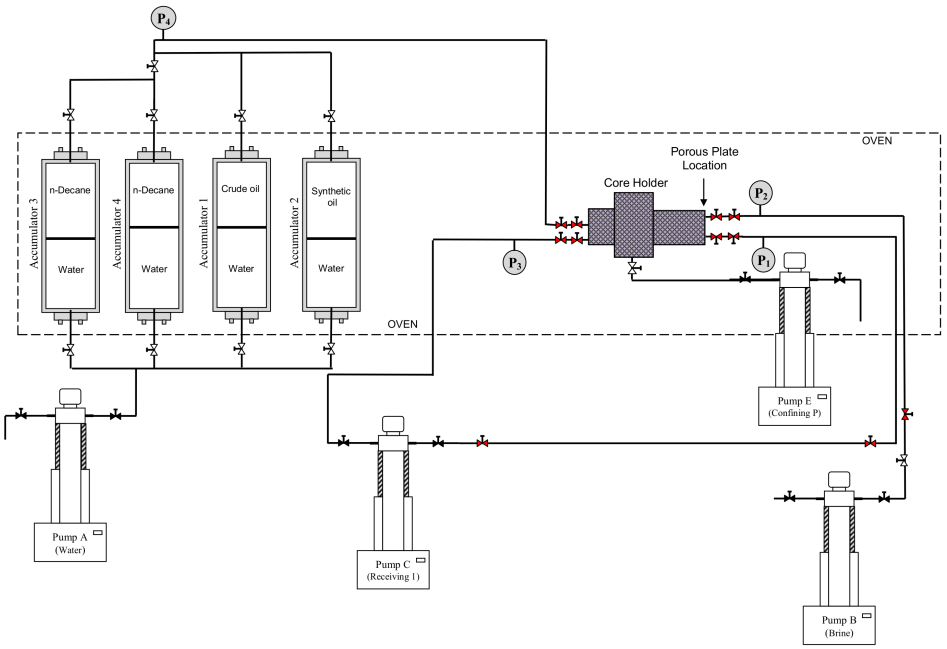

Figure 4.2. Schematic of the elevated temperatures coreflood experiment.

Table 4.2. Composition and properties of the crude oil used in this study.

TBN	TAN	API°	SARA Analysis [wt%]			
[mg KOH/g oil]	[mg KOH/g oil]	[API]	Saturates	Aromatics	Resins	Asphaltenes
2.02	0.35	27.8	31.57	50.69	14.29	3.46

Table 4.3. Fluid properties of the n-decane and the crude oil used in this study at 70°C.

Fluid	ρ [kg/m^3]	μ [mPa s]	σ [mN/m]	θ_I [°]	θ_A [°]	θ_R [°]
n-decane	691[a]	0.49[a]	40.0[a]	-	-	-
crude oil	856	6.51	27.2[b]	100[b]	81[b]	109[b]

[a]For μ and ρ of n-decane and σ measured with n-decane/synthetic brine (consisting of 10000 mg/L NaCl, 70 mg/L $MgCl_2.6H_2O$, and 200 mg/L $CaCl_2.2H_2O$) fluid pair, all these measurements were performed at 70°C [*Humphry et al.*, 2013].
[b]Measured on a smooth surface with the same same crude oil and with brine of 4.39 mol.kg^{-1} molality NaCl at 50°C and ambient pressure [*Li et al.*, 2015]. Note that the measurement was conducted using an oil droplet on a smooth calcite surface through brine thus $\theta_R > \theta_A$.

Water-Wet Scenario

We use the same water-wet trapping data as the ambient conditions data as we do not expect to see significant differences between the results at ambient conditions and 70°C [*Pentland et al.*, 2010, 2011].

Altered-Wettability Scenario

Primary Drainage

- When the system is in thermal equilibrium, inject the crude oil from the upstream side of the Hassler cell and collect the brine effluent outside the oven at ambient conditions to avoid evaporation inside the oven. Depending on the capillary pressure injected, the time of this experiment varies. Since the brine effluent is outside the oven, careful monitoring of the amount of brine displaced is possible.
- When no changes in the volumes of the injection pump and the effluent are observed, we know that the drainage process ends.
- Take the core out and weigh it and place it in a container filled with the same crude oil for 40 days for further ageing.
- After that, continuously inject 5 PV of deahydroanphthalene (decalin) and followed by 5 PV of n-decane. Inject the decalin in order to prevent any mixing of n-decane with crude oil which may lead to asphaltene deposition [*Vincent and Kilpatrick*, 2007, *Tie and Morrow*, 2005, *Buckley et al.*, 2006, *Fernø et al.*, 2010]. In addition, using n-decane will assess the stability of the wettability alteration.

- Extract the core and place it in the Amott cell.
- For the USS method, repeat the same procedure but without the porous plate and inject 5 PV of crude oil at a constant flow rate. Following that, inject 5 PV of decalin and after that 5 PV of n-decane. This method is also referred to as dynamic wettability alteration.

Spontaneous Water Imbibition

- Insert the core into a half full Amott cell with 70°C degassed brine.
- Top the additional volume of brine from the top of the cell until reaching the full volume minus 2-3 ml.
- Seal the Amott cell but not fully and place it into the oven at the same temperature of 70°C.
- After 30 minutes, seal the cell perfectly and that step is to avoid any fluid expansion which may lead to pressurisation of the cell, and leave it for 30 days.
- Monitor the cell, until no further volume of n-decane is produced.
- Recored the final volume of n-decane produced and the weight of the core after spontaneous water imbibition.

Waterflooding

- Place the core again in the Hassler Cell.
- Inject up to 10 PV of degassed brine at 70°C starting from a flow rate of 0.1 ml/min and which gradually increase until reaching to a high flow rate compared to the permeability of the rock as discussed for the ambient condition experiments.
- Monitor the volume of n-decane in the effluent and weigh the core after the injection of the brine for the residual oil saturation measurement.

4.3. Results and Discussion

4.3.1. Amott Wettability Indices

Ambient Conditions

For the water-wet systems, we see significant recovery from spontaneous water imbibition; the Amott water index, $I_w > 0.9$ for all the rocks, Table 4.4. For the altered-wettability systems, spontaneous water imbibition produces $I_w = 0$ for Estaillades and Portland. This might indicate that the systems are intermediate-wet due to the rocks not imbibing any water, as discussed in Chapter 1. However, for Ketton, we have $I_w > 0.9$ indicating no sign of wettability alteration. In Ketton, as we show later, we do not

invade the micro-porosity with wettability-altering agent (the oil phase). As a result, we can only saturate the large macro-pores at relatively low capillary pressures with little wettability alteration.

For I_o, we do not see any oil imbibition. A similar behaviour have been noticed by *Fernø et al.* 2010 where no oil imbibition occurred when chalk limestones were aged by crude oil despite a low I_w.

Table 4.4. Detailed summary of the petrophysical properties, capillary trapping data, and Amott water index for the ambient conditions waterflooding experiments. I_o is zero for all the rocks. The data above the dashed line are water-wet data while the ones below it are altered-wettability data. The S_{oi} and S_{or} data are the average of the mass and volume balance methods and the error bars are the standard deviation of these measurements.

Core Label	D [mm]	L [mm]	ϕ [%]	k [m^2]	S_{oi}	S_{or}	I_w
E7	37.8	76.51	26.4	2.07×10^{-13}	0.68±0.02	0.34±0.007	0.91
E8	37.88	76.28	27.3	1.69×10^{-13}	0.59±0.04	0.32±0.04	0.96
E9	37.77	76.4	27.8	2.58×10^{-13}	0.53±0.08	0.26±0.03	0.95
E10	37.66	75.81	28.0	2.96×10^{-13}	0.78±0.025	0.45±0.025	0.99
E11	37.82	76.63	26.2	1.94×10^{-13}	0.95±0.045	0.43±0.01	0.96
E12	37.75	76.08	27.2	1.77×10^{-13}	0.86±0.04	0.1±0.05	0
E13	37.79	76.29	27.3	2.03×10^{-13}	0.94±0.05	0.27±0.05	0
E14	37.87	76.22	28.0	2.18×10^{-13}	0.6±0.025	0.22±0.03	0
E15	37.65	76.24	27.9	3.26×10^{-13}	0.67±0.07	0.12±0.02	0
E16[a]	37.73	76.39	26.8	1.22×10^{-13}	0.58±0.025	0.33±0.04	0
K7	37.74	76.22	20.2	1.38×10^{-12}	0.68±0.06	0.33±0.05	0.93
K8[a]	37.87	75.29	22.0	1.07×10^{-12}	0.48±0.08	0.21±0.07	0.95
K9	37.87	75.29	22.0	1.07×10^{-12}	0.61±0.09	0.25±0.08	0.91
K10[a]	37.9	76.48	21.9	1.28×10^{-12}	0.64±0.05	0.33±0.05	0.93
K11	37.9	76.28	22.0	2.1×10^{-12}	0.36±0.05	0.17±0.05	0.92
K12	37.7	76.23	22.6	3.55×10^{-12}	0.59±0.05	0.3±0.05	0.95
P7	37.85	76.38	22.8	5.24×10^{-15}	0.27±0.03	0.19±0.03	0.9
P8	37.84	76.19	19.7	3.2×10^{-15}	0.4±0.02	0.3±0.02	0.92
P9[a]	37.95	76.35	19.8	1.9×10^{-15}	0.56±0.03	0.39±0.03	0.93
P10[a]	37.95	76.25	18.0	1.8×10^{-15}	0.68±0.03	0.44±0.03	0.95
P11	37.89	76.28	18.9	7.2×10^{-15}	0.49±0.09	0.27±0.1	0
P12	37.81	76.35	18.6	4.17×10^{-15}	0.25±0.03	0.16±0.05	0
P13	37.9	76.25	17.0	1.3×10^{-14}	0.38±0.03	0.18±0.06	0
P14[a]	37.92	76.35	21.0	6.2×10^{-15}	0.38±0.03	0.21±0.03	0

[a]Measured using the USS method.

Elevated Temperatures

For spontaneous water imbibition we see $0.07 > I_w > 0.17$ for Estaillades and Portland, Table 4.5. Ketton shows again $I_w > 0.9$ indicating no sign of wettability alteration. Since the results here showed more recovery form spontaneous imbibition that might indicates that the crude oil ageing is weaker than the organic acid, leaving some portions of the pore space water-wet.

Overall, for these rocks and the two wettability-altering agents studied (crude oil and organic acid) the degree of wettability alteration is modest. We study here systems that are more intermediate-wet with little or no spontaneous imbibition of either water or oil, indicating intrinsic local contact angles of around 90°.

Table 4.5. Summary of the petrophysical properties, capillary trapping data, and Amott water index for the high temperatures waterflooding experiments for altered-wettability samples. Again, I_o is zero for all the rocks. The S_{oi} and S_{or} data are the average of the mass and volume balance methods and the error bars are the standard deviation of these measurements.

Core Label	D [mm]	L [mm]	ϕ [%]	k [m^2]	S_{oi}	S_{or}	I_w
E17	37.65	76.52	26.2	2.25×10^{-13}	0.89±0.05	0.32±0.1	0.12
E18	37.75	76.26	27.6	1.69×10^{-13}	0.65±0.08	0.19±0.12	0.15
E19[a]	37.65	76.42	28.4	2.06×10^{-13}	0.8±0.05	0.26±0.08	0.07
K13[a]	37.9	76.48	21.8	1.54×10^{-12}	0.6±0.02	0.33±0.05	0.9
K14	37.9	76.28	22.0	2.6×10^{-12}	0.38±0.05	0.18±0.07	0.92
P15	37.66	76.42	18.5	2.47×10^{-15}	0.83±0.04	0.47±0.05	0.13
P16	37.84	76.09	20.9	9.9×10^{-15}	0.29±0.04	0.12±0.09	0.11
P17	37.73	76.38	19.4	3.57×10^{-15}	0.83±0.06	0.38±0.088	0.09
P18[a]	37.89	76.21	19.2	5.77×10^{-15}	0.61±0.035	0.25±0.035	0.17

[a]Measured using the USS method.

4.3.2. Leverett J-Function and Oil Accessibility

Ambient Conditions

We compute the Leverett J-function, Equation 1.5, for the ambient condition experiments from the measured injection pressure of oil during the primary drainage step using ϕ and k from Table 4.4 and σ of 53.8 mN/m for n-decane/brine system and 19.8 mN/m for fluid A/brine system, and θ of 37.9° for the two cases. We compare the data to the Leverett J-function of the measured MICP data from Figure 2.2.

Table 4.6 lists the capillary pressure data while Figure 4.3 shows the computed Leverett J-function for the three carbonates. The figure indicates that after accounting the contact angle and interfacial tension, the drainage behaviour of n-decane is similar to mercury to within experimental error for water-wet data. For the altered-wettability

samples, we observe a higher Leverett-J function compared to the water-wet state. This can be attributed to the uncertainty in the interfacial tension and assignment of the contact angle.

Mercury injection curves for Estaillades and Ketton indicate a bi-modal pore size distribution (the two regions of relatively low slope on the figure), with a connected macro-porous inter-granular porosity, and intra-granular micro-porosity that is only accessed at high capillary pressures.

For Estaillades and Portland at high initial oil saturations, the oil will access the micro-porosity Figures 4.3a and 4.3c respectively. However, for Ketton, Figure 4.3b, even with high capillary pressure the oil was not able to access the micro-pore which explains the reason behind the weak wettability alteration in Ketton. Therefore, higher capillary pressures are required to break the thin water films protecting the pore walls from oil [*Kovscek et al.*, 1993].

Table 4.6. Drainage capillary pressure data for all the rocks at ambient conditions. We calculate the corresponding r_p of each capillary pressure from Equation 1.6.

Core Label	P_c [kPa]	S_w	r_p [μm]	Oil Invasion (macro/micro)
E7	203	0.32±0.02	0.4	micro
E8	71	0.4±0.04	1.2	macro
E9	94	0.47±0.08	0.9	macro
E10	827	0.22±0.025	0.1	macro
E11	1209	0.05±0.045	0.07	micro
E12	827	0.14±0.04	0.03	micro
E13	1172	0.06±0.05	0.02	micro
E14	207	0.4±0.025	0.12	micro
E15	483	0.33±0.07	0.05	micro
K9	483	0.39±0.09	0.18	micro
K11	34	0.64±0.05	0.73	macro
K12	483	0.41±0.05	0.05	micro
P7	69	0.73±0.03	1.23	macro
P8	483	0.6±0.02	0.18	micro
P11	827	0.51±0.09	0.03	micro
P12	69	0.75±0.03	0.37	micro
P13	483	0.62±0.03	0.05	micro

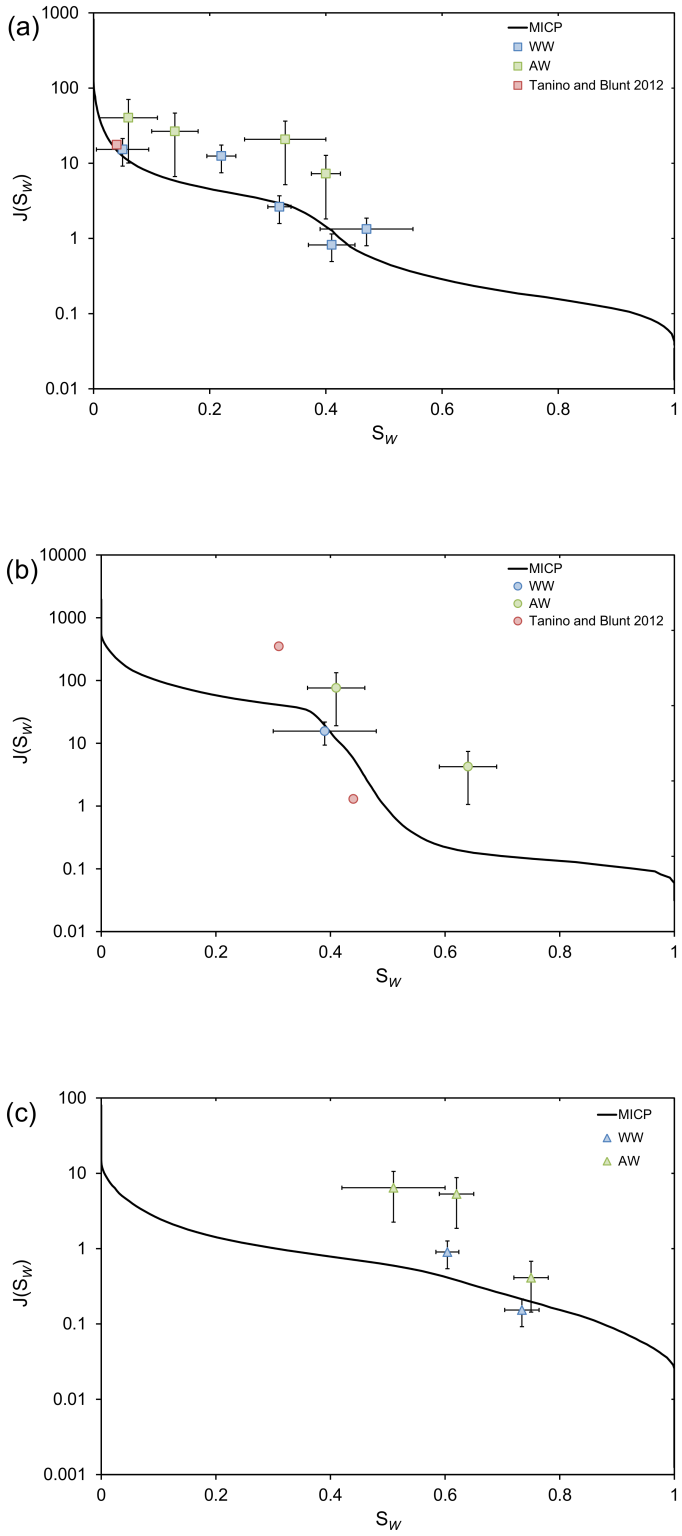

Figure 4.3. Leverett J-function, Equation 1.5, for ambient conditions experiments and external MICP data for (a) Estaillades, (b) Ketton, and (c) Portland core samples. In addition, we include water-wet literature data for Estaillades and Ketton from *Tanino and Blunt* 2012.

Elevated Temperatures

Similarly for elevated temperatures, we compute the Leverett J-function to compare the MICP data with the experimental data. In this case, we use ϕ and k from Table 4.5 and σ of 27.2 mN/m and θ of 37.9°. A list of the capillary pressure data at elevated temperatures is given in Table 4.7.

Similar to the ambient conditions, for both Estaillades and Portland Figures 4.4a and 4.4c respectively. We can access the micro-pores at the selected capillary pressure. However, for Ketton, Figure 4.4c, the induced capillary pressure is not sufficient to access the micro-pores which explains the weak wettability alteration as well. Over 50% of Ketton's porosity is considered to be micro–see Chapter 2–which prevents the oil to be in contact with more of the surface of the rock.

Overall, pore structure is an important feature to understand the wetting behaviour. Rocks with high fractions of micro-porosity will require higher capillary pressures to break the water films and thus the oil will be able to coat on the surface.

Table 4.7. Drainage capillary pressure data for all the rocks at elevated temperatures. We calculate the corresponding r_p of each capillary pressure from Equation 1.6.

Core Label	P_c [kPa]	S_w	r_p [μm]	Oil Invasion (macro/micro)
E17	34	0.34±0.08	0.9	macro
E18	482	0.1±0.05	0.06	micro
K14	48	0.64±0.05	0.65	macro
P15	414	0.17±0.04	0.08	micro
P16	34	0.71±0.04	0.9	macro
P17	827	0.17±0.06	0.04	micro

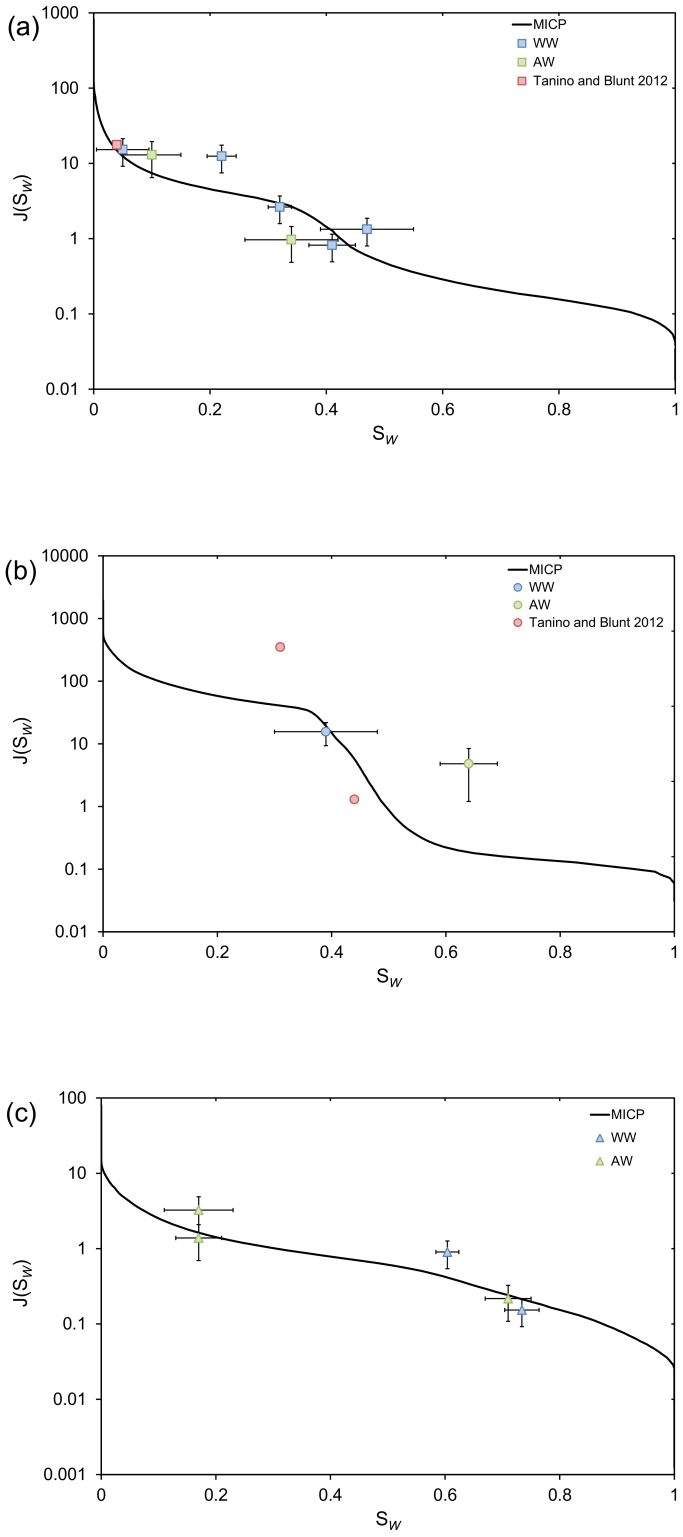

Figure 4.4. Leverett J-function, Equation 1.5, for elevated temperatures experiments and external MICP data for (a) Estaillades, (b) Ketton, and (c) Portland core samples. In addition, we include water-wet literature data for Estaillades and Ketton from *Tanino and Blunt* 2012.

4.3.3. Recap on Wettability and Contact Angle

Before presenting the waterflood results, we will review the measurements of wettability, compare with the measured contact angles and anticipate the likely behaviour of the systems we study.

Firstly, there is no routine method to measure the distribution of contact angle inside the rocks, although this is a topic of active research (see, for instance, [*Andrew et al.*, 2014]). Instead, we need to enter the likely contact angles from measurements on smooth surfaces and inherit macroscopic characterisation, such as the Amott wettability indices.

For Ketton, we see little sign of wettability alteration: during primary drainage, oil only invades the large macro-pores. This appears to protect the solid surface from deposition of acid and other surface-active components of the oil. Hence for Ketton we expect water-wet type behaviour in all cases: significant trapping, a monotonic trapping curve and little or no recovery after water breakthrough.

Estaillades and Portland both do experience a wettability change. Using the organic acid (ambient conditions) the intrinsic contact angle measured on a smooth surface is 130°, Table 4.1. This suggests oil-wet conditions, yet no sample spontaneously imbibes oil. This implies that, like Ketton, uninvaded micro-porosity may protected some surfaces weakening the wettability change, where $\theta_R < 90°$. However, because of contact angle hysteresis, the behaviour for water imbibition is indicative of $\theta_A > 90°$ since $I_w = 0$. Portland has more micro-porosity than Estaillades (see Chapter 2): since water-filled micro-porosity in Ketton serves to weaken the wettability trend, we expect Portland to display less oil-wet behaviour than Esaillades. Portland may display intermediate-wet characterisation, while Estaillades appears to be oil-wet.

With crude oil we see $\theta_R = 109°$, $\theta_I = 100°$, and $\theta_A = 81°$ measured through the brine (Table 4.3). This characteristic is of intermediate-wet surfaces with no imbibition of either oil or water. In Estaillades and Portland we do see a small amount of water imbibition, indicating some protected water-wet pores, but overall we expect intermediate-wet waterflood properties since wettability alteration is modest, with a monotonic trapping curve and some post-breakthrough recovery, but less trapping than a water-wet system.

4.3.4. Trapping Curves and Waterflood Recovery

Organic Acid

Figure 4.5 shows the water-wet and altered-wettability trapping curve for the three rocks, showing the remaining oil saturation after 10 PV of waterflooding as a function of initial oil saturation. For the water-wet systems, we see a monotonic increase in the trapping curve for all the rocks as we expected.

For the altered-wettability systems for Ketton, Figure 4.5b, we see a monotonic increase in the trapping curve with no further recovery beyond the first PV injected, as we expected.

For Estaillades, Figure 4.5a, we notice an unexpected trend in remaining oil saturation with initial saturation with three different regimes. First, we see most trapping for S_{oi}= 0.58. Second, we see a decrease in the remaining oil saturation for 0.58< S_{oi} ≤0.86, this can be explained by the stability of oil layers discussed in more detail later. Third, we see an increase again for $S_{oi} > 0.86$, this can be explained by trapping of oil in micro-porosity. This complex trend has been observed previously by *Salathiel* 1973, *Tanino and Blunt* 2013 in oil-wet and mixed-wet rocks.

For Portland, Figure 4.5c, we observe intermediate behaviour between Estaillades and Ketton where we see a monotonic increase in the trapping curve but with slightly higher recovery, less trapping, than the water-wet case. A similar trend of a monotonic increase in the trapping curve in altered wettability rocks have been observed by *Karabakal and Bagci* 2004, *Nono et al.* 2014. This can be explained with the high fraction of micro to macro-porosity in Portland. Portland has the highest fraction of micro-porosity, see Chapter 2, compared to the other rocks. However, these micro-pores are bigger than Ketton's micro-pores which will make it easier for the oil to coat the surface compared to Ketton. Still, with the selected capillary pressures, not all the pores have been contacted with oil, protecting the surfaces from a strong wettability alteration.

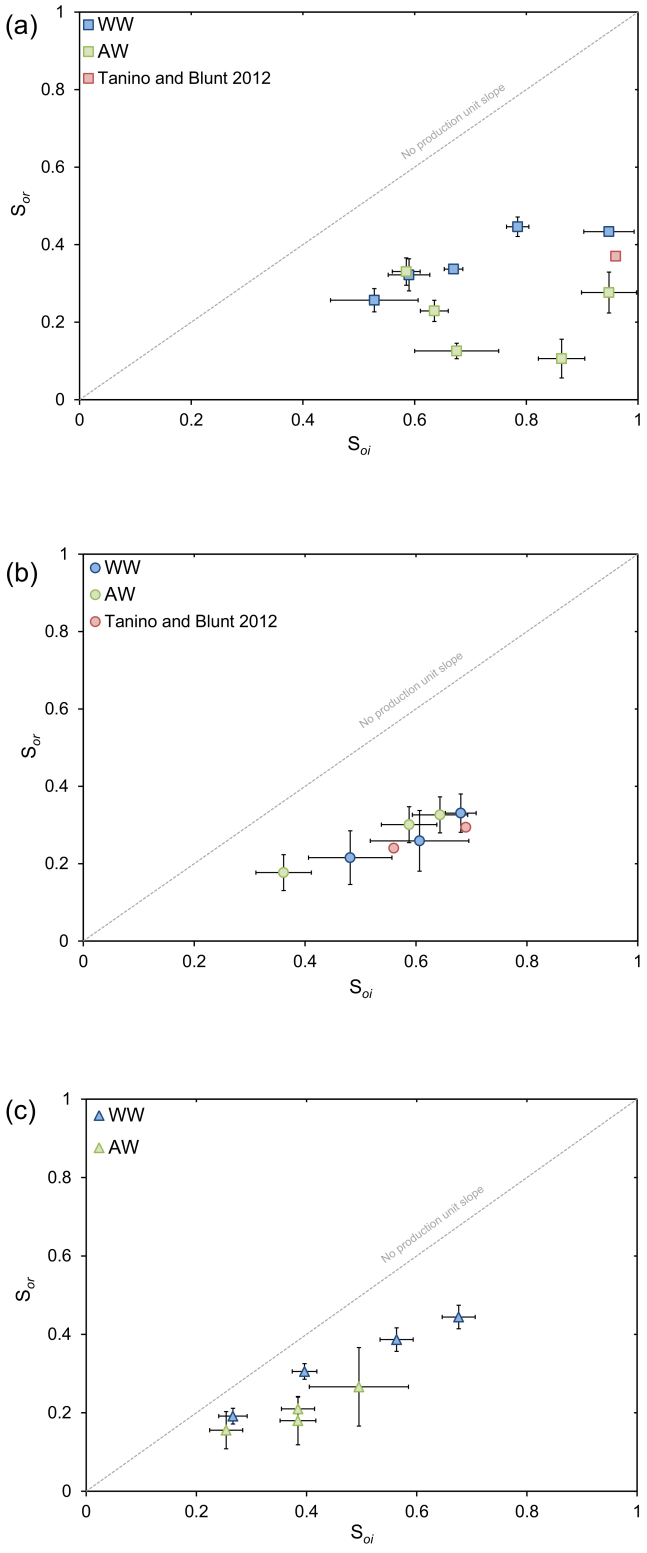

Figure 4.5. Remaining oil saturation as a function of initial oil saturation trapping curve at ambient conditions for water-wet and altered-wettability for (a) Estaillades, (b) Ketton, and (c) Portland core samples. The data plotted represent an average value of mass balance and volume balance while the error bars represent the standard deviation. In addition, we include water-wet literature data for Estaillades and Ketton from *Tanino and Blunt* 2012.

Crude Oil

The results using crude oil are illustrated in Figure 4.6. For the altered-wettability rocks, we see a monotonic increasing trend but with higher recovery than the water-wet case for Estaillades and Portland.

For Ketton, we see no sign of wettability alteration and similar trapping to the water-wet cases.

Overal, these results are indicative of intermediate-wet behaviour with less trapping than for water-wet rocks.

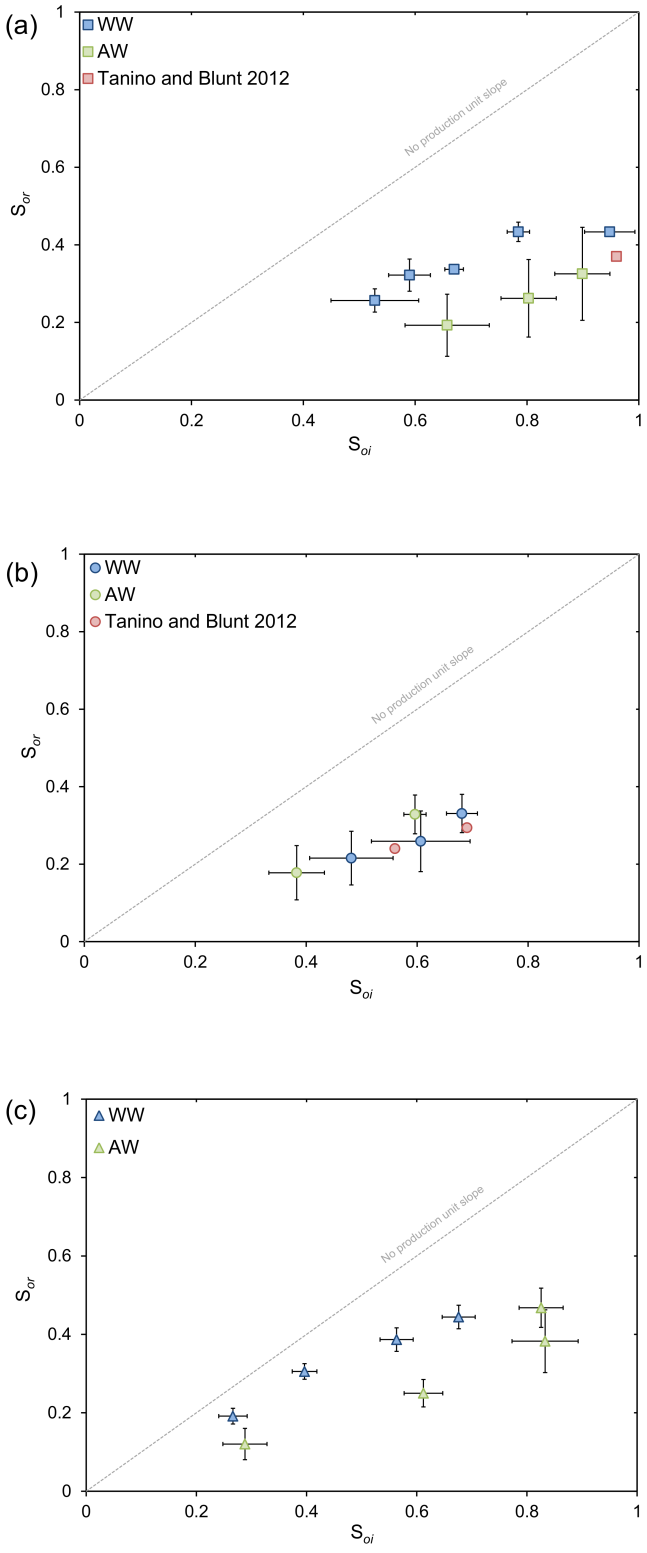

Figure 4.6. Remaining oil saturation as a function of initial oil saturation trapping curve at elevated temperatures for water-wet and altered-wettability for (a) Estaillades, (b) Ketton, and (c) Portland core samples. The data plotted represent an average value of mass balance and volume balance while the error bars represent the standard deviation. In addition, we include water-wet literature data for Estaillades and Ketton from *Tanino and Blunt* 2012.

4.3.5. Oil Recovery by Waterflooding

We show the remaining oil saturation as a function of brine pore volumes injected at ambient conditions, Figure 4.7, and at elevated temperatures, Figure 4.8. We can see that for the water-wet cases, we achieve the residual saturation from the first pore volume with no further reduction in the residual oil saturation as the waterflood is extended.

However, for the altered-wettability cases, we see significant recovery from the first pore volume but with further reduced recovery as the pore volume increases. The first three pore volumes have the most significant recovery with slower recovery later.

Ketton, shows water-wet behaviour in all cases, as expected.

With crude oil, Portland and Estaillades show intermediate-wet behaviour: while there is some recovery post-breakthrough, this can be modest with in all cases a monotonic increase in remaining oil saturation with the initial value for all the PV injected. Portland displays similar behaviour with organic acid.

The only oil-wet behaviour is shown for Estaillades with organic acid as the wettability agent. Here we see a sharp decrease in oil saturation with PV injected, and a crossing of the curves, such that for given amount of water injected a higher S_{oi} gives lower remaining S_o. This behaviour has been observed by *Jadhunandan and Morrow* 1995 and will be explained in the next section.

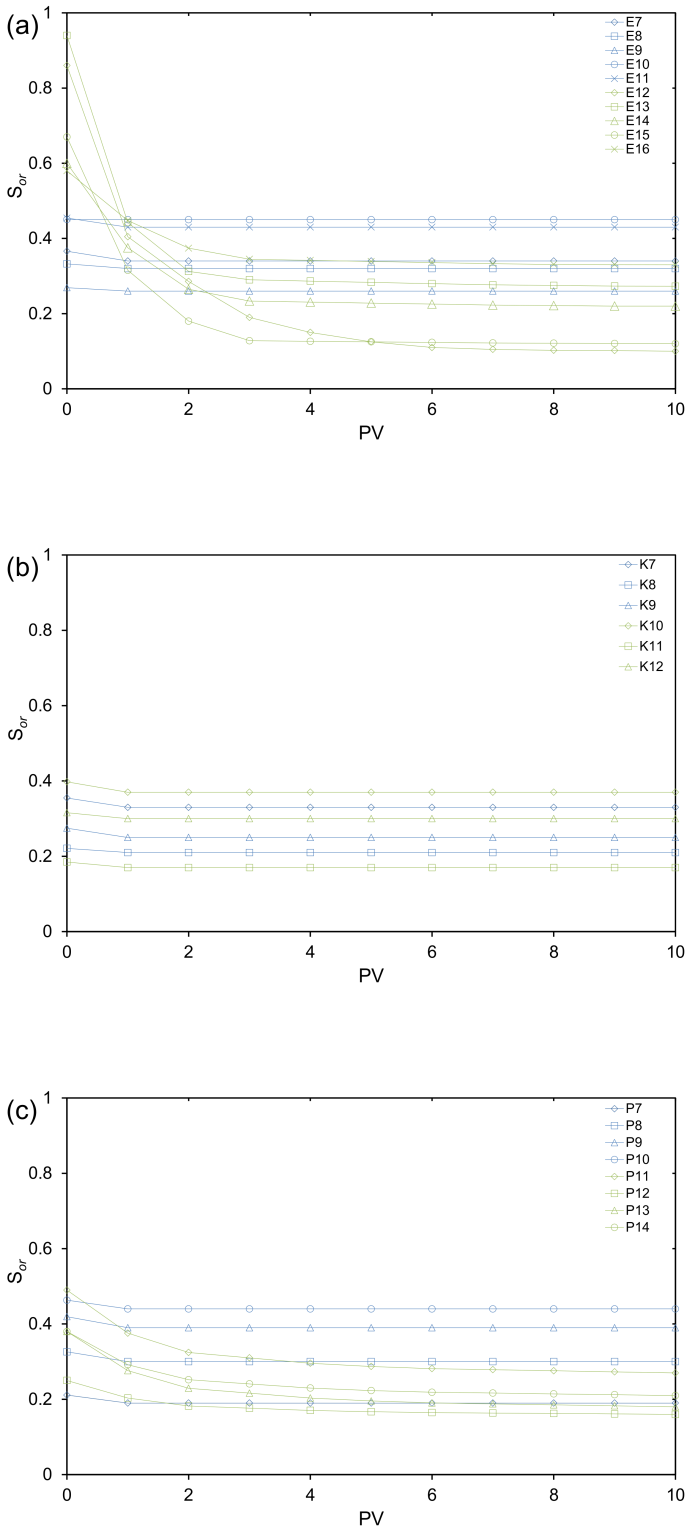

Figure 4.7. Remaining saturation as a function of pore volume injected at ambient conditions for (a) Estaillades, (b) Ketton, and (c) Portland. Blue lines indicate water-wet conditions, while the green curves are for altered-wettability.

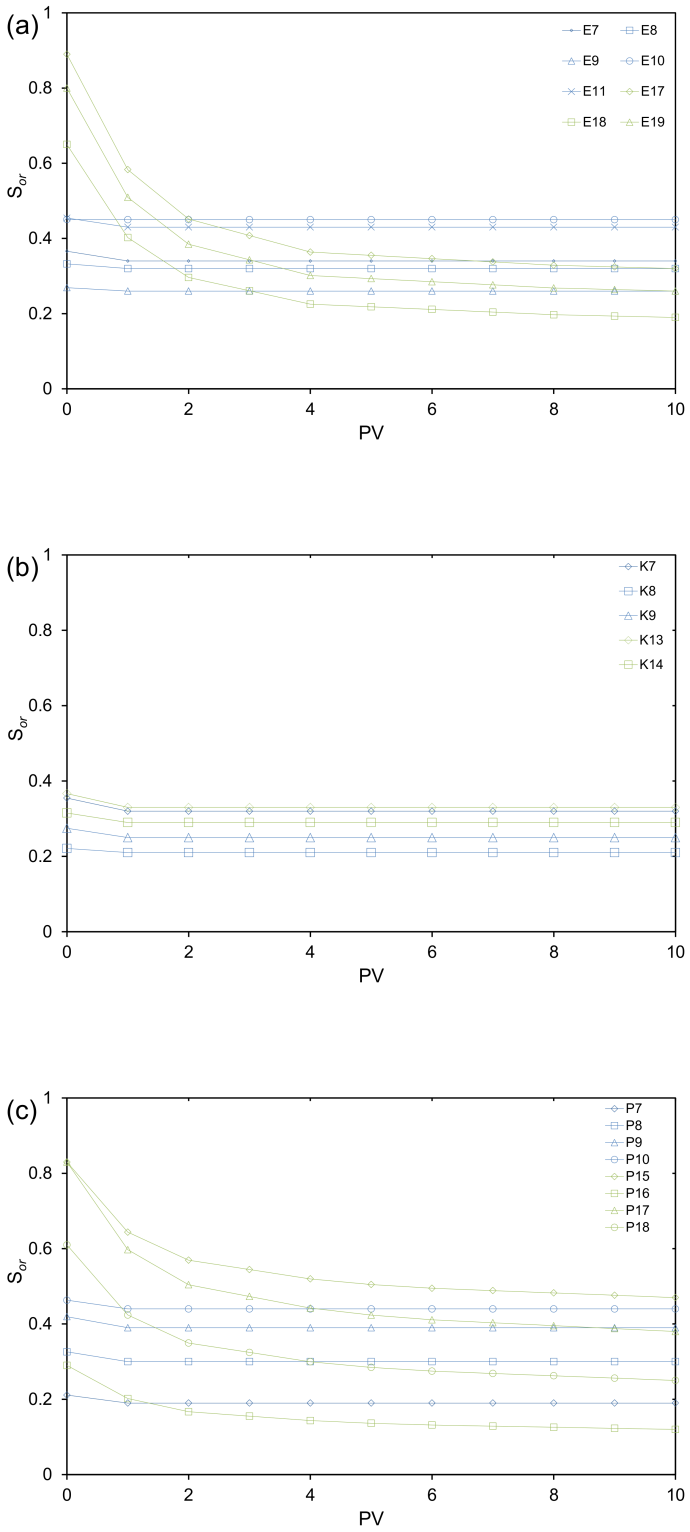

Figure 4.8. Remaining saturation as a function of pore volume injected at elevated temperatures for (a) Estaillades, (b) Ketton, and (c) Portland. Blue lines indicate water-wet conditions, while the green curves are for altered-wettability.

4.4. Pore-Scale Explanation

In this section, we will interpret the results in terms of pore-scale displacement processes. Specifically we will explain trapping and waterflood recovery for water-wet, intermediate-wet and oil-wet systems in the context of our results.

The water-wet behaviour is controlled, at the pore-scale, by snap-off, Figure 1.17. During waterflooding, water fills the narrowest regions of the pore space, stranding oil in the larger pores. This leads to a large residual saturation. S_{or} increases with S_{oi}, as the more of the pore space initially filled, the more oil that can be trapped, as shown in Figure 4.9.

In terms of relative permeability, see Figure 1.20, water is poorly connected, being in the smaller regions of the pore space or in wetting layers, and so is held back, allowing oil to flow readily. The consequence is that during waterflooding, the maximum recovery is seen at, or shortly after, breakthrough. Subsequent water injection does not recover additional oil, as we see in our experiments.

We see water-wet behaviour in all our samples without wettability alteration and in Ketton, where the water-filled micro-porosity appears to protect the solid from wettability alteration.

In intermediate-wet media with $\theta \approx 90^{\circ}$, we see less snap-off . As shown in Equation 1.10, snap-off becomes less favoured compared to direct displacement as the contact angle increases. In Figure 4.9, direct displacement of oil by water would simply push out the oil with no trapping. Hence, intermediate-wet systems see lower residual saturations: there is still some trapping by snap-off and bypassing, where a connected front of water simply surrounds the oil [*Lenormand et al.*, 1983]. Again, the higher S_{oi}, the more oil that can be trapped and so the trapping curve is monotonically increasing, as in the water-wet case.

In terms of relative permeability, Figure 1.20, water is better connected allowing for more rapid water advance than in a water-wet system. During waterflooding this can lead to earlier water breakthrough and some recovery of oil as more water is injected. However, as we see experimentally, Figures 4.7 and 4.8, this recovery is relatively small in some cases. In all intermediate-wet rocks, the remaining oil saturation at some value of PV injected will always increase with initial saturation–the recovery curves in Figures 4.7 and 4.8 do not cross.

In our experiments, intermediate-wet behaviour is observed, when crude oil is the wetting agent in Estaillades and Portland. This is consistent with contact angle measurements on smooth calcite. While some water is spontaneously imbibed, no oil is imbibed and we do not see the signature of oil layer drainage–very low S_{or}, significant post-breakthrough recovery and non-monotonic trapping curves. Hence, we assume in

these cases that we have $\theta_A \approx 90°$. We also see intermediate-wet behaviour for Portland with organic acid: here $I_w = I_o = 0$, but the waterflood behaviour indicates that the significant water-filled micro-porosity protects to some extent, the surfaces from a stronger wettability change.

We only see oil-wet behaviour in one case: Estaillades with organic acid. While $I_w = I_o = 0$, we can reach $S_{or} < 0.1$, see non-monotonic trapping curve and significant recovery after breakthrough. We now provide a pore-scale explanation for this behaviour.

Figure 1.18 shows how–if a pore is oil-wet–water can enter as the non-wetting phase, leaving an oil layer sandwiched between water in the corner and the oil in the centre of the pore. These layers keep the oil connected in the pore space, preventing trapping, but have a low conductance, meaning that the oil relative permeability is low. If the initial oil saturation is high, water is squeezed into the corners and the oil layers are thick. As more water is injected and the water pressure increases, the layers will become thinner and, when they collapse, will allow some oil to be trapped. However, as we see, remaining oil saturations of less than 10% are possible.

If S_{oi} is lower, more water initially resides in corners, the oil layers are thinner and more trapping is possible. This is the origin of a non-monotonic trapping curve and explains why the recovery plots in Figure 4.7a cross [*Jackson et al.*, 2003, *Spiteri et al.*, 2008].

For the very highest values of S_{oi} , however, S_{or} increases again. This is likely due to oil invading micro-porosity in which additional oil may be trapped.

In terms of waterflood recovery, we see early water breakthrough followed by significant recovery as more PV of water is injected, indicating the slow drainage of oil layers. It is likely that further, albeit modest, recovery would be observed had we injected more than 10 PV [*Salathiel*, 1973].

It is interesting that even for the same oil and physical conditions of temperature and pressure, we can observe very distinct behaviour for three rocks whose chemical composition (almost pure calcite) are similar: from water-wet behaviour in Ketton, to intermediate-wet in Portland, to intermediate to oil-wet in Estaillades. This demonstrates the need for good benchmark experiments, as clearly the behaviour is dependent to a significant degree on the pore structure. In particular, water-filled micro-porosity appears to protect the solid surfaces from wettability alteration in Ketton and, to a lesser extent, in Portland.

Future work could extend these studies to a wider range of rocks, mineralogies and oils, relating our macroscopic measurements with microscopic in situ determination of contact angle [*Andrew et al.*, 2014].

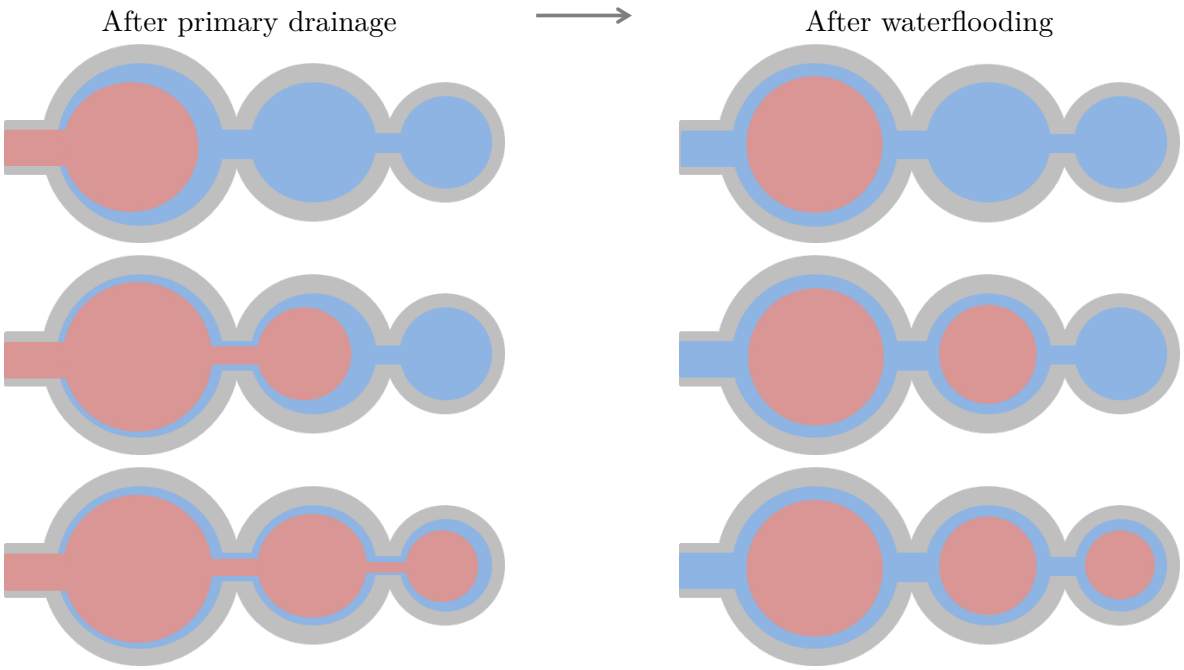

Figure 4.9. A pore-scale schematic demonstration showing how as S_{oi} increases, so does S_{or}, as oil (red) is trapped in progressively smaller pores (grey) by snap-off in water-wet medium by water (blue).

4.5. Conclusions

We have presented a methodology for the study of waterflood recovery in carbonates, combining a reproducible and instant method for ambient-condition wettability alteration with an organic acid and a crude oil ageing at high temperature. We see significant recovery by spontaneous imbibition in water-wet rocks, followed by little to no recovery by waterflooding. The trapping curve for these rocks is monotonically increasing as we expected. For altered-wettability rocks, the behaviour is more complex.

For Estaillades limestone, aged with organic acid, we observe a non-monotonic increase in the trapping curve consistent with oil-wet behaviour. When the core is aged with crude oil and replaced with decane, we observe an intermediate-wet behaviour, with slightly higher recovery than the water-wet case and a monotonic trapping curve.

For Ketton, we observe a monotonic increase in the trapping curve for both altered-wettability cases. This is explained by the nature of Ketton limestone having significant amount of micro-pores that are hard for the oil to access. Here we do not see evidence of wettability alteration.

For Portland, we observe an intermediate case between Estaillades and Ketton for both altered-wettability cases with higher recovery than the water-wet case but with a monotonic increase in the trapping curve. This can be explained by the pore structure, since Portland has the highest fraction of micro-porosity compared to the other limestones.

These results were explained and interpreted in terms of pore-scale displacement processes.

5. Conclusions and Recommendations for Future Work

5.1. Summary and Conclusions

In this thesis, we have investigated spontaneous imbibition in water-wet media and capillary trapping under different wetting conditions in carbonate rocks: Estaillades, Ketton, and Portland. This work has equal importance for IOR and CCS. For IOR, spontaneous imbibition is the main recovery mechanism in fractured reservoirs and capillary trapping is the main obstacle to tackle in order to maximise recovery. For CCS, imbibition is the process rendering the CO_2 immobile in aquifers and capillary trapping is one of the main mechanisms to store the CO_2 safely in the reservoir.

For **spontaneous imbibition**, we show a simplified derivation of the *Schmid et al.* 2011 analytical solution for spontaneous imbibition. We then perform co-current experiments using medical CT imaging with an air/brine fluid pair. We match the experimental ratio of distance to the square-root of time, ω, with the analytical solution for ω by using physically plausible relative permeability and capillary pressure functions. Since the analytical solution is a function of relative permeability and capillary pressure, it can be a powerful tool to estimate multi-phase flow properties and can be used in combination with other experiments to determine relative permeabilities and capillary pressures.

One of the main parameters in the analytical solution is the C constant which quantifies the rock's rate of imbibition. We showed two methods to find this value: (1) from computing the relative permeability and capillary pressure in the analytical solution. (2) From experimental measurement of the mass of water imbibed as a function of time. The C value is also important for the scaling equation derived by *Schmid and Geiger* 2012 which is an extension from the analytical solution of spontaneous imbibition. We found C for several samples of each rock type studied.

For **capillary trapping and oil recovery** we have presented a methodology for the study of waterflood recovery in carbonates, with an instant method for ambient-condition wettability alteration. We find a non-monotonic trend between initial oil saturation and the remaining oil saturation after 10 PV injected at high flow rates in Estaillades with altered wettability. This behaviour can be explained in terms of the pore-scale configuration of fluids. First, we observe a monotonic increase in the trapping curve, where the initial water saturation is high. This is followed by a decrease in the trapping curve due to the formation of oil layers that will collapse with sufficient water pressure leading to higher oil recovery than the first phase. Finally, we notice an increase in the trapping curve as micro-porosity is invaded. For elevated temperature, we observe weaker wettability alteration than the ambient condition, leading a monotonic increase in the trapping curve with higher recovery than the water-wet case. Again this can be explained in terms of pore-scale displacement processes–specifically the suppression of snap-off.

For Ketton, we observe a monotonic increase in the trapping curve, with the data overlapping with the water-wet data indicating no wettability alteration. This is due to Ketton's complex pore structure with tiny micro-pores that can only be accessible at high pressures that we do not capture in our experiments. It appears that the water-filled micro-porosity protects the surface from wettability alteration. Similarly, we see the same behaviour for elevated temperature experiments with crude oil.

For Portland at ambient conditions, we observe an intermediate case between Estaillades and Ketton with a monotonic increase in the trapping curve but with higher recovery. This is also due to Portland's pore structure with the highest fraction of micro-porosity. In our experiment, we access some of these pores leading to some wettability alteration in Portland. Similarly, we observe the same behaviour in the elevated temperature experiments.

Overall, we can see that pore structure has a major impact on wettability alteration while wettability itself has a big impact on residual saturation and waterflood recovery. The results indicate that altered-wettability reservoirs may have the highest oil recovery by waterflooding. In contrast, water-wet reservoirs such as saline aquifers are the best location for CCS as they will trap more CO_2 (non-wetting phase) than an altered-wettability reservoir.

While this work has provided several useful insights into muti-phase flow in porous media, we are still some way from a predective methodology to understand oil recovery and long-term CO_2 storage. There is ample opportunity for future work, addressed below.

5.2. Recommendations for Future Work

5.2.1. Spontaneous Imbibition

To expand the spontaneous imbibition work, we should include initial water saturations. Having initial water saturations make the system more realistic and representative of reservoir conditions. In addition, the analytical solution could be used to find the relative permeability and/or capillary pressure from a simple experiment with the combination of the analytical solution. Therefore, an experimental investigation correlating the measured relative permeability and capillary pressure to the measured saturation profile will validate the analytical solution furthermore.

This work can also be used to improve the development of the numerical models to study the capillary dominated flow in fractured carbonates. For example, using the analytical solution to validate the prediction of numerical simulation or pore-scale modelling for capillary dominated flow, in the same manner as Buckley-Leverett analysis used to assess viscous dominated flow.

Also, using different rock types, as we have shown, different rocks with different permeabilities behave differently. It would be interesting to compare this study to sandstone rocks where there is no micro-porosity. In addition, tackling different wettability systems, mainly mixed-wet as many of the world's reservoirs are believed to be mixed-wet, will add substantial value to the understanding of reservoir engineering.

As well, using different fluid pairs with different viscosity ratio and compare the saturation profile of co-current and counter-current flow. In our case we used gas and brine fluid pair leading to a very high viscosity ratio ≈ 560, other suggestions can be n-decane and brine with viscosity ratio ≈ 1 and high viscosity crude oil and brine with viscosity ratio < 1.

5.2.2. Capillary Trapping and Oil Recovery

For future work, we suggest extending our experimental study and, in combination with the numerical and analytical analysis, provide a predictive framework for understanding waterflood and imbibition recovery in carbonates of different wettability. Moreover, numerical simulation can be used to compare our experimental results especially when dealing with altered-wettability system as the flow behaviour is more complex.

Specifically we could perform more experiments with different initial oil saturations and try different organic acids from the cyclohexane family group to observe the effect of contact angle on residual saturation. This could also be studied by using different crude oils to span a wide range of effective contact angles.

Further, we suggest working with less heterogeneous rocks i.e. sandstone rocks in order to achieve homogenous and reproducible wettability alteration and then observe the trapping curve at different initial saturations.

Also, we recommend using micro-CT to investigate the same type of experiment but on the micro-scale in order to visualise the process of wettability alteration and the residual saturation. This will help us to understand the effect of wettability on multi-phase flow in porous media. In addition, micro-CT will help us visualise the oil layer formation and in-situ contact angle as well as observe the oil layer drainage and the collapse of oil layers in waterflooding [*Andrew et al.*, 2014].

Further, we suggest looking at the effect of wettability on spontaneous imbibition and that can be incorporated with a medical CT and/or micro-CT experiment to visualise the process of imbibition inside the rock. Further this work can be incorporated with the analytical solution discussed in Chapter 3 to estimate the multi-phase flow properties.

Bibliography

Abdallah, W., J. S. Buckley, A. Carnegie, J. Edwards, B. Herold, A. Graue, T. Hasbashy, N. Seleznev, C. Singer, H. Hussain, B. Montaron, and M. Ziauddin (1986), Fundamentals of wettability, *Technology*, *38*, 1125-1144.

Akbarabadi, M., and M. Piri (2013), Relative permeability hysteresis and capillary trapping characteristics of supercritical CO_2/brine systems: An experimental study at reservoir conditions, *Advances in Water Resources*, *52*, 190-206,doi:10.1016/j.advwatres.2012.06.014.

Al Ghafri, S., G. C. Maitland, and J. P. M. Trusler (2012), Densities of aqueous $MgCl_2$ (aq), $CaCl_2$ (aq), KI (aq), NaCl (aq), KCl (aq), $AlCl_3$ (aq), and (0.964 NaCl+ 0.136 KCl)(aq) at temperatures between (283 and 472) K, pressures up to 68.5 MPa, and molalities up to 6 mol.kg^{-1}, *Journal of Chemical & Engineering Data*, *57*, 1288-1304, doi:10.1021/je2013704.

Alley, R., T. Berntsen, N. L. Bindoff, Z. Chen, A. Chidthaisong, P. Friedlingstein, J. Gregory, G. Hegerl, M. Heimann, B. Hewitson, B. Hoskins, F. Joos, J. Jouzel, V. Kattsov, U. Lohmann, M. Manning, T. Matsuno, M. Molina, N. Nicholls, J. Overpeck, D. Qin, G. Raga, V. Ramaswamy, J. Ren, M. Rusticucci, S. Solomon, R. Somerville, T. F. Stocker, P. Stott, R. J. Stouffer, P. Whetton, R. A. Wood, and D. Wratt (2007), Climate Change 2007: The Physical Science Basis, *Summary for Policymakers*, *Intergovernmental Panel on Climate Change: Geneva, CH*.

Al Mansoori, S., S. Iglauer, C. H. Pentland, B. Bijeljic, and M. J. Blunt (2009), Measurements of non-wetting phase trapping applied to carbon dioxide storage, *Energy Procedia*, *1*, 3173–3180, doi:10.1016/j.egypro.2009.02.100.

Amott, E (1959), Observations relating to the wettability of porous rock, *Trans. AIME*, *219*, 156-162.

Anderson, W. G (1987), Wettability literature survey-part 1: rock/oil/brine interactions and the effects of core handling on wettability, *Journal of Petroleum Technology*, *38*, 1125–1144, doi:10.2118/13932-PA.

Anderson, W. G (1987), Wettability literature survey-part 4: Effects of wettability on capillary pressure, *Journal of Petroleum Technology*, *39*, 1283–1300, doi:10.2118/15271-PA.

Anderson, W. G (1987), Wettability literature survey part 5: The effects of wettability on relative permeability, *Journal of Petroleum Technology*, *39*, 1453–1468, doi:10.2118/16323-PA.

Anderson, W. G (1987), Wettability literature survey-part 6: the effects of wettability on waterflooding, *Journal of Petroleum Technology*, *39*, 1605–1622, doi:10.2118/16471-PA.

Andrew, M., B. Bijeljic, and M. J. Blunt (2014), Pore-scale imaging of trapped supercritical carbon dioxide in sandstones and carbonates, *International Journal of Greenhouse Gas Control*, *22*, 1–14, doi:10.1016/j.ijggc.2013.12.018.

Andrew, M., B. Bijeljic, and M. J. Blunt (2014), Pore-scale contact angle measurements at reservoir conditions using X-ray microtomography, *Advances in Water Resources*, *68*, 24–31, doi:10.1016/j.advwatres.2014.02.014.

Ashton, M (1980), The stratigraphy of the Lincolnshire limestone formation (Bajocian) in Lincolnshire and Rutland (Leicestershire), *Proceedings of the Geologists' Association*, *91*, 203-223, doi:10.1016/S0016-7878(80)80040-X.

Babadagli, B., and I. Ershaghi (1992), Imbibition assisted two-phase flow in natural fractures, *Proceedings of the SPE Western Regional Meeting, 30 March-1 April, Bakersfield, California*, SPE-24044-MS, doi:10.2118/24044-MS.

Bachu, S., W. D. Gunter, and E. H. Perkins (1994), Aquifer disposal of CO_2: Hydrodynamic and mineral trapping, *Energy Conversion and Management*, *35*, 269-279, doi:10.1016/0196-8904(94)90060-4.

Bear, J (1988), Dynamics of fluids in porous media, *Courier Dover Publications*, New York.

Blunt, M. J. (2010), Carbon dioxide storage, *Grantham Institute for Climate Change*, *4*, `https://workspace.imperial.ac.uk/climatechange/Public/pdfs/Briefing%20Papers/Briefing%20Paper%204.pdf`.

Blunt, M. J., B. Bijeljic, H. Dong, O. Gharbi, S. Iglauer, P. Mostaghimi, A. Paluszny, and C. Pentland (2013), Pore-scale imaging and modelling, *Advances in Water Resources*, *51*, 197–216, doi:10.1016/j.advwatres.2012.03.003.

Bourbiaux, B. J., and F. J. Kalaydjian (1990), Experimental study of cocurrent and countercurrent flows in natural porous media, *SPE Reservoir Engineering*, *5*, 361–368, doi:10.2118/18283-PA.

Brenchley, P. J., and P. F. Rawson (2006), The geology of England and Wales, *The Geological Society*, London.

Brunauer, S., P. H. Emmett, and E. Teller (1938), Adsorption of gases in multimolecular layers, *Journal of the American Chemical Society*, *60*, 309-319, doi:10.1021/ja01269a023.

Buckley, J. S. (1995), Asphaltene precipitation and crude oil wetting, *SPE Advanced Technology Series*, *3*, 53-59, doi:10.2118/26675-PA.

Buckley, J. S., C. Bousseau, and Y. Liu (1996), Wetting alteration by brine and crude oil: From contact angles to cores, *SPE Journal*, *1*, 341-350, doi:10.2118/30765-PA.

Buckley, J. S., and Y. Liu (1998), Some mechanisms of crude oil/brine/solid interactions, *Journal of Petroleum Science and Engineering*, *20*, 155-160, doi:10.1016/S0920-4105(98)00015-1.

Buckley, J. S. (2001), Effective wettability of minerals exposed to crude oil, *Current Opinion in Colloid & Interface Science*, *6*, 191-196, doi:10.1016/S1359-0294(01)00083-8.

Buckley, J. S., T. Fan, Z. Tong, and N. R. Morrow (2006), Some mechanisms of crude oil/brine/solid interactions, *Proceedings of Society of Core Analysts held in Trondheim, Norway*, SCA2006-02.

Buckley, J. S., and T. Fan (2007), Acid number measurements revisited, *SPE Journal*, *12*, doi:10.2118/99884-PA.

Buckley, S. E., and M. C. Leverett (1942), Mechanism of fluid displacement in sands, *Transactions of the AIME*, *146*, 107-116, doi:10.2118/942107-G.

Chatzis, I., and N. R. Morrow (1984), Correlation of capillary number relationships for sandstone, *SPE Journal*, *24*, 555-562, doi:10.2118/10114-PA.

Craig, F. F. (1971), The reservoir engineering aspects of waterflooding, *Monograph SeriesSoc. Petrol. Eng, Dallas*, *3*.

Crowell, D. C., G. W. Dean, and A. G. Loomis (1966), Efficiency of gas displacement from a water-drive reservoir, *US Dept. of the Interior, Bureau of Mines*, *6735*.

Dake, L. P (1983), Fundamentals of reservoir engineering, *Elsevier Science*, USA, *volume 8*.

Dong, H., and M. J. Blunt (2009), Pore-network extraction from micro-computerized-tomography images, *Phys. Rev. E*, *80*, 036307, doi:10.1103/PhysRevE.80.036307.

de Gennes, P-G., F. Brochard-Wyart, and D. Quéré (2004), Capillarity and wetting phenomena: drops, bubbles, pearls, waves, *Springer*, USA.

Dullien, F. A. L. (1991), Porous media: fluid transport and pore structure, *Academic Press*, New York.

El-Maghraby, R. M., C. H. Pentland, S. Iglauer, and M. J. Blunt (2012), A fast method to equilibrate carbon dioxide with brine at high pressure and elevated temperature including solubility measurements, *The Journal of Supercritical Fluids*, *62*, 55-59, doi:10.1016/j.supflu.2011.11.002.

El-Maghraby, R. M., and M. J. Blunt (2013), Residual CO_2 Trapping in Indiana Limestone, *Environ. Sci. Technol.*, *47 (1)*, pp 227–233, doi:10.1021/es304166u.

Fernø, M. A., M. Torsvik, S. Haugland, and A. Graue (2010), Dynamic laboratory wettability alteration, *Energy & Fuels*, *24*, 3950–3958, doi:10.1021/ef1001716.

Fernø, M. A., Å. Haugen, S. Wickramathilaka, J. Howard, A. Graue, G. Mason, and N. R. Morrow (2013), Magnetic resonance imaging of the development of fronts during spontaneous imbibition, *Journal of Petroleum Science and Engineering*, *101*, 1–11, doi:10.1016/j.petrol.2012.11.012.

Fernø, M. A., Å. Haugen, G. Mason, and N. R. Morrow (2014), Measurement of core properties using a new technique – two ends open spontaneous imbibition, *Proceedings of Society of Core Analysts held in Avignon, France*, SCA2014-006.

Friedlingstein, P., R. A. Houghton, G. Marland, J. Hackler, T. A. Boden, T. J. Conway, J. G. Canadell, M. R. Raupach, P. Ciais, and C. Le Quéré (2010), Update on CO_2 emissions, *Nature Geoscience*, *3*, 811-812, doi:10.1038/ngeo1022.

Garg, A., E. Zwahlen, and T.W. Patzek (1996), Experimental and numerical studies of one-dimensional imbibition in Berea sandstone, *Proceedings of the 16th Annual American Geophysical Union Hydrology Days, Fort Colllins, CO, 15-18 April*.

Geffen, T. M., D. R. Parrish, G. W. Haynes, and R. A. Morse (1952), Efficiency of gas displacement from porous media by liquid flooding, *Journal of Petroleum Technology*, *4*, 29-38, doi:10.2118/952029-G.

Gharbi, O., and M. J. Blunt (2012), The impact of wettability and connectivity on relative permeability in carbonates: A pore network modeling analysis, *Water Resour. Res.*, *48*, W12513, doi:10.1029/2012WR011877.

Gibbins, J., and H. Chalmers (2008), Carbon capture and storage, *Energy Policy*, *36(12)*, 4317-4322, doi:10.1016/j.enpol.2008.09.058.

Girifalco, L. A., and R. J. Good (1957), A theory for the estimation of surface and interfacial energies. I. Derivation and application to interfacial tension, *J. Phys. Chem.*, *61(7)*, 904-909, doi:10.1021/j150553a013.

Graue, A., B. G. Viksund, T. Eilertsen, and R. Moe (1999), Systematic wettability alteration by aging sandstone and carbonate rock in crude oil, *Journal of Petroleum Science and Engineering*, *24*, 85-97, doi:10.1016/S0920-4105(99)00033-9.

Graue, A., and M. Fernø (2011), Water mixing during spontaneous imbibition at different boundary and wettability conditions, *Journal of Petroleum Science and Engineering*, *78*, 586-595, doi:10.1016/j.petrol.2011.07.013.

Gunter, W. D., E. H. Perkins, and T. J. McCann (1993), Aquifer disposal of CO_2-rich gases: Reaction design for added capacity, *Energy Conversion and Management*, *34*, 941-948, doi:10.1016/0196-8904(93)90040-H.

Hafez, H. H., A. Ismail, and M. Kalam (2013), A workflow for developing water-oil relative permeability hysteresis - super giant carbonate reservoir case study, *Proceedings of the ASPE Reservoir Characterization and Simulation Conference and Exhibition, 16-18 September, Abu Dhabi, UAE*, SPE-165957-MS, doi:10.2118/165957-MS.

Handy, L. L. (1960), Determination of effective capillary pressures for porous media from imbibition data, *AIME*, *219*, 75-80.

Haugen, Å., M. A. Fernø, G. Mason, and N. R. Morrow (2014), Capillary pressure and relative permeability estimated from a single spontaneous imbibition test, *Journal of Petroleum Science and Engineering*, *115*, 66-77, doi:10.1016/j.petrol.2014.02.001.

Humphry, K. J., B. M. J. M. Suijkerbuijk, H. A. van der Linde, S. G. J. Pieterse, and S. K. Masalmeh (2013), Impact of wettability on residual oil saturation and capillary desaturation curves, *Proceedings of Society of Core Analysts held in Napa Valley, California, USA*, SCA2013-025.

International Energy Agency (2012), World Energy Outlook 2012, `http://www.iea.org/publications/freepublications/publication/WEO2012_free.pdf`.

Jackson, M. D., P. H. Valvatne, and M. J. Blunt (2003), Prediction of wettability variation and its impact on flow using pore-to reservoir-scale simulations, *Journal of Petroleum Science and Engineering*, *39*, 231–246, doi:10.1016/S0920-4105(03)00065-2.

Jadhunandan, P. P., and N. R. Morrow (1995), Effect of wettability on waterflood recovery for crude-oil/brine/rock systems, *SPE Reservoir Engineering*, *10*, 40-46, doi:10.2118/22597-PA.

Jingyan, L., C. Xiaoli, and T. Songbai (2012), Research on determination of total acid number of petroleum using mid-infrared attenuated total reflection spectroscopy, *Energy & Fuels*, *26*, 5633–5637, doi:10.1021/ef3002372.

Johannesen, E. B., and A. Graue (2007), Mobilization of remaining oil - emphasis on capillary number and wettability, *Proceedings of International Oil Conference and Exhibition in Mexico, 27-30 June, Veracruz*, SPE-108724-MS, doi:10.2118/108724-MS.

Juanes, R., C. W. MacMinn, and M. L. Szulczewski (2010), The footprint of the CO_2 plume during carbon dioxide storage in saline aquifers: storage efficiency for capillary trapping at the basin scale, *Transp Porous Med*, *82*, 19-30, doi:10.1007/s11242-009-9420-3.

Karabakal, U., and S. Bagci (2004), Determination of wettability and its effect on waterflood performance in limestone medium, *Energy Fuels*, *18 (2)*, 438-449, doi:10.1021/ef030002f.

Klinkenberg, L. J. (1941), The permeability of porous media to liquids and gases, *American Petroleum Institute*.

Kovscek, A. R., H. Wong, and C. J. Radke (1993), A pore-level scenario for the development of mixed wettability in oil reservoirs, *Environmental and Energy Engineering*, *39*, 1072-1085, doi:10.1002/aic.690390616.

Krevor, S. C. M, R. Pini, B. Li, and S. M. Benson (2011), Capillary heterogeneity trapping of CO_2 in a sandstone rock at reservoir conditions, *Geophysical Research Letters*, *38*, L15401, doi:10.1029/2011GL048239.

Krevor, S. C. M, M. J. Blunt, S. M. Benson, C. H. Pentland, C. Reynolds, A. Al-Menhali, and B. Niu (2015), Capillary trapping for geologic carbon dioxide storage – From pore scale physics to field scale implications, *International Journal of Greenhouse Gas Control*, doi:10.1016/j.ijggc.2015.04.006.

Lababjos-Broncano, L., M. L. González-Martín, J. M. Braque, and C. M. González-García (2001), Influence of the meniscus at the bottom of the solid plate on imbibition experiments, *Journal of Colloid and Interface Science*, *234(1)*, 79-83, doi:10.1006/jcis.2000.7244.

Lake, L. W (1989), Enhanced oil recovery, *Old Tappan, NJ; Prentice Hall Inc.*

Lamy, C. M. M., S. Iglauer, C. H. Pentland, M. J. Blunt, and G. C. Maitland (2010), Enhanced oil recovery, *Proceedings of the SPE EUROPEC/EAGE Annual Conference and Exhibition, 14-17 June, Barcelona, Spain*, SPE-130720-MS, doi:10.2118/130720-MS.

Land, C. S (1971), Comparison of calculated with experimental imbibition relative permeability, *SPE Journal*, *11*, 419-425, doi:10.2118/3360-PA.

Lenormand, R., C. Zarcone, and A. Sarr (1983), Mechanisms of the displacement of one fluid by another in a network of capillary ducts, *Journal of Fluid Mechanics*, *135*, 337-353.

Lenormand, R., and C. Zarcone (1984), Role of roughness and edges during imbibition in square capillaries, *Proceedings of SPE Annual Technical Conference and Exhibition, 16-19 September, Houston, Texas*, SPE-13264-MS, doi:10.2118/13264-MS.

Lenormand, R., A. Eisenzimmer, and P. Delaplace (1995), Improvements of the Semi-Dynamic Method for Capillary Pressure Measurements, *Proceedings of Society of Core Analysts held in San Francisco, CA, USA*, SCA1995-31.

Li, K., and R. N. Horne (2001), Characterization of spontaneous water imbibition into gas-saturated rocks, *SPE Journal*, *6*, 375-384, doi:10.2118/74703-PA.

Li, K., K. Chow, and R. N. Horne (2002), Effect of initial water saturation on spontaneous water imbibition, *Proceedings of SPE Western Regional/AAPG Pacific Section Joint Meeting, 20-22 May, Anchorage, Alaska*, SPE-76727-MS, doi:10.2118/76727-MS.

Li, K., and R. N. Horne (2005), Extracting capillary pressure and global mobility from spontaneous imbibition data in oil-water-rock systems, *SPE Journal*, *10*, 458-465, doi:10.2118/80553-PA.

Li, K., and R. N. Horne (2006), Generalized scaling approach for spontaneous imbibition: an analytical model, *SPE Reservoir Evaluation & Engineering*, *9*, 251-258, doi:10.2118/77544-PA.

Li, X., H. van der Linde, W. J. Looyestijin, J. Romanuka, J. P. M. Trusler, G. C. Maitland, E. S. Boek, and H. Ott (2015), Experimental investigation of carbonate reservoir wettability dependence on the salinity of flooding water, *(in preparation)*.

Lide, D. R (2004), CRC handbook of chemistry and physics, *CRC*.

Lindeberg, E., and D. Wessel-Berg (1997), Vertical convection in an aquifer column under a gas cap of CO_2, *Energy Conversion and Management*, *38*, S229-S234, doi:10.1016/S0196-8904(96)00274-9.

Ma, T. D., and G. K. Youngren (1994), Performance of Immiscible Water-Alternating-Gas (IWAG) Injection at Kuparuk River Unit North Slope Alaska, *Proceedings of the SPE Annual Technical Conference and Exhibition, 25-28 September, New Orleans, Louisiana*, SPE-28602-MS, doi:10.2118/28602-MS.

Ma, S., N. R. Morrow, and X. Zhang (1997), Generalized scaling of spontaneous imbibition data for strongly water-wet systems, *Journal of Petroleum Science and Engineering*, *18*, 165–178, doi:10.1016/S0920-4105(97)00020-X.

Mattax, C.C., and J. R. Kyte (1962), Imbibition oil recovery from fractured, water-drive reservoir, *Society of Petroleum Engineers Journal*, *2(2)*, 177-184, doi:10.2118/187-PA.

Macminn, C. W., M. L. Szulczewski, and R. Juanes (2010), CO_2 migration in saline aquifers. Part 1. Capillary trapping under slope and groundwater flow, *Journal of Fluid Mechanics*, *662*, 329-351, doi:10.1017/S0022112010003319.

Masalmeh, S. K (2000), High oil recoveries from transition zones, *Abu Dhabi International Petroleum Exhibition and Conference*, SPE-87291-MS, doi:10.2118/87291-MS.

Masalmeh, S. K., and S. Oedai (2000), Oil mobility in transition zone, *Proceedings of Society of Core Analysts held in Abu Dhabi, UAE*, SCA2000-02.

Masalmeh, S. K (2002), The effect of wettability on saturation functions and impact on carbonate reservoirs in the middle east, *Abu Dhabi International Petroleum Exhibition and Conference*, SPE-78515-MS, doi:10.2118/78515-MS.

Masalmeh, S. K., I. M. Abu-Shiekah, and X. Jing (2007), Improved characterization and modeling of capillary transition zones in carbonate reservoirs, *SPE Reservoir Evaluation & Engineering*, *10*, 191–204, doi:10.2118/109094-PA.

Masalmeh, S. K. (2012), Impact of Capillary forces on residual oil saturation and flooding experiments for mixed to oil-wet carbonate reservoirs, *Proceedings of Society of Core Analysts held in Aberdeen, Scotland, UK*, SCA2012-11.

Mason, G., H. Fischer, N. R. Morrow, E. Johannesen, Å. Haugen, A. Graue, and M. A. Fernø (2010), Oil production by spontaneous imbibition from sandstone and chalk cylindrical cores with two ends open, *Energy & Fuels*, *24*, 1164-1169, doi:10.1021/ef901118n.

Mason, G., M. A. Fernø, Å. Haugen, N. R. Morrow, and D. W. Ruth (2012), Spontaneous counter-current imbibition outwards from a hemi-spherical depression, *Journal of Petroleum Science and Engineering*, *90-91*, 131-138, doi:10.1016/j.petrol.2012.04.017.

Mason, G., and N. R. Morrow (2013), Developments in spontaneous imbibition and possibilities for future work, *Journal of Petroleum Science and Engineering*, *110*, 268-293, doi:10.1016/j.petrol.2013.08.018.

Metz, B., O. Davidson, H. D. Coninck, M. Loos, and L. Meyer (2005), Carbon dioxide capture and storage, *Intergovernmental Panel on Climate Change, Geneva, Switzerland*, http://www.ipcc.ch/pdf/special-reports/srccs/srccs_wholereport.pdf.

Metz, B., O. Davidson, H. D. Coninck, M. Loos, and L. Meyer (2005), IPCC special report on carbon dioxide capture and storage, *Cambridge University Press*.

Morrow, N. R. (1975), The effects of surface roughness on contact: angle with special reference to petroleum recovery, *Journal of Canadian Petroleum Technology*, *14*, doi:10.2118/75-04-04.

Morrow, N. R., S. Ma, X. Zhou, and X. Zhang (1994), Characterization of wettability from spontaneous imbibition measurements, *Proceedings of the Annual Technical Meeting, June 12 - 15, Calgary, Alberta*, PETSOC-94-47, doi:10.2118/94-47.

Morrow, N. R., and G. Mason (2001), Recovery of oil by spontaneous imbibition, *Current Opinion in Colloid & Interface Science*, *6*, 321–337, doi:10.1016/S1359-0294(01)00100-5.

Morse, J. W., and R. S. Arvidson (2002), The dissolution kinetics of major sedimentary carbonate minerals, *Earth-Science Reviews*, *58*, 51–84, doi:10.1016/S0012-8252(01)00083-6.

Muir-Wood, H. M., and D. Sc. F.G.S. (1952), Some jurassic brachiopoda from the Lincolnshire limestone and upper estuarine series of rutland and Lincolnshire, *Proceedings of the Geologists' Association*, *113*, 113–142, doi:10.1016/S0016-7878(52)80014-8.

Munson, B. R., D. F. Young, and T. H. Okiishi (1990), Fundamentals of fluid mechanics, *Wiley, New York*.

National Research Council (2010), Advancing the Science of Climate Change, *The National Academies Press*, `http://www.nap.edu/openbook.php?record_id=12782`.

Nono, F., H. Bertin, and G. Hamon (2014), Oil recovery in the transition zone of carbonate reservoirs with wettability change: hysteresis models of relative permeability versus experimental data, *Proceedings of Society of Core Analysts held in Avignon, France*, SCA2014-007.

Olafuyi, O. A., Y. Cinar, M. A. Knackstedt, and W. V. Pinczewski (2007), Spontaneous imbibition in small cores, *Proceedings of the Asia Pacific Oil and Gas Conference and Exhibition, 30 October-1 November, Jakarta, Indonesia*, SPE-109724-MS, doi:10.2118/109724-MS.

Otsu, N (1975), A threshold selection method from gray-level histograms, *Automatica*, *11*, 285-396.

Ott, H., C. Pentland, and S. Oedai (2014), CO_2-brine displacement in heterogeneous carbonates, *Proceedings of Society of Core Analysts held in Avignon, France*, SCA2014-019.

Pentland, C. H., E. Itsekiri, S. Al-Mansoori, S. Iglauer, B. Bijeljic, and M. J. Blunt (2010), Measurement of nonwetting-phase trapping in sandpacks, *SPE Journal*, *15*, 274-281, doi:10.2118/115697-PA.

Pentland, C. H., Y. Tanino, S. Iglauer, and M. J. Blunt (2010), Residual saturation of water-wet sandstones: Experiments, correlations and pore-scale modeling, *Proceedings of the SPE Annual Technical Conference and Exhibition, Florence, Italy*, SPE 133798, doi:10.2118/133798-MS.

Pentland, C. H., R. El-Maghraby, S. Iglauer, and M. J. Blunt (2011), Measurements of the capillary trapping of super-critical carbon dioxide in Berea sandstone, *Geophysical Research Letters*, *38*, L06401, doi:10.1029/2011GL046683.

Pini, R. S. M. Krevor, and S. M. Benson (2012), Capillary pressure and heterogeneity for the CO_2/water system in sandstone rocks at reservoir conditions, *Advances in Water Resources*, *38*, 48-59, doi:10.1016/j.advwatres.2011.12.007.

Pooladi-Dravish, M., and A. Firoozabadi (2000), Cocurrent and countercurrent imbibition in a water-wet matrix block, *SPE Journal*, *5*, 3-11, doi:10.2118/38443-PA.

Salathiel, R. A (1973), Oil recovery by surface film drainage in mixed-wettability rocks, *Journal of Petroleum Technology*, *25*, 1216-1224, doi:10.2118/4104-PA.

Schlumberger (2013), Carbonate reservoirs, `http://www.slb.com/services/technical_challenges/carbonates.aspx`.

Schmid, K. S., S. Geiger, and K. S. Sorbie (2011), Semianalytical solutions for cocurrent and countercurrent imbibition and dispersion of solutes in immiscible two-phase flow, *Water Resour. Res.*, *47*, W02550, doi:10.1029/2010WR009686.

Schmid, K. S., and S. Geiger (2012), Universal scaling of spontaneous imbibition for water-wet systems, *Water Resour. Res.*, *48*, W03507, doi:10.1029/2011WR011566.

Schmid, K. S., and S. Geiger (2013), Universal scaling of spontaneous imbibition for arbitrary petrophysical properties: Water-wet and mixed-wet states and Handy's conjecture, *Journal of Petroleum Science and Engineering*, *101*, 44-61, doi:10.1016/j.petrol.2012.11.015.

Skauge, A., A. Sørvik, B. Vik, and K. Spildo (2006), Effect of wettability on oil recovery from carbonate material representing different pore classes, *Proceedings of Society of Core Analysts held in Trondheim, Norway*, SCA2006-01.

Spiteri, E., R. Juanes, M. J. Blunt, and F. M. Orr (2008), A new model of trapping and relative permeability hysteresis for all wettability characteristics, *SPE Journal*, *13*, 277-288, doi:10.2118/96448-PA.

Stocker, T. F., D. Qin, G-K. Plattner, M. M. B. Tignor, S. K. Allen, J. Boschung, A. Nauels, Y. Xia, V. Bex, and P. M. Midgley (2013), Climate Change 2013: The Physical Science Basis, *Working Group I Contribution to the IPCC Fifth Assessment Report (AR5)*, *Cambridge Univ Press, New York*.

Straley, C., D. Rossini, H. Vinegar, T. Pierre, and C. Morriss (1997), Core analysis by low-field NMR, *Log Anal*, *38(2)*, 84-93.

Suzanne, K., G. Hamon, J. Billiotte, and V. Trocme (2003), Experimental relationships between residual gas saturation and initial gas saturation in heterogeneous sandstone reservoirs, *Proceedings of the SPE Annual Technical Conference and Exhibition, 5-8 October, Denver, Coloradol*, SPE-84038-MS, doi:10.2118/84038-MS.

Tanino, Y., and M. J. Blunt (2012), Capillary trapping in sandstones and carbonates: Dependence on pore structure, *Water Resour. Res.*, *48*, W08525, doi:10.1029/2011WR011712.

Tanino, Y., and M. J. Blunt (2013), Laboratory investigation of capillary trapping under mixed-wet conditions, *Water Resour. Res.*, *49*, 4311–4319, doi:10.1002/wrcr.20344.

Tavassoli, Z., R. W. Zimmerman, and M. J. Blunt (2005), Analysis of counter-current imbibition with gravity in weakly water-wet systems, *Journal of Petroleum Science and Engineering*, *48*, 94–104, doi:10.1016/j.petrol.2005.04.003.

Tiab, D., and E. C. Donaldson (2011), Petrophysics: theory and practice of measuring reservoir rock and fluid transport properties, *Gulf professional publishing*, USA.

Tie, H., and N. R. Morrow (2005), Oil recovery by spontaneous Imbibition before and after wettability alteration of three carbonate rocks by a moderately asphaltic crude oil, *Proceedings of Society of Core Analysts held in Toronto, Canada*, SCA2005-11.

Tohidi, B, J. Yang, M. Salehabadi, R. Anderson, and A. Chapoy (2010), CO_2 hydrates could provide secondary safety factor in subsurface sequestration of CO_2, *Environ. Sci. Technol.*, *44(4)*, 1509–1514, doi:10.1021/es902450j.

Treiber, L. E., and W. W. Owens (1972), A laboratory evaluation of the wettability of fifty oil-producing reservoirs, *Society of Petroleum Engineers Journal*, *12*, 531–540, doi:10.2118/3526-PA.

Valvatne, P. H., and M. J. Blunt (2004), Predictive pore-scale modeling of two-phase flow in mixed wet media, *Water Resour. Res.*, *40*, W07406, doi:10.1029/2003WR002627.

Vincent, J. V., and P. K. Kilpatrick (2007), Preferential solvent partitioning within asphaltenic aggregates dissolved in binary solvent mixtures, *Energy & fuels*, *21*, 1217-1225, doi:10.1021/ef060456n.

Washburn, E. W. (1921), The dynamics of capillary flow, *Phys. Rev.*, *17(3)*, 273-283, doi:10.1021/ef060456n.

Watson, J. (1911), British and foreign building stones: A descriptive catalogue of the specimens in the sedgwick museum, *Cambridge Univ. Press*, Cambridge, UK, doi:10.1017/S0016756800111410.

Weast, R. C., M. J. Astle, and W. H. Beyer (1988), CRC handbook of chemistry and physics, *CRC press Boca Raton, FL*, *69*.

Westphal, H., I. Surholt, C. Kiesl, H. F. Thern, and T. Kruspe (2005), NMR measurements in carbonate rocks: problems and an approach to a solution, *Pure Appl. Geophys.*, *162(3)*, 549-570, doi:10.1007/s00024-004-2621-3.

Wigley, T. M. L., R. Richels, and J. A. Edmonds (1996), Economic and environmental choices in the stabilization of atmospheric CO_2 concentrations, *Nature*, *379*, 240-243, doi:10.1038/379240a0.

Wong, P. Z., T. Lucatorto, and M. De Graef (1999), Methods of the Physics of Porous Media, *Academic Press*, *35*.

Wright, V. P., N. H. Platt, S. B. Marriott, and V. H. Beck (1995), A classification of rhizogenic (root-formed) calcretes, with examples from the Upper Jurassic-Lower Cretaceous of Spain and Upper Cretaceous of southern France, *Sedimentary Geology*, *100*, 143-158, doi:10.1016/0037-0738(95)00105-0.

Wu, Y., P. J. Shuler, M. Blanco, Y. Tang, and W. A. Goddard (2008), An experimental study of wetting behavior and surfactant EOR in carbonates with model compounds, *SPE Journal*, *13*, 26-34, doi:10.2118/99612-PA.

Zhang, X., N. R. Morrow, and S. Ma (1996), Experimental verification of a modified scaling group for spontaneous imbibition, *SPE Reservoir Engineering*, *11*, 280-285, doi:10.2118/30762-PA.

Zhao, X., M. J. Blunt, and J. Yao (2010), Pore-scale modeling: Effects of wettability on waterflood oil recovery, *Journal of Petroleum Science and Engineering*, *71*, 169–178, doi:10.1016/j.petrol.2010.01.011.

Zhou, D., L. Jia, J. Kamath, and A. R. Kovscek (2002), Scaling of counter-current imbibition processes in low-permeability porous media, *Journal of Petroleum Science and Engineering*, *33*, 61-74, doi:10.1016/S0920-4105(01)00176-0.

Zhou, X., N. R. Morrow, and S. Ma (2000), Interrelationship of wettability, initial water saturation, aging time, and oil recovery by spontaneous imbibition and waterflooding, *SPE Journal*, *5*, 199-207, doi:10.2118/62507-PA.

Appendices

A. Continuum-Scale Properties

A.1. Porosity

We use three different methods to measure the porosity of the cores.

A.1.1. Volume Balance

Before we start the experiment, we take the dimensions (length and width) and the dry weight of the core. Then, we place the core into a Hassler cell and we vacuum it for 12 hours. Separately, we vacuum the brine to make sure there is no air in the brine. After that, we inject 5 PV of degassed brine into the core. Then, we take the core out and we weigh it.

The difference between the dry core and the fully saturated core with brine, divided by the density will give us the pore volume and the pore volume divided by the volume of the core will give us the porosity as shown in the following equation:

$$\phi = \frac{PV}{\pi r^2 L} \tag{A.1}$$

where ϕ is the porosity of the rock, PV is the pore volume of the rock [cm^3], r is the radius of the core [cm], and L is the length of the core [cm].

A.1.2. Helium Porosimeter

We measure the helium porosity using a helium porosimeter device (Roberston Research Helium gas expansion volume meter, Model HGEVM/PG; Serial No. 823/M/0011). We use helium particularly as it has a very small molecular size which can go through the smallest pores in the rock and thus gives us accurate results.

The measurement of the helium porosity is based on Boyle's law for a constant temperature.

$$P_1 V_1 = P_2 V_2 \tag{A.2}$$

From the device, we have P_2 and V_2 as constant values and we measure P_1. Therefore, we can calculate V_2 which is the pore volume of the rock and by dividing by the rock volume, we can find the porosity.

A.1.3. Medical CT

From the medical CT we can obtain the porosity of the rock. In order to achieve that, we need to scan the core dry, with only air filling it. Then, we saturate the core with 100% brine and we take another scan. The comparison between the CT numbers of the dry scan and the saturated core scan, can give us the porosity. In addition, we need to take a scan of the brine separately to get its CT number. Air has a CT number of -1000 and the higher the density of the material, the higher the CT number will be.

The porosity can then be calculated from the following equation:

$$\phi_{CT} = \frac{CT_{wet} - CT_{dry}}{CT_{water} - CT_{air}} \tag{A.3}$$

where CT_{wet} is the CT number of the core when it is 100% saturated with brine, CT_{dry} is the CT number of the core when it is dry and filled only with air, CT_{water} is the CT number of water/brine and our brine has a CT number of 127.5, and CT_{air} is the CT number of air usually -1000.

A.1.4. Results

Tables A.1-A.3 show porosity measurements of each rock by using each method indicated earlier for Estaillades, Ketton, and Portland respectively. We can see that the results are comparable making each method valid.

Table A.1. Summary of porosity measurements on Estaillades limestone by using volume balance, helium porosimeter, and medical CT.

Core Label	ϕ [%]	Method
E1	28.0	Helium Porosimeter
E2	27.8	Helium Porosimeter
E3	27.5	Volume Balance
E4	27.5	Volume Balance
E5	28.2	Volume Balance
E6	28.0	Volume Balance
E*	27.6	Medical CT
E7	26.4	Helium Porosimeter
E8	27.3	Helium Porosimeter
E9	27.8	Helium Porosimeter
E10	28.0	Helium Porosimeter
E11	26.2	Helium Porosimeter
E12	27.2	Volume Balance
E13	27.3	Volume Balance
E14	28.0	Volume Balance
E15	27.9	Volume Balance
E16	26.2	Volume Balance
E17	26.2	Volume Balance
E18	27.6	Volume Balance
E19	28.4	Volume Balance

Table A.2. Summary of porosity measurements on Ketton limestone by using volume balance, helium porosimeter, and medical CT.

Core Label	ϕ [%]	Method
K1	23.4	Helium Porosimeter
K2	20.5	VHelium Porosimeter
K3	23.3	Volume Balance
K4	21.7	Volume Balance
K5	22.7	Volume Balance
K6	22.5	Volume Balance
K*	20.7	Medical CT
K7	20.2	Volume Balance
K8	22.0	Volume Balance
K9	22.0	Volume Balance
K10	21.9	Volume Balance
K11	22.0	Helium Porosimeter
K12	22.6	Helium Porosimeter
K13	21.8	Volume Balance
K14	22.0	Volume Balance

Table A.3. Summary of porosity measurements on Portland limestone by using volume balance, helium porosimeter, and medical CT.

Core Label	ϕ [%]	Method
P1	16.1	Helium Porosimeter
P2	19.6	Helium Porosimeter
P3	19.8	Volume Balance
P4	20.0	Volume Balance
P5	19.5	Volume Balance
P6	19.0	Volume Balance
P*	22.1	Medical CT
P7	22.8	Volume Balance
P8	19.7	Volume Balance
P9	19.8	Volume Balance
P10	18.0	Volume Balance
P11	18.9	Helium Porosimeter
P12	18.6	Helium Porosimeter
P13	17.0	Helium Porosimeter
P14	21.0	Volume Balance
P15	18.5	Volume Balance
P16	20.9	Volume Balance
P17	19.4	Volume Balance
P18	19.2	Volume Balance

A.2. Viscosity Measurement

We use the Rheotek U-tube viscometer for ambient viscosity measurements and we use a U-tube size O. This size is for fluids with viscosity range of 0-0.9 mPa s as they will take a certain amount of time to fill a specific volume. We fill the U-tube with the fluid we want to measure to reach to the point C shown in Figure A.1.

We use a pipette squeeze bulb o the top of the column of points A and B and lift the fluid until it reaches slightly above point A. We then get the timer ready and start recording then time when the fluid reaches to point A exactly and stop when it reaches to point B.

We use the following equation to calculate the kinematic viscosity:

$$v = zt \tag{A.4}$$

where v is the kinematic viscosity [mm^2/s], z is a constant depending on the tube dimensions: it is 0.0009524 [$(mm^2/s)/s$] for size O, and t is the time [s].

To obtain the dynamic viscosity, we divide the kinematic viscosity by the density of the fluid [*Weast et al.*, 1988].

Table A.4 shows the viscosity values used in the thesis.

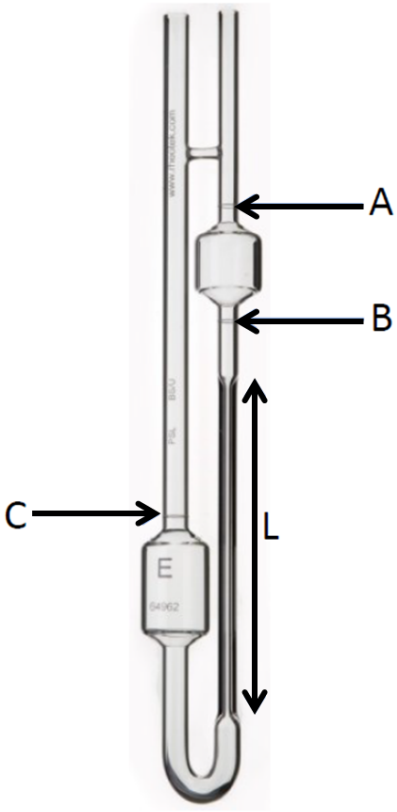

Figure A.1. U-tube capillary viscometer where A and B are timing marks, C is the filling mark, and L is the capillary length.

Table A.4. Viscosity measurement of n-decane and fluid A at ambient conditions.

Fluid	Viscosity[mPs]
n-decane	0.92
A	0.91

A:1.5 wt.% cyclohexanepntanoic acid in n-decane/brine

A.3. Absolute Permeability Measurements

A.3.1. Brine Absolute Permeability

First, we take the dimensions of the dry core. For this experiment, we use a Hassler cell, a Teledyne ISCO pump, a gas cylinder for confining pressure, and pressure transducers.

Then we insert the core into the Hassler cell, as shown in Figure A.2. We vacuum the core for 6-12 hours to remove any trapped air in the system. Separately, we vacuum the brine that we want to inject into the rock for overnight.

After vacuuming, we inject gaseous CO_2 to dispel any remaining trapped air. Then, we vacuum for one last round to remove the CO_2 from the system as the brine and CO_2 mixture will react with the carbonate mineral surface and cause changes in the rock morphology.

After that, we start injecting degassed brine at different flow rates. At every single flow rate, we keep injecting until we reach to the steady-state regime (no further fluctuations in the pressure).

We generally select five different flow rates and take down the pressure readings and from Darcy's equation; we can calculate the absolute brine permeability.

$$Q = \frac{kA\,(P_1 - P_2)}{\mu L} \tag{A.5}$$

where Q is flow rate [m^3/s], k is the absolute permeability [m^2], A is the cross-sectional area [m^2], P_1 is the upstream pressure [Pa], P_2 is the downstream pressure [Pa], μ is the viscosity [Pa.s], and L is the core length [m].

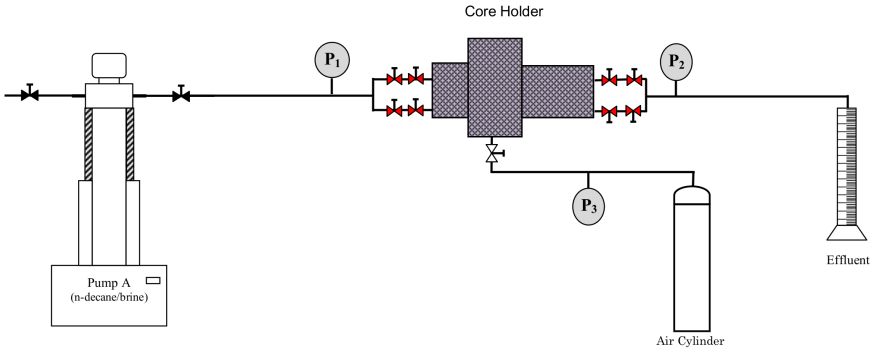

Figure A.2. Schematic of experimental apparatus to measure the brine absolute permeability.

A.3.2. Gas Absolute Permeability

Measuring the gas absolute permeability is a different technique than the brine absolute permeability, since the gas is compressible. For this experiment, we use a Hassler cell, two gas cylinders one for injection and one for confining, a metering valve, pressure transducers and a flow meter, as shown in Figure A.3.

We insert the core into the Hassler cell and for the gas permeability, vacuuming is not required. We set a constant pressure from the gas cylinder and we vary the flow rate through the metering valve. However, we need to maintain the flow rate to be below a Reynolds number of 2000 to ensure a laminar flow where Darcy's law is applicable and avoid turbulent flow [*Munson et al.*, 1990].

To calculate the Reynolds number, we use the following equation:

$$N_R = \frac{vD\rho}{\mu} \tag{A.6}$$

where N_R is the Reynolds number and it is dimensionless, v is the Darcy velocity [m/s], D is the diameter of the pipe [m], ρ is the density of the gas [kg/m^3], and μ is the viscosity of the gas [kg/m.s].

We recored the differential pressure across the core and the flow rate. We can calculate the gas absolute permeability from the following equation [*Bear*, 1988]:

$$Q = \frac{kA\left(P_1^2 - P_2^2\right)}{2\mu L} \tag{A.7}$$

where Q is flow rate [m^3/s], k is the absolute permeability [m^2], A is the cross-sectional area [m^2], P_1 is the upstream pressure [Pa], P_2 is the downstream pressure [Pa], μ is the viscosity [Pa.s], and L is the core length [m].

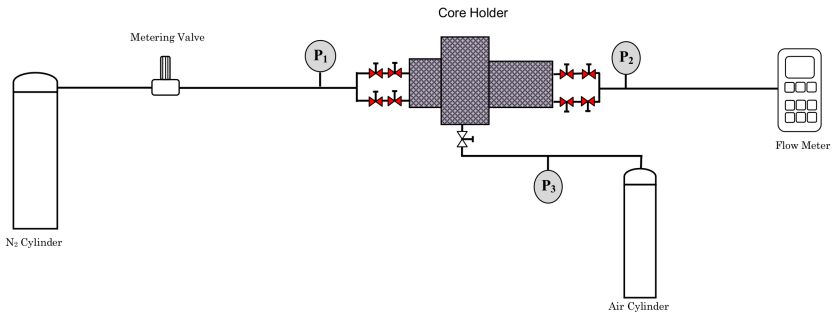

Figure A.3. Schematic of experimental apparatus to measure the gas absolute permeability.

We then correct the gas permeability for the Klinkenberg effect, as there is gas slip at the pore walls which is not observed for the liquids [*Klinkenberg*, 1941]. In order to correct the permeability, we have to plot the measured permeability from Equation A.7 versus $1/(P_{mean})$, where P_{mean} is $(P_1 + P_2)/2$. The y-intercept of this plot is the corrected permeability.

A.3.3. Results

Tables A.5-A.7 show a comparison between the measured permeability of brine and gas for for Estaillades, Ketton, and Portland respectively. We can see that the results are comparable.

Table A.5. Summary of the absolute permeability values performed by using gas and brine for Estaillades limestone.

Core Label	k [$\times 10^{-13}$ m^2]	Fluid used (Gas/Brine)
E1	1.34	Gas
E2	3.53	Gas
E3	1.19	Gas
E4	1.55	Gas
E5	3.94	Gas
E6	3.28	Gas
E*	2.10	Brine
E7	2.07	Gas
E8	1.69	Gas
E9	2.58	Gas
E10	2.96	Gas
E11	1.94	Gas
E12	1.77	Brine
E13	2.03	Brine
E14	2.18	Brine
E15	3.26	Brine
E16	1.22	Brine
E17	2.25	Brine
E18	1.69	Brine
E19	2.06	Brine

Table A.6. Summary of the absolute permeability values performed by using gas and brine for Ketton limestone.

Core Label	k [$\times 10^{-12}$ m^2]	Fluid used (Gas/Brine)
K1	1.62	Gas
K2	1.37	Gas
K3	1.88	Gas
K4	1.99	Gas
K5	2.23	Gas
K6	2.54	Gas
K*	2.35	Brine
K7	1.38	Brine
K8	1.07	Brine
K9	1.07	Brine
K10	1.28	Brine
K11	2.1	Brine
K12	3.55	Brine
K13	1.54	Brine
K14	2.6	Brine

Table A.7. Summary of the absolute permeability values performed by using gas and brine for Portland limestone.

Core Label	k [$\times 10^{-15}$ m^2]	Fluid used (Gas/Brine)
P1	10.1	Gas
P2	13.7	Gas
P3	15.2	Gas
P4	6.51	Gas
P5	18.2	Gas
P6	35.0	Gas
P*	5.23	Brine
P7	5.24	Brine
P8	3.2	Brine
P9	1.9	Brine
P10	1.8	Brine
P11	7.2	Gas
P12	4.17	Gas
P13	13.0	Gas
P14	6.2	Brine
P15	2.47	Brine
P16	9.9	Brine
P17	3.57	Brine
P18	5.77	Brine

A.4. Initial and Residual Saturations

We measure the initial and residual saturations (S_{oi} and S_{or}) via volumetric and mass balance techniques. The volumetric balance depends on knowing the pore volume, the volume produced, and the dead volume (if it exists). The mass balance technique depends on weighing the mass of the core at several stages and comparing them.

To measure the initial oil saturation using the volume balance, we use the following equation:

$$S_{oi} = \frac{V_{oi} - V_{DV}}{PV} \tag{A.8}$$

where S_{oi} is the initial oil saturation, V_{oi} is the volume of water displaced by oil during primary drainage [ml], V_{DV} is the dead volume of the cell [ml], and PV is the pore volume of the rock [ml].

To measure the initial oil saturation using the mass balance method, we use the following equation:

$$S_{oi} = \frac{M_{dry} - M_{drainage} + (\rho_{brine} PV)}{PV(\rho_{brine} - \rho_{oil})} \tag{A.9}$$

where S_{oi} is the initial oil saturation, M_{dry} is the mass of the dry core [kg], $M_{drainage}$ is the mass of core after drainage [kg], ρ_{brine} is the density of brine [kg/m^3], PV is the pore volume [m^3], and ρ_{oil} is the density of oil [kg/m^3].

To measure the residual oil saturation using the volume balance technique, we use the following equation:

$$S_{or} = \frac{V_{oi} - V_{DV} - V_{WF}}{PV} \tag{A.10}$$

where S_{or} is the residual oil saturation, V_{oi} is the volume of water displaced by oil during primary drainage [ml], V_{DV} is the dead volume of the cell [ml], V_{WF} is the volume of oil displaced by water during waterflooding [ml], and PV is the pore volume of the rock [ml].

To measure the residual oil saturation using the mass balance, we use the following equation:

$$S_{or} = \frac{M_{dry} - M_{WF} + (\rho_{brine} PV)}{PV(\rho_{brine} - \rho_{oil})} \tag{A.11}$$

where S_{or} is the residual oil saturation, M_{dry} is the mass of the dry core [kg], M_{WF} is the mass of core after waterflooding [kg], ρ_{brine} is the density of brine [kg/m^3], PV is the pore volume [m^3], and ρ_{oil} is the density of oil [kg/m^3].

A.4.1. Dead Volume Measurement

To measure the dead volume of the cell, we use a simple approach using a syringe. We take the inlet of the Hassler cell and we attach a syringe filled with water, we open the valve connected to the cell, Figure A.4. We start injecting water until we see water coming out of the cell, once we see the water coming out, we recored the amount of water displaced in the syring and that will be the dead volume. We repeat the same process three times to make sure the results are consistent.

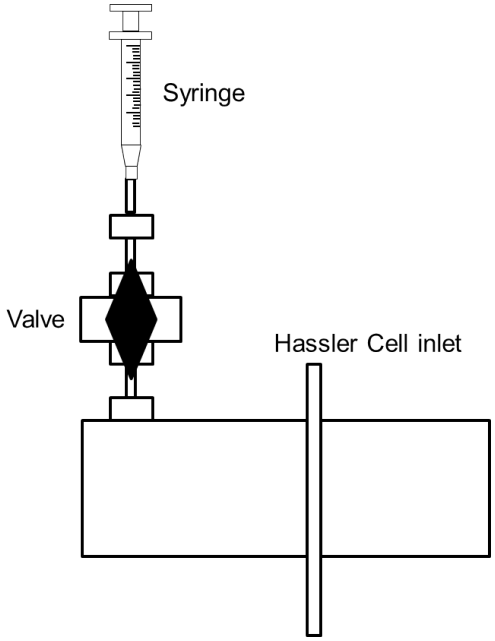

Figure A.4. Schematic of experimental process to measure the dead volume of the hassler cell.

Table A.8. Dead volume for the all the Hassler cells used in the thesis.

Cell#	1	2	3
Dead volume [ml]	1.85 ± 0.15	1.8 ± 0.1	0.85 ± 0.05

A.5. Interfacial Tension

We use a Ramé-Hart model 590 device to measure the interfacial tension of the fluids, figure A.5. The apparatus consists of a high resolution camera placed in front of fluids we want to measure. For gas/fluid systems, we can set the pipette to release a drop and the camera will capture the shape and then we calculate the interfacial tension.

For fluid/fluid system, we place a container filled with the intended fluid and we lower the pipette into the container and we release a drop of the higher dense fluid from the pipette and similarly we can measure the interfacial tension. Before each experiment, a calibration process is needed to make sure we capture the correct size of the droplet. Then, we measure the interfacial tension from the following equation:

$$\sigma = \frac{\Delta\rho g R_0^2}{\beta} \tag{A.12}$$

where σ is the interfacial tension [N/m], $\Delta\rho$ is the density difference between of the drop and the surrounding fluid [kg/m^3], g is the gravity constant [m/s^2], R is the radius of curvature at the drop apex [m], and β is the shape factor [*de Gennes et al.*, 2004, *Girifalco and Good*, 1957].

The results obtained is this thesis are shown in Figure A.6 and Table A.9.

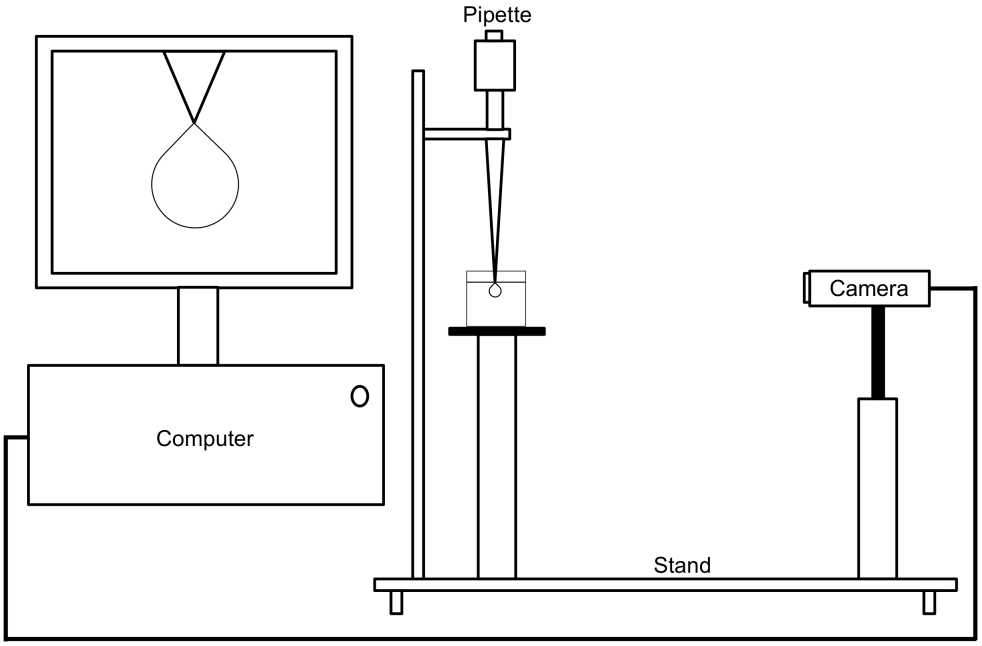

Figure A.5. Schematic of the experimental apparatus to measure the interfacial tension.

(a) (b) (c)

Figure A.6. Images showing the brine drop for interfacial tension measurement surrounded by (a) air, (b) n-decane, and (c) 1.5 wt.% cyclohexanepntanoic acid in n-decane.

Table A.9. The values of the interfacial tensions of the fluids used in the thesis.

Fluid Pair	air/brine	n-decane/brine	A/brine	crude oil/brine
IFT [mN/m]	73	52.3	19.8	27.2[a]

A:1.5 wt.% cyclohexanepntanoic acid in n-decane.
[a]Measured on the same same crude oil and with brine of 4.39 mol.kg^{-1} molality NaCl at 50°C and ambient pressure [*Li et al.*, 2015].

A.6. Contact Angle

We use a Ramé-Hart model 590 to measure the contact angle, Figure A.7. The apparatus consist of a high resolution camera attached to the computer. The camera is set to be in a linear position to the sample we want to measure. Before we measure the contact angle, we need to calibrate the camera to be in a central position using calibration tool. Once in position, we drop the fluid droplet on the intended surface, in our case we used calcite surface. To process the data, a built in software will identify the contact angle based on the interface of the droplet. If the interface is not detected by the software, then a manual identification of the interface is required.

The results of the contact angle measurements in this thesis are illustrated in Figure A.8 and Table A.10.

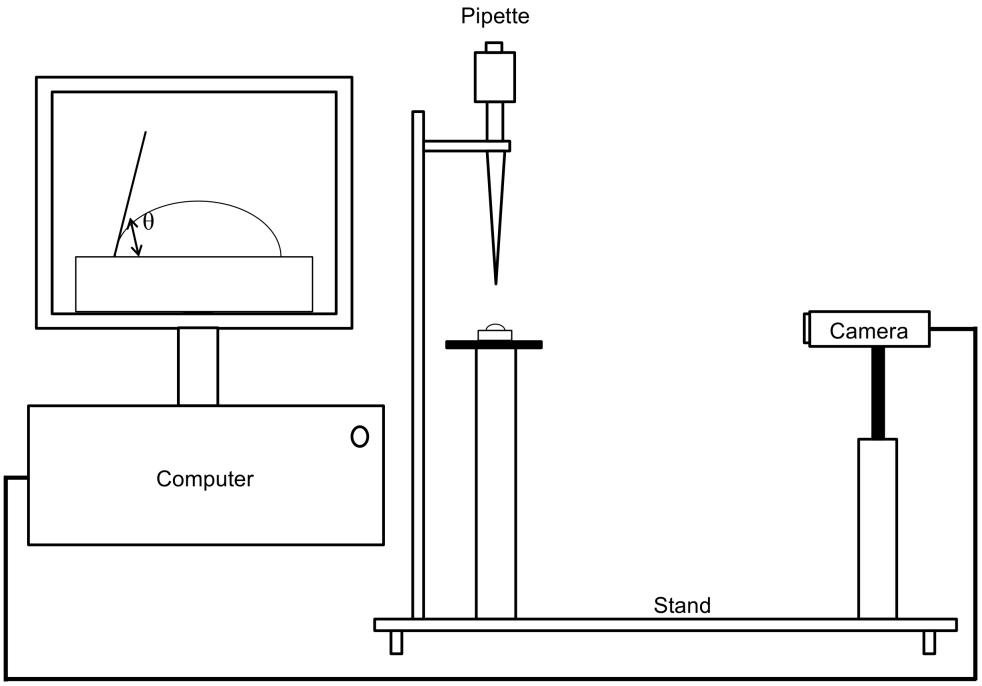

Figure A.7. Schematic of experimental apparatus to measure the contact angle.

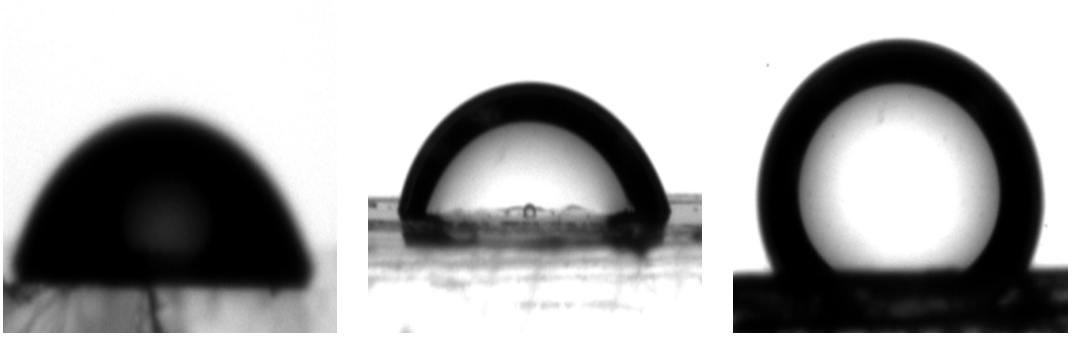

(a) (b) (c)

Figure A.8. Images showing brine droplets for contact angle measurements on a calcite surfaces surrounded by (a) air, (b) n-decane, and (c) 1.5 wt.% cyclohexanepntanoic acid in n-decane.

The contact angles of Figure A.8 are tabulated in Table A.10.

Table A.10. The values of the average contact angles (left and right) from Figure A.8.

Fluid Pair	air/brine	n-decane/brine	A/brine	crude oil/brine
θ_I [°]	37± 0.3	37.9 ± 0.2	130 ± 3	100[a]

A:1.5 wt.% cyclohexanepntanoic acid in n-decane.
[a]Measured on a smooth surface with the same same crude oil and with brine of 4.39 mol.kg^{-1} molality NaCl at 50°C and ambient pressure [*Li et al.*, 2015].

B. Analytical Solution

B.1. Formulation

To construct the analytical solution for the capillary dominated flow, we need to have both the imbibition relative permeability and capillary pressure.

We use Microsoft Excel in order to construct the solution. In this example, we assume water-wet rock properties, Table B.1. We use Corey exponents to capture the relative permeability:

$$k_{rw} = k_{rw,max}\left(\frac{S_w - S_{wi}}{1 - S_{wr} - S_{or}}\right)^n \tag{B.1}$$

where k_{rw} is the water relative permeability, $k_{rw,max}$ is the maximum water relative permeability, S_w is the water saturation, S_{wi} is the initial water saturation, S_{or} is the residual oil saturation, and n is the Corey water exponent.

$$k_{ro} = k_{ro,max}\left(\frac{1 - S_w - S_{wi}}{1 - S_{wr} - S_{or}}\right)^m \tag{B.2}$$

where k_{ro} is the oil relative permeability, $k_{ro,max}$ is the maximum oil relative permeability, S_w is the water saturation, S_{wi} is the initial water saturation, S_{or} is the residual oil saturation, and m is the Corey oil exponent.

We also use a power law to express the capillary pressure:

$$P_c = P_{c,entry}\left(\frac{S_w - S_{wi}}{1 - S_{wi} - S_{or}}\right)^\alpha \tag{B.3}$$

where P_c is the capillary pressure, $P_{c,entry}$ is the entry capillary pressure, S_w is the water saturation, S_{wi} is the initial water saturation, S_{or} is the residual oil saturation, and α is the capillary pressure exponent.

This example is different from chapter 3, because in chapter 3 we were trying to find the relative permeability and capillary pressure and fit it to our measurements, while in this example we have a fixed value for relative permeability and capillary pressure and we only try to find the C value that will satisfy the conditions that we will discuss below.

We use the following equations to construct the solution:

for co-current flow:

$$F(S_{wi}) = \Big(F(S_{wi-1}) - 0.5F(S_{wi-2}) + 0.5f(S_{wi})\Big) + \sqrt{0.25\Big(F(S_{w-2}) - 2F(S_{wi-1}) - f(y_i)\Big)^2 - \Big(f(S_{wi})(F(S_{wi-2}) - 2F(S_{wi-1})) + \Big(\frac{\phi}{2C^2}\Big)D(S_{wi})\Delta S_w^2\Big)} \tag{B.4}$$

while for counter-current flow:

$$F(S_{wi}) = \Big(F(S_{wi-1}) - 0.5F(S_{wi-2})\Big) + \sqrt{\Big(F(S_{wi-1}) - 0.5F(S_{wi-2})\Big)^2 - \Big(\frac{\phi}{2C^2}\Big)D(S_w)\Delta S_w^2} \tag{B.5}$$

where D is a non-linear capillary diffusion coefficient as a function of water saturation:

$$D(S_{wi}) = -\frac{k\lambda_w\lambda_o}{\lambda_t}\frac{\partial P_c}{\partial S_w} \tag{B.6}$$

where

$$\lambda_w = \frac{k_{rw}}{\mu_w} \tag{B.7}$$

$$\lambda_o = \frac{k_{ro}}{\mu_o} \tag{B.8}$$

$$\lambda_t = \lambda_w + \lambda_o \tag{B.9}$$

Tables B.2 and B.4 show the procedure in a spreadsheet showing how to construct the solution for co-current and counter-current spontaneous imbibition respectively. Tables B.3 and B.5 show the detailed input parameters and results of co-current and counter-current spreadsheets respectively. After we input all these parameters shown in Table B.1, we will only have to vary the value of C to satisfy the following conditions:

$$F(S_{wir}) = 0 \tag{B.10}$$

In addition, the integrated saturation curve must equal to the total volume imbibed:

$$\int_{S_{wir}}^{S_{w,max}} x(S_w, t)dS_w = \frac{Q_w(t)}{\phi} = \frac{2C\sqrt{t}}{\phi} \tag{B.11}$$

where we can re-arrange and approximate the integral to give:

$$\Sigma_{i=1}^{n} F'(S_w, i)\Delta S_w \approx \frac{Q_w(t)}{\phi} = \frac{\phi}{2C} = 1 \tag{B.12}$$

We start the process by guessing an initial value of C and we keep iterating until we satisfy Equation B.10. The outcome of the analytical solution is in the form of ω_D which is the dimensionless form of ω. ω can be achieved by multiplying ω_D by the constant C.

Table B.1. Input parameters used for the construction of the analytical solution example of spontaneous imbibition.

Input Parameter	Value
S_{wi}	0
S_{or}	0.4
n	3
$k_{rw,max}$	0.2
m	1.5
$k_{ro,max}$	0.85
$Pc, entry$ [Pa]	12000
α	-0.7
Maximum P_c [Pa]	400000
μ_w [Pa. s]	0.001
μ_o [Pa. s]	0.003
k [$\times$ 10^{-13} m^2]	2.96
ϕ	0.20

B.1.1. Construction of Spontaneous Imbibition Analytical Solution

Table B.2. Procedure to construct the co-current analytical solution in a spreadsheet.

i	S_w	k_{rw}	k_{ro}	P_c	D	f_w	F	C	ω_D	$\Sigma_{i=1}^{n} F'(S_w, i)\Delta S_w$
1	S_{w1}	k_{rw1}	k_{ro1}	P_{c1}	0	$(k_{rw1}/\mu_w)/(k_{rw1}/\mu_w + k_{ro1}/\mu_o)$	1	We start with	0	0
2	S_{w2}	k_{rw2}	k_{ro2}	P_{c2}	Equation 4.18	$(k_{rw2}/\mu_w)/(k_{rw2}/\mu_w + k_{ro2}/\mu_o)$	1	initial guess	dF/dS_w	Equation 4.24
3	S_{w3}	k_{rw3}	k_{ro3}	P_{c3}	Equation 4.18	$(k_{rw3}/\mu_w)/(k_{rw3}/\mu_w + k_{ro3}/\mu_o)$	Equation 4.16	and iterate	dF/dS_w	Equation 4.24
4	S_{w4}	k_{rw4}	k_{ro4}	P_{c4}	Equation 4.18	$(k_{rw4}/\mu_w)/(k_{rw4}/\mu_w + k_{ro4}/\mu_o)$	Equation 4.16	to satisfy	dF/dS_w	Equation 4.24
5	S_{w5}	k_{rw5}	k_{ro5}	P_{c5}	Equation 4.18	$(k_{rw5}/\mu_w)/(k_{rw5}/\mu_w + k_{ro5}/\mu_o)$	Equation 4.16	the conditions	dF/dS_w	Equation 4.24
3	S_{w6}	k_{rw6}	k_{ro6}	P_{c6}	Equation 4.18	$(k_{rw6}/\mu_w)/(k_{rw6}/\mu_w + k_{ro6}/\mu_o)$	Equation 4.16	discussed earlier	dF/dS_w	Equation 4.24
7	S_{w7}	k_{rw7}	k_{ro7}	P_{c7}	Equation 4.18	$(k_{rw7}/\mu_w)/(k_{rw7}/\mu_w + k_{ro7}/\mu_o)$	Equation 4.16		dF/dS_w	Equation 4.24
8	S_{w8}	k_{rw8}	k_{ro8}	P_{c8}	Equation 4.18	$(k_{rw8}/\mu_w)/(k_{rw8}/\mu_w + k_{ro8}/\mu_o)$	Equation 4.16		dF/dS_w	Equation 4.24
9	S_{w9}	k_{rw9}	k_{ro9}	P_{c9}	Equation 4.18	$(k_{rw9}/\mu_w)/(k_{rw9}/\mu_w + k_{ro9}/\mu_o)$	Equation 4.16		dF/dS_w	Equation 4.24
10	S_{w10}	k_{rw10}	k_{ro10}	P_{c10}	Equation 4.18	$(k_{rw10}/\mu_w)/(k_{rw10}/\mu_w + k_{ro10}/\mu_o)$	Equation 4.16		dF/dS_w	Equation 4.24
11	S_{w11}	k_{rw11}	k_{ro11}	P_{c11}	Equation 4.18	$(k_{rw11}/\mu_w)/(k_{rw11}/\mu_w + k_{ro11}/\mu_o)$	Equation 4.16		dF/dS_w	Equation 4.24
12	S_{w12}	k_{rw12}	k_{ro12}	P_{c12}	Equation 4.18	$(k_{rw12}/\mu_w)/(k_{rw12}/\mu_w + k_{ro12}/\mu_o)$	Equation 4.16		dF/dS_w	Equation 4.24
13	S_{w13}	k_{rw13}	k_{ro13}	P_{c13}	Equation 4.18	$(k_{rw13}/\mu_w)/(k_{rw13}/\mu_w + k_{ro13}/\mu_o)$	Equation 4.16		dF/dS_w	Equation 4.24
14	S_{w14}	k_{rw14}	k_{ro14}	P_{c14}	Equation 4.18	$(k_{rw14}/\mu_w)/(k_{rw14}/\mu_w + k_{ro14}/\mu_o)$	Equation 4.16		dF/dS_w	Equation 4.24
15	S_{w15}	k_{rw15}	k_{ro15}	P_{c15}	Equation 4.18	$(k_{rw15}/\mu_w)/(k_{rw15}/\mu_w + k_{ro15}/\mu_o)$	Equation 4.16		dF/dS_w	Equation 4.24
.	.	.	.	.	.	.	.	.	.	.
.	.	.	.	.	.	.	.	.	.	.
.	.	.	.	.	.	.	.	.	.	.
.	.	.	.	.	.	.	.	.	.	.
n	S_{wn}	k_{rwn}	k_{ron}	P_{cn}	Equation 4.18	$(k_{rwn}/\mu_w)/(k_{rwn}/\mu_w + k_{ron}/\mu_o)$	0		dF/dS_w	1

Table B.3. Actual data used to construct the co-current analytical solution in a spreadsheet.

i	S_w	k_{rw}	k_{ro}	P_c	D	f_w	F	C	ω_D	$\Sigma_{i=1}^{n} F'(S_w, i)\Delta S_w$
1	0.6	0.2	0	12000	0	1	1	1.1016×10^{-4}	0	0
2	0.596	0.196	0.0004	12056	6.3×10^{-10}	0.999	1		0	0
3	0.592	0.192	0.0012	12113	1.8×10^{-9}	0.997	0.9998		0.0279	0.0001
4	0.588	0.188	0.0023	12170	3.3×10^{-9}	0.995	0.9996		0.056	0.0003
5	0.58	0.184	0.0036	12228	5.2×10^{-9}	0.993	0.9993		0.085	0.0006
6	0.576	0.18	0.0051	12286	7.5×10^{-9}	0.99	0.9988		0.114	0.0011
7	0.572	0.177	0.0067	12345	9.7×10^{-9}	0.987	0.9982		0.144	0.0017
8	0.568	0.173	0.0084	12405	1.2×10^{-8}	0.983	0.9976		0.174	0.0023
9	0.560	0.169	0.01	12466	1.5×10^{-8}	0.98	0.9967		0.204	0.0032
10	0.556	0.166	0.012	12527	2.1×10^{-8}	0.975	0.9958		0.234	0.0041
11	0.552	0.162	0.014	12590	2.5×10^{-8}	0.971	0.9948		0.264	0.0051
12	0.548	0.159	0.016	12652	2.8×10^{-8}	0.966	0.9936		0.294	0.0063
13	0.554	0.156	0.019	12716	3.2×10^{-8}	0.96	0.9923		0.324	0.0076
14	0.536	0.152	0.021	12781	3.6×10^{-8}	0.953	0.99		0.354	0.009
15	0.532	0.149	0.023	12846	4.1×10^{-8}	0.94	0.989		0.384	0.01
.	.	.	.	.	.	.	.	.	.	.
.	.	.	.	.	.	.	.	.	.	.
.	.	.	.	.	.	.	.	.	.	.
.	.	.	.	.	.	.	.	.	.	.
151	0	0	0.85	400000	0	0	0		1.75	1

Table B.4. Procedure to construct the counter-current analytical solution in a spreadsheet.

i	S_w	k_{rw}	k_{ro}	P_c	D	F	C	ω_D	$\Sigma_{i=1}^{n} F'(S_w, i)\Delta S_w$
1	S_{w1}	k_{rw1}	k_{ro1}	P_{c1}	0	1	We start with	0	0
2	S_{w2}	k_{rw2}	k_{ro2}	P_{c2}	Equation 4.18	1	initial guess	dF/dS_w	Equation 4.24
3	S_{w3}	k_{rw3}	k_{ro3}	P_{c3}	Equation 4.18	Equation 4.17	and iterate	dF/dS_w	Equation 4.24
4	S_{w4}	k_{rw4}	k_{ro4}	P_{c4}	Equation 4.18	Equation 4.17	to satisfy	dF/dS_w	Equation 4.24
5	S_{w5}	k_{rw5}	k_{ro5}	P_{c5}	Equation 4.18	Equation 4.17	the conditions	dF/dS_w	Equation 4.24
6	S_{w6}	k_{rw6}	k_{ro6}	P_{c6}	Equation 4.18	Equation 4.17		dF/dS_w	Equation 4.24
7	S_{w7}	k_{rw7}	k_{ro7}	P_{c7}	Equation 4.18	Equation 4.17		dF/dS_w	Equation 4.24
8	S_{w8}	k_{rw8}	k_{ro8}	P_{c8}	Equation 4.18	Equation 4.17		dF/dS_w	Equation 4.24
9	S_{w9}	k_{rw9}	k_{ro9}	P_{c9}	Equation 4.18	Equation 4.17		dF/dS_w	Equation 4.24
10	S_{w10}	k_{rw10}	k_{ro10}	P_{c10}	Equation 4.18	Equation 4.17		dF/dS_w	Equation 4.24
11	S_{w11}	k_{rw11}	k_{ro11}	P_{c11}	Equation 4.18	Equation 4.17		dF/dS_w	Equation 4.24
12	S_{w12}	k_{rw12}	k_{ro12}	P_{c12}	Equation 4.18	Equation 4.17		dF/dS_w	Equation 4.24
13	S_{w13}	k_{rw13}	k_{ro13}	P_{c13}	Equation 4.18	Equation 4.17		dF/dS_w	Equation 4.24
14	S_{w14}	k_{rw14}	k_{ro14}	P_{c14}	Equation 4.18	Equation 4.17		dF/dS_w	Equation 4.24
15	S_{w15}	k_{rw15}	k_{ro15}	P_{c15}	Equation 4.18	Equation 4.17		dF/dS_w	Equation 4.24
.	.	.	.	.	.	.	.	.	.
.	.	.	.	.	.	.	.	.	.
.	.	.	.	.	.	.	.	.	.
.	.	.	.	.	.	.	.	.	.
n	S_{wn}	k_{rwn}	k_{ron}	P_{cn}	Equation 4.18	0		dF/dS_w	1

Table B.5. Actual data used to construct the counter-current analytical solution in a spreadsheet.

i	S_w	k_{rw}	k_{ro}	P_c	D	F	C	ω_D	$\Sigma_{i=1}^{n} F'(S_w, i)\Delta S_w$
1	0.6	0.2	0	12000	0	1	5.656×10^{-5}	0	0
2	0.596	0.196	0.0004	12056	6.3×10^{-10}	1		0	0
3	0.592	0.192	0.0012	12113	1.8×10^{-9}	0.99999		0.00022	8.97×10^{-7}
4	0.588	0.188	0.0023	12170	3.3×10^{-9}	0.99999		0.00064	3.46×10^{-6}
5	0.58	0.184	0.0036	12228	5.2×10^{-9}	0.99999		0.00129	8.6×10^{-6}
6	0.576	0.18	0.0051	12286	7.5×10^{-9}	0.99998		0.00221	1.74×10^{-5}
7	0.572	0.177	0.0067	12345	9.7×10^{-9}	0.99996		0.00342	3.1×10^{-5}
8	0.568	0.173	0.0084	12405	1.2×10^{-8}	0.99994		0.00668	5.08×10^{-5}
9	0.560	0.169	0.01	12466	1.5×10^{-8}	0.99992		0.0091	7.08×10^{-5}
10	0.556	0.166	0.012	12527	2.1×10^{-8}	0.99985		0.01185	0.000114
11	0.552	0.162	0.014	12590	2.5×10^{-8}	0.99983		0.01498	0.000162
12	0.548	0.159	0.016	12652	2.8×10^{-8}	0.99977		0.01858	0.000221
13	0.554	0.156	0.019	12716	3.2×10^{-8}	0.9997		0.02266	0.000295
14	0.536	0.152	0.021	12781	3.6×10^{-8}	0.99961		0.02724	0.000385
15	0.532	0.149	0.023	12846	4.1×10^{-8}	0.99937		0.03236	0.000493
.	.	.	.	.	.	.	.	.	.
.	.	.	.	.	.	.	.	.	.
.	.	.	.	.	.	.	.	.	.
.	.	.	.	.	.	.	.	.	.
151	0	0	0.85	400000	0	0		3.9559	1

B.1.2. Results

In this part, we will show the results after applying the data in the tables above. Figure B.1 shows the imbibition capillary pressure used in this study which is plotted using the power law from the data in Table B.1. Figure B.2 shows the imbibition relative permeability used in this study which is plotted using Corey exponents. Figure B.3 shows the fractional flow curves for co-current and counter-current spontaneous imbibition from this study in addition to the Buckley-Leverett fractional flow. Figure B.4 shows ω as a function of water saturation.

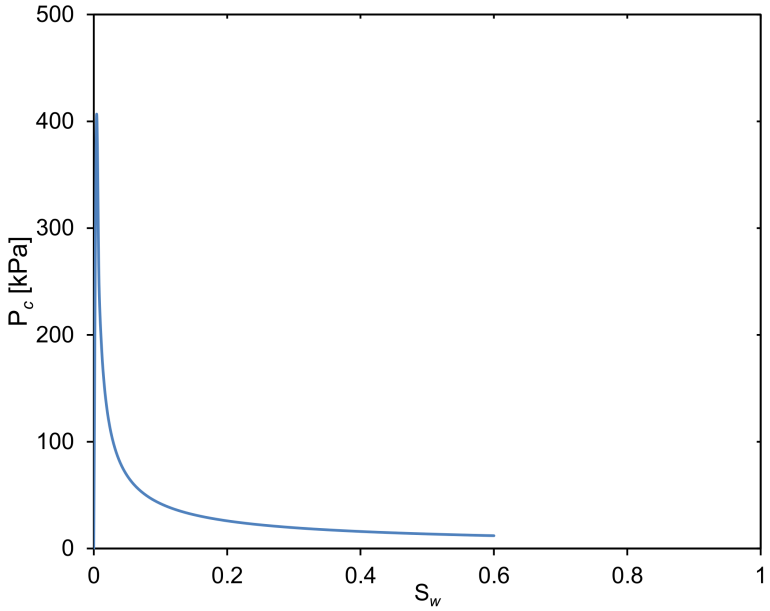

Figure B.1. Imbibition capillary pressure as a function of water saturation used in this example.

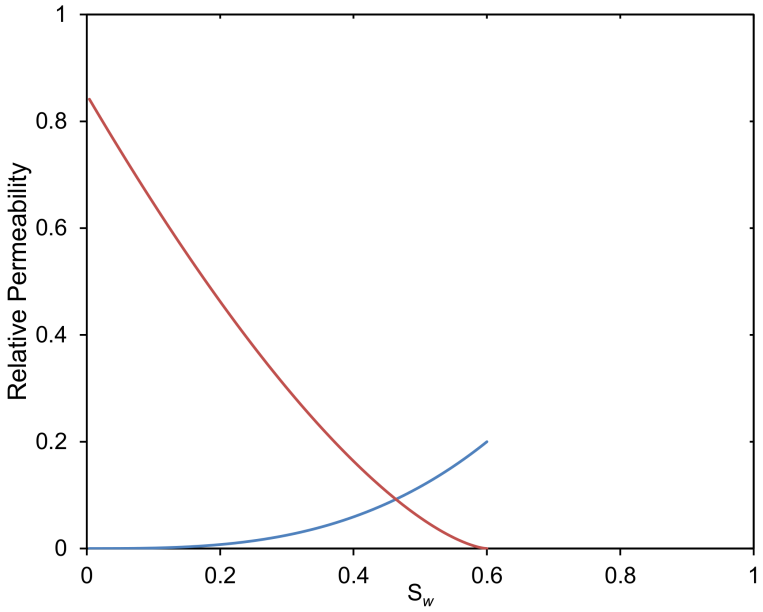

Figure B.2. Imbibition relative permeability as a function of water saturation used in this study.

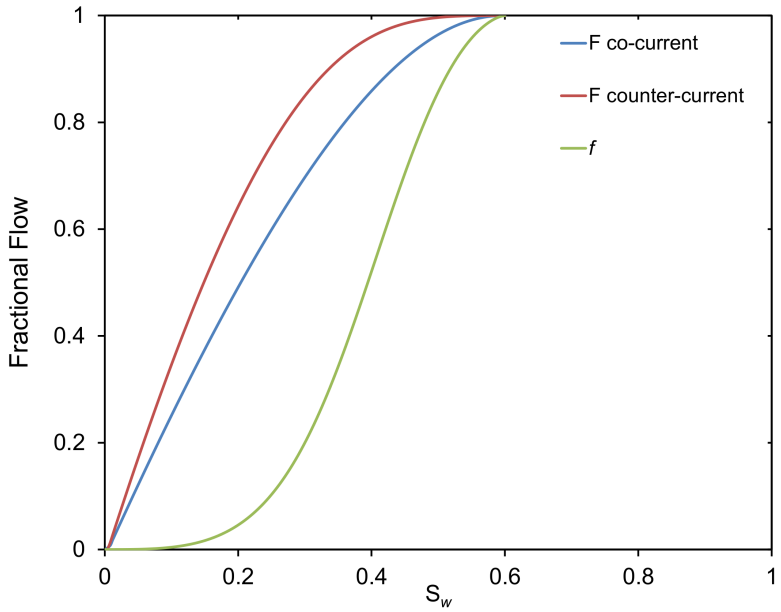

Figure B.3. Three fractional flow curves based on this analysis: Buckley-Leverett, co-current, and counter-current.

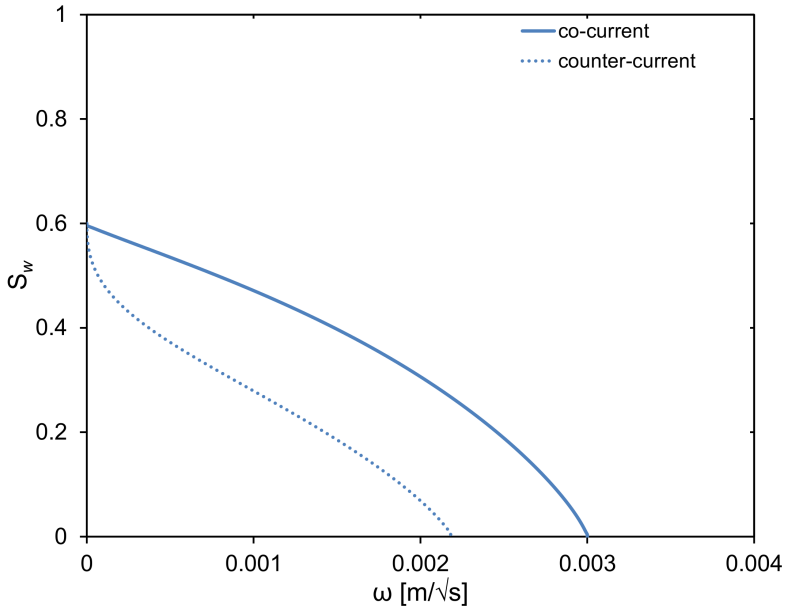

Figure B.4. The results of the co-current and counter-current spontaneous imbibition in the form of ω as a function of water saturation.